EFFECT OF CATALYTIC FILMS ON CERAMIC CONVERSION TREATMENT OF TITANIUM ALLOYS FOR MEDICAL DEVICES

by

JAMES EDWARD ALEXANDER

A thesis submitted to the University of Birmingham for the degree of

DOCTOR OF PHILOSOPHY

School *of* Metallurgy and Materials

College *of* Engineering and Physical Sciences

University *of* Birmingham

July 2022

Abstract

Titanium (Ti) and its alloys are attractive metals for biomedical use, where predominantly Ti-6Al-4V (Ti64) is used. This is largely due to their desirable mechanical and chemical properties, which include low density, excellent fatigue resistance, and high corrosion resistance. Additionally, Ti is renowned for its excellent biocompatibility and for being one of the only known metals to promote osseointegration, which is the growth of bone onto the surface of the metal. However, untreated Ti suffers from very poor wear resistance that results in the release of wear particles and ions into the surrounding tissue and systemic circulation. This is worsened with alloys like Ti64 due to the presence of vanadium, which is known to be highly toxic, so alternative alloys are being investigated, one of which is Ti-6Al-7Nb (Ti67), which has also been investigated within this study.

Ceramic conversion treatment (CCT, C2T) is an effective approach used to resolve the poor tribological properties. This thermal oxidation process results in the formation of a hard, wear resistant surface rutile (TiO_2) oxide layer, with an underlying oxygen-hardened diffusion zone (ODZ). Additionally, CCT further improves the corrosion resistance of Ti, which is beneficial in biological applications due to the aggressive *in vivo* environment. However, it takes approximately 80-100 hours to produce a high-quality oxide layer of 2-5 μm on Ti64. The research within this thesis is focussed on enhancing the CCT process through surface pre-deposition of catalytic films consisting of Au, Ag, Pd, or a combination of Ag and Pd to produce novel catalytic ceramic conversion treatment (CCCT, C3T).

Detailed characterisation of the influence of these coatings on the CCT process demonstrate a significant increase in oxide layer thickness from ≈ 5 to ≈ 100 μm with the same

treatment conditions, and a reduction in treatment time from 80 to 1 h to generate an equal layer thickness. C3T presented an improved oxide layer-substrate inter-facial bonding, aluminium-rich layers at the subsurface, and surface agglomeration. In-depth analysis of C3T Ag/Pd by TEM and EDX revealed a surface layer consisting of 2 sublayers: (1) a superficial layer containing agglomerates of palladium (and trace silver) oxide, and amorphous-like alumina fine grains within the grain boundaries. (2) an underlying structure dominated by nano-columnar grains of TiO_2/Al_2O_3, with trace silver and palladium particles.

Owing to the alumina produced at the subsurface and the underlying supporting nano grains, the C3T layers were of higher surface hardness and load bearing capacity, and therefore demonstrated a significant improvement in durability during reciprocating tribological testing.

A potential application for the novel C3T was assessed by fixation pin drilling into a simulated bone material with untreated and treated pins. It revealed the resilience of the oxide layers even when produced on complex geometry objects, where the treatments both reduced insertion force and the generated temperatures during drilling.

In addition to this, a significant reduction in the number of colony-forming units per ml of *Staphylococcus aureus* on the C3T surfaces was observed, which was maintained post fixation pin drilling, proving its potential for the medical field.

Ackowledgements

I would like to firstly thank my project supervisors, Professor Hanshan Dong, Dr Xiaoying Li, and Dr Rachel Sammons for their guidance and support throughout this study. Without which, this project would not have been possible.

I gratefully thank everyone involved within the Centre for Doctoral Training in Innovative Metal Processing (IMPaCT) funded by the UK Engineering and Physical Sciences Research Council (EPSRC), grant reference EP/L016206/1.

I am thankful for the support given by my colleagues within the Surface Engineering Group, including Dr Zhenxue Zhang, Dr Zhiyuan Jing, Dr Yana Liang, and Dr Tatiana Mukinay. Special thanks also go to Dr Behnam Dashtbozorg and Dr Valter Luiz Jantara Jr for not only their support with my studies, but also for their friendship.

I would like to thank Dr Xiao Tao for his help with SEM and TEM during the Covid-19 pandemic. I would also like to thank all the staff within the School of Metallurgy and Materials and School of Dentistry, especially Jaswinder Singh, Paul Stanley, Amy Newell, Gay Smith, and Dr Sarah Kuehne. Thanks also to Dr Ali Abdelhafeez Hassan from the School of Mechanical Engineering for his help with the fixation pin drilling.

Finally, I would like to give thanks, love, and appreciation to my friends and family for their confidence and support throughout the years I have been at the university, both during my undergraduate and PhD.

Publications

Zhang, Z., Zhang, Y., Li, X., **Alexander, J.**, Dong, H. 2020. An enhanced ceramic conversion treatment of Ti6Al4V alloy surface by a predeposited thin gold layer. *Journal of Alloys and Compounds*, 844:155867

Alexander J, Dong H, Bose D, Hassan AA, Soo SL, Zhang Z, Tao X, Kuehne S, Li X, Dong H. 2021. Novel Catalytic Ceramic Conversion Treatment of Ti6Al4V for Improved Tribological and Antibacterial Properties for Biomedical Applications. *Materials*, 14(21):6554

Contents

List of Figures

List of Tables

List of Abbreviations

Ag - Silver

Ag/Pd - Silver and palladium Al_2O_3 - Aluminium oxide/alumina

Au – Gold

BCC – Body centred cubic

C2T - Ceramic conversion treatment

C3T - Catalytic ceramic conversion treatment

CCCT - Catalytic ceramic conversion treatment

CCT – Ceramic conversion treatment

CFU - Colony forming units

CoCr - Cobalt chromium CoCr – Cobalt chromium

Cp – Commercially pure

E. coli - *Escherichia coli*

EDX - Energy-dispersive X-ray spectroscopy

GDOES – Glow discharge optical emission spectroscopy

HAADF – High-angle annular dark field

HCP – Hexagonal close packed

MOA - Micro-arc oxidation

ODZ – Oxygen diffusion zone

Pd - Palladium

PVD – Physical vapour deposition

ROS - Reactive oxygen species

S. aureus - *Staphylococcus aureus*

SAD - Selected area diffraction

SEM – Scanning electron microscopy

SMAT – Surface mechanical attrition treatment

SS - Stainless steel

TEM – Transmission electron microscopy

Ti – Titanium

Ti64 – Ti-6Al-4V

Ti67 – Ti-6Al-7Nb

TiN – Titanium nitride

TiO_2 – Titanium dioxide/titania

TO – Thermal oxidation

Unt – Untreated

XRD – X-ray diffraction

Chapter 1

Introduction

Many materials are used within the biomedical field with a vast array of applications, ranging from both soft and hard implants for vascular grafts and orthopaedic implants respectively, to supportive devices such as pacemakers and heart valves, to wound care and surgical dressings, to surgical instruments and diagnostic equipment. There has been a huge global effort to the development of these biomaterials to improve their mechanical and physical properties. The materials can be subdivided into metallic, polymeric, ceramic, and composite systems [1–3].

Metallic materials are readily used within the biomedical field, whereby titanium and its alloys are a major player, with Ti-6Al-4V being the currently most adopted alloy. This is due to their desirable properties of a high strength-weight ratio, corrosion resistance, and excellent biocompatibility [4–6].

Titanium forms a passive oxide film which aids in biocompatibility due to it protecting the material from the harsh conditions within the body [1,7]. However, this natural oxide is very thin (≈ 3 nm) and easily damaged/removed when it is in contact with a counterpart surface in motion, and titanium suffers greatly from this poor tribological performance [4].

In addition to this, the performance of a material used within the body can also be compromised by implant-associated hospital and community acquired infections [8, 9] which will lead to further complications including potential loosening, and therefore failure, of the implant device [9–11].

A method to overcome these drawbacks is to modify the surface of the material, termed surface engineering, to improve the poor properties at this surface whilst maintaining the advantageous properties of the bulk material [12, 13].

A currently adopted surface treatment method for titanium is ceramic conversion treatment (CCT) [14]. This is a thermal oxidation process in which the titanium reacts with oxygen to *in situ* convert to titanium oxides. This successfully produces hard oxide layers with low friction and high resistance to wear and corrosion [15]. However, this process requires treatment times of 80+ hours to yield useful layer thicknesses (2-5 μm) for improved performance which is time- and energy- consuming [14, 16].

Noble metals for oxidation catalysis have been of interest in recent years [17–19], which coupled with their antimicrobial potential [20–23], offer an exciting opportunity for a multifunctional treatment of titanium alloys for medical devices.

1.1 Aims and Objectives of this work

The aim of this investigation was to study the effect of catalytic films on CCT of Ti64 and Ti67 alloys to increase the surface layer thickness/reduce the required treatment duration, and to yield durable antimicrobial surfaces. In order to address this aim, the investigation can be broken down into the following objectives:

1. To develop and optimise a novel CCT process utilising catalysts for Ti64 and Ti67 titanium alloys.
2. To study the effect of this process on the micro-structures using SEM, chemical

composition using EDX and GDOES, and the effect on the phase constituents and crystal structures using XRD and TEM.

3. To evaluate the effect of these treatments on the mechanical properties using hardness testing, and durability using reciprocating sliding wear.

4. To further scientific understanding of the roles of catalysts roles on the CCT process and the mechanisms involved.

5. To investigate the effect of this novel CCT (of selected optimal treatments from the previous objectives) on the biological performance using anti-bacterial testing of *S. aureus*, and a potential future medical application of the treatments using fixation pin drilling.

1.2 Outline of Thesis

Chapter 2 provides a review of the current findings and evolution of research within the related fields of metallurgy, biomaterials, microbiology, surface engineering, tribology, and catalysis.

Chapter 3 describes the experimental materials and methodology used. Detail on how the samples were prepared, catalytic films were applied, and how these were characterised via scanning electron microscopy (SEM), energy dispersive X-ray analysis (EDX), glow-discharge optical emission spectroscopy (GDOES), transmission electron microscopy (TEM), etc. Additionally, how the samples were mechanically and tribologically assessed is described. It also contains how the samples were tested for their antimicrobial ability, and how fixation pin drilling procedure was carried out.

Chapter 4 reports the experimental results of the influence of the catalytic films on surface morphology, cross-sectional layer structures, micro-structure and compositional analysis of the layers. Surface mechanical and tribological performance assessments are also shown. As well as these, results of how the surfaces perform as antimicrobial surfaces against *Staphylococcus aureus* (*S. aureus*) are reported. In addition to this, the performance of the surface treatments to increase fixation pin durability for drilling into simulated bone, and the influence this has on the generated temperature, force, and whether it alters the antimicrobial performance are assessed.

Chapter 5 is divided into 4 main sections and discusses the main findings. It discusses how the different alloys differed in response to CCT; the influence of the catalytic films on the CCT of titanium alloys Ti-6Al-4V and Ti-6Al-7Nb and the potential mechanism in which these catalysts function; the durability and antimicrobial performance of the surface treated layers.

Chapter 6 summarises the main findings based on the obtained results and discussions. Potential future work is also discussed.

Chapter 2

Literature Review

2.1 Biomaterial

A biomaterial is defined as “a nonviable material used in a medical device, intended to interact with biological systems”; whereby as a prerequisite they should be biocompatible, which is “to perform with an appropriate host response in a specific application” [1,2,24].

As all implantation, regardless of method, results in a disruption in the local environment, the successfulness of a biomaterial depends on how much this disruption effects host homoeostasis [25]. This is because seconds after a material is implanted within the body, it contacts blood and bodily fluids. In order to protect itself, the body will adsorb non-specific plasma proteins and immune and inflammatory cells to the material, which is one of the first stages in the inflammatory/wound healing process. The type and quantity of these plasma proteins and cells will depend upon the surface of the material, so therefore the surface of a material dictates the response that the host will have to it [26, 27]. The body has two main responses to foreign object implantation:

The first response involves an immune response, known as the foreign body response, which then leads to inflammation and fibrous encapsulation of the implant. This fibrous encapsulation leads to poor biomechanical fixation, therefore resulting in clinical failure and the need to remove the implant. Titanium is non-allogenic thus reducing the risk of this post-operative trauma, which is often seen with other materials. This therefore reduces the initiation of bone/tissue necrosis when using titanium [1,3,28].

The second response involves direct contact between the native bone and the implant, without the presence of a connective tissue layer between them, termed osseointegration. Titanium is one of the few metals in which this is able to occur [1,28]. The rate of this osseointegration, and therefore bone-implant fixation, is dependent on both the surface morphology, where rougher surfaces result in earlier fixation, and composition [28].

The reason titanium is able to do this is due to the fact that in oxygen containing environments, titanium spontaneously forms a nm thick titanium dioxide (TiO_2) oxide layer [29,30], which both is bio-inert and has an isolating effect. This isolating effect also means that unlike with many metallic biomaterials, it does not have a tendency to lose electrons once in solution, therefore reducing the amount of corrosion/release of corrosion products. This results in a reduction in inflammation and osteolysis [31,32].

This isolating effect is due to the fact that non-/semi- conductive oxides undergo Coulomb electron repulsion and thus have localised d-electrons compared with most transition metals, which have partially filled d-bands and therefore de-localised electrons. This isolating effect prevents a large amount of ionic flow, therefore preventing the dissolution of ions into the host and direct cell attachment without fibrous encapsulation occurring [4,28].

Additionally, the fact that titanium has a high superficial energy means that it stimulates the body to synthesise and deposit minerals at the bone-implant interface [33], meaning that it is an ideal candidate for orthopaedic implants. This is also influenced by the surface morphology, for example roughness.

This is because when a surface is very smooth it has a reduced contact area, which will therefore result in a reduced adhesion to the surrounding tissue. However, with a rougher surface there will be increased adhesive strength due to cell ingrowth, for example bone ingrowth. This will also have beneficial effects due to the fact that orthopaedic implants typically undergo shear stress. This shear will put strain on the cells anchoring to the implant and therefore stimulate them to produce calcium and bone neo-formation. This will be increased further by having favourable load transfer through implant design and the use of low modulus materials such as titanium [4].

2.1.1 Anti-bacterial Surfaces

When a foreign body is implanted there is an associated increase in infection risk. It has been proven by Elek and Conen [34] that bacteria are able to colonise foreign material much more readily, where only 100 colony forming units (CFUs) were required for abscess formation. This is a >100,000-fold reduction compared with no foreign body being present. This is due to the immune response being impaired at the implant site and implant adhering biofilm production [35].

Anthony Gristina [36] coined the theory of "race to the surface". This theory suggests that after implantation of this foreign body, a race between tissue and bacterial cells for the colonisation of the surface occurs. It is hoped that the host's immune system is able to 'defend' the implant with a successful combination of implant integration and immune proficiency, which will result in an implant less susceptible to infection. However, if the host is unable to do this and the bacteria 'win' the race, the implant surface will get covered in a biofilm which will release bacterial toxins thus impairing host cell function.

Due to biofilm resistance to antibiotics, implant removal, debridement, and reimplantation is the only course of action, and will result in dire consequences for the patient [37–39].

Hospital-acquired infections in an average UK hospital with 76,053 admissions per year costs the NHS £11.9 million during this time [40]; and with some devices, especially cardiac/ventricular, high mortality rates occur once infection takes place [41].

Staphylococcus aureus (*S. aureus*) is a prominent human pathogen and is the most commonly passed on bacteria by direct contact within hospitals [42] and is also a common cause of community acquired infections [43]. It is also the main cause of orthopaedic implant-associated infections [44]. Not only this, but strains have developed which are resistant to many drugs, for example methicillin resistant *S. aureus* (MRSA) [43, 44], which make the treatment of these infections challenging, and presents a chance to lose the progress that we have made to be able to fight life-threatening diseases, prevent infections in patients who are immuno-compromised due to the treatment of cancer, and post-operative antibiotic use to prevent infection [45]. Because of this, it is vital that an alternative method to fight infectious disease is developed.

To this end, materials have been researched and developed to aid in implant integration, and one way to do this is by reducing bacterial colonisation. Both surface topography and chemistry influence the host cell and bacterial response to implant surfaces, where some surfaces are capable of preventing cellular/bacterial attachment, known as anti-fouling surfaces, and some surfaces are able to kill bacteria, known as anti-microbial surfaces [46].

2.1.1.1 Anti-fouling

Anti-fouling surfaces prevent the reversible to irreversible adhesion transition for the cells. This is typically done using 2 methods, either by reducing the adhesion between the surface and surface-binding proteins, or by providing an easy method for detachment of the cell from the protein layer at the surface under low shear [47].

The currently most adopted method to do this is by applying polymer coatings. Poly(ethylene glycol) (PEG) is the current benchmark due to its hydrophilic nature resulting from its low polymer-water interfacial energy (≈ 5 mJ m^{-2}). This means that when the surface contacts biological fluids, the surface will prevent protein and cellular adsorption [48]. But, it easily undergoes oxidative degradation [47].

However, polymers are much more susceptible to wear/damage, and bacteria are able to settle/colonise areas with these defects. A single bacterium has the potential to form a biofilm in less than 24 h [47], which will cause severe complications for the patient. Because of this, for biomedical applications, antimicrobial surfaces are better suited to produce a durable defence from bacterial colonisation, especially so for applications where motion occur.

2.1.1.2 Anti-microbial

Antimicrobial surfaces are able to kill microbes. Examples of this are applying surface topographical features which are able to penetrate/pierce bacterial cell walls, applying antimicrobial substances to be released such as antibiotics and/or silver, or the use of non-releasing antimicrobial surfaces such as photo-active metallic oxides or polycations [46].

A well-documented antimicrobial substance is silver, which in the presence of wa-

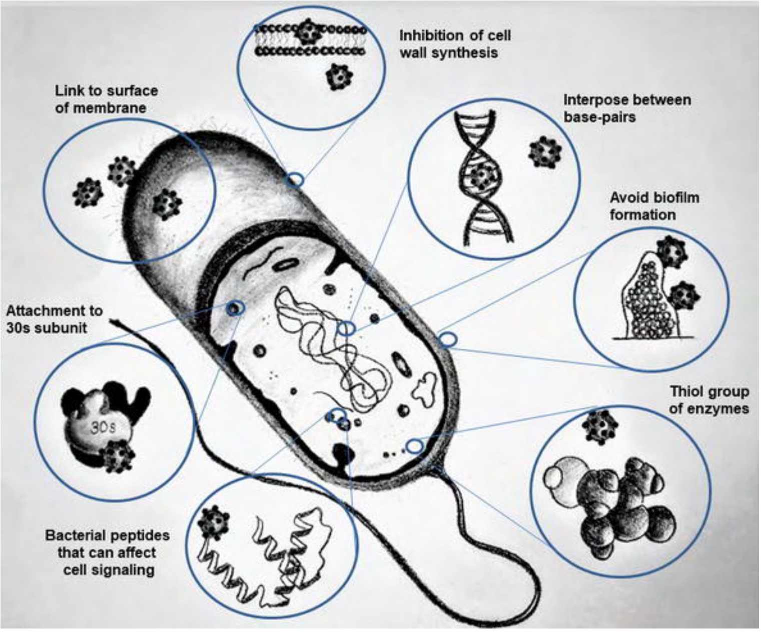

Figure 2.1: Schematic of the methods in which silver is able to interact with bacterial cells. Source: [51]

ter/body fluids releases silver cations (Ag^+). There are three mechanisms known for how the silver kills microbes. Firstly, Ag^+ has an affinity for sulfhydryl groups and proteins on cell membranes and can react with the peptidoglycan to form pores/puncture the cell wall. Secondly, Ag^+ is then able to alter bacterial cell membranes thus influencing permeability and causing intracellular uptake of Ag^+ which will disrupt respiration and metabolic pathways, thus generating reactive oxygen species (ROS). Finally, once inside the cells, the Ag^+ can interact with subcellular components and therefore impair the replication cycle [20, 21, 49, 50]. These are summarised in the schematic in figure 2.1.

The earliest use of silver for sterilisation is recorded to be in the Han Dynasty of China *circa.* 1500 BC. Silver vessels were often used in the Persian empire [50], and during the Roman empire silver coins were often put inside water vessels to make it drinkable [42].

The finding and subsequent uptake of antibiotics in the 20^{th} century halted the development of silver for therapeutic uses. But in recent years, antibiotic resistance has become a widespread issue [50]; resulting in the search for alternative methods to combat microbial infection and the re-evaluation of silver as a treatment.

Titanium oxide has received interest for its non-toxic, antimicrobial, and photo-catalytic properties. They have been embedded in clothing [52], used on biomedical implants [53–55], added into toothpastes [56], and has demonstrated their antimicrobial potential. Although the true mechanism for this is under debate [57], it is thought to be due to titania being semi-conducting. This means it has a valence band which is fully occupied with electrons, and an unoccupied conduction band, which is highly energetic. In titania the bandgap between these is 3.2 eV. Light illumination results in free electrons and electron-hole pairs being produced when the photo energy is equal or greater than the band gap (i.e. $\geq$ 3.2 eV) and hits the surface. This causes electron transfer from the valence band to the conduction band, which results in the positively charged holes in the valence band and the free electrons in the conduction band being formed. These electrons and holes will either recombine or, in the presence of electron or hydrogen scavengers, will cause a photocatalytic reaction. The conduction band electrons can reduce oxygen molecules to generate superoxides (O_2^-), and the valence band hole can react with water to generate hydroxyl radicals ($\cdot$OH). Although both of these are short lived, the reactive oxygen species (ROS) are very strong agents, impeding bacterial proliferation and survival [55, 57, 58].

More recently, palladium and palladium oxide have also been reported to demonstrate antimicrobial properties [22]. The first investigation of palladium nano-particles for their use as antibacterial agents was published in 2014 by Adams *et al.* [23]. They found a significant reduction in the number of colony forming units (CFUs) of both Escherichia coli (*E. coli*) and *S. aureus* after exposure to palladium nano-particles, although it was more limited for *E. coli*. As it is a recent discovery, further investigation is required to determine a potential mechanism for this action and for medical application [22].

2.1.2 Thermal Necrosis

Orthopaedic procedures will commonly involve the use of sawing/drilling bone, especially in the case of fracture repair. This causes trauma to the bone and the friction produced between the saw blade/drill bit and bone will inherently generate heat. If the heat production is too high (≈45 °C) [59, 60], it will kill the bone cells. This typically occurs in one of two ways: apoptosis or necrosis. The type of cell death will depend upon the severity of the trauma/injury, as summarised in figure 2.2. Apoptosis is controlled cell death, and follows a genetically controlled cascade comprising of shrinkage, blebbing, chromatin condensation, DNA fragmentation, and apoptotic body formation. Necrosis on the other hand occurs due to severe trauma/injury. It occurs due to the cell losing control of its ion flux, thus resulting in water uptake, swelling, and ultimately cytolysis [61]. In addition to this, it will result in blood coagulation and therefore cause blood vessel occlusion and ischemia to the area, thus resulting in infarction. This is known as thermal osteonecrosis, and is irreversible [59, 60].

This tissue damage leads to subsequent implant failure due to biomechanically reducing the stability and strength, which will delay repair and, due to the presence of necrotic tissue, increase the susceptibility to infections [60]. Additionally, it may cause mal-union and/or non-union fracture repair [59].

In orthopaedic surgery, high-speed drilling is the predominant cause of heat generation

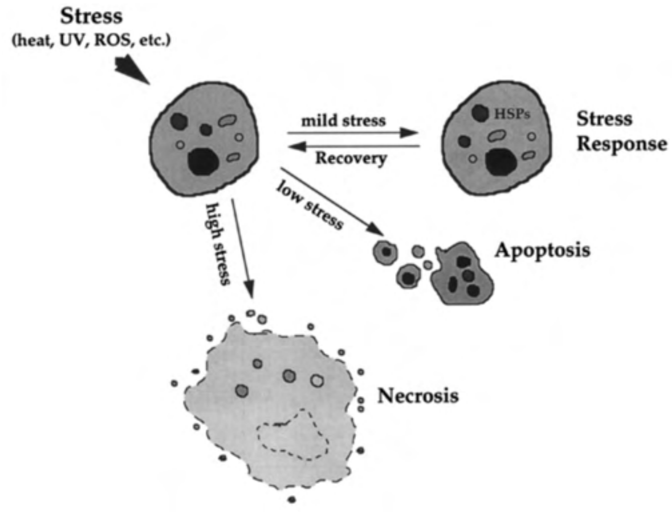

Figure 2.2: Schematic of the cell stress response. Mild stresses induce heat shock protein expression to refold misfolded proteins, and therefore is reversable (thermotolerance). More stress results in apoptosis (controlled death) and increasing further results in necrosis (uncontrolled death). Source: [61]

[62]. Methods to reduce this heat generation include changing the drilling parameters, where the prominent factors which influence the heat generation are the cortical bone thickness and density, drill speed, axial force, drill diameter, gradual vs one-step drilling [59], and irrigation of the surgical area with saline solution to reduce the temperature of the surgical tools/tissue [63].

In addition to this, the tribological performance of the drill tip is vital, as with increasing wear of the cutting edge, the amount of time required will increase [59], thus increasing the cumulative frictional energy and therefore resultant bone temperature. It has been seen that with increasing uses of the drill bit, the measured temperature in the bone increases [64].

2.1.3 Metallic Biomaterials

Metallic materials are widely used within the biomedical field, and especially so within orthopaedics. However, they are not without their drawbacks, for example stainless steel (SS), which although provides good mechanical properties such as ease of manufacture and low cost, it is only suitable for trauma/short-term use patients. This is because it has relatively poor corrosion resistance within the harsh conditions of the body, which coupled with its nickel content, makes it non-satisfactory for long-term use. As a replacement for this, cobalt-chromium (CoCr) has been used. This is due to its high corrosion and fatigue resistance [65]. However, it has a high modulus which results in the implant removing some/all of the load/stress away from the bone, and as bone responds to stress this reduction in stress will result in bone resorption [66, 67], and therefore leads to aseptic loosening of the implant.

A metal which has some key properties to help overcome these issues is titanium and its alloys, which will be discussed later in this chapter.

2.1.4 Fixation Devices

Bone healing is a multifactorial physiological process based on complex cellular and biomechanical interactions [68]. 5-10 % of fractures will heal abnormally, resulting in delays in or non-union healing [69]. Although bone fractures may not need reduction (setting), if they would: heal in a displaced position; sufficient healing would require prolonged immobility; the bone fracture displaced the bone too far for it to successfully unite; the fracture distorts vasculature or nerves; or once healed, the limb appearance may not be satisfactory even though functionality is correct [70], intervention will be required to restore correct functionality.

Once reduction is achieved, stability is required for the healing process. Some fractures are stable enough to not require additional support, however, if not, they will either require external or internal stabilisation. External fixation is achieved with either splints, casts, or braces. Internal fixation requires the use of screws, plates, pins, nails, wires etc. And in some instances, requires the use of an external frame to provide a rigid support to the bone [70, 71]. An example of this is with comminuted fractures, where the bone cannot anatomically repair [53, 72]. An example of an external fixation frame can be seen in figure 2.3, where a severe case had been presented and amputation recommended. After corticotomy (fragment removal leaving vessels and periosteum) and fixation, successful recovery occurred [73]. The way in which these work is by holding the bone in a fixed position to stabilise and align it via the utilisation of an external scaffold.

The same approach can be taken for bone lengthening. This can either be for cosmetic reasons to become taller, or for the treatment of patients with leg length discrepancy. This can occur due to either developmental conditions, damage, or disease affecting the growth plate, thus disrupting bone growth [74–76].

In some instances, birth/developmental bone growth disruptions can result in significant change to bone geometry. External fixation devices can be used to remodel this. A widely adopted example of this is the Ilizarov method [77]. It utilises the bone/tissue's ability to regenerate when stresses are applied to them; therefore, by using a fixation cage to apply tensional stresses, the limb is able to reconstruct in a minimally invasive way [78], especially for patients with complex deformities [79].

However, a problem with treatments such as this is the requirement for a direct

Figure 2.3: X-ray of a patient with a severe open comminuted tibia and fibula fracture (a), resulting in the need for debridement, resulting in a 13 cm gap, and subsequent external fixation (b). Source: [73]

implant-air interface. This frequently results in the development of pin-site infections. The presence of the pin prevents successful healing from this infection, so therefore daily pin site care and antibiotic prophylaxis is needed to lessen the infection risk. In addition to this, deep pin tract infections are common, and result in pin loosening, osteomyelitis, and ultimately the loss of fixation, resulting in the need for pin replacement [78, 80, 81].

2.2 Titanium and Titanium Alloys

Titanium and its alloys have properties which reduce the problems associated with SS and CoCr as they demonstrate high biocompatibility, high corrosion and fatigue resistance, low density (resulting in a high strength-to-weight ratio), and a low modulus of elasticity compared to the previously mentioned metals [24,82,83]. It has been speculated that titanium has a modulus of elasticity below the threshold of stress shielding [67]. This is important because bone responds to the amount of stress it experiences, and if the implant shields the stresses exposed to the bone, the bone will resorb as the body believes it is not needed. Therefore, titanium limits the amount of bone resorption around a load bearing implant, thus preventing aseptic loosening of said implant [84]. In addition to this, titanium also forms a passive oxide layer consisting primarily of TiO_2. This is what provides the high corrosion resistance and biocompatibility associated with the material due to it acting as a barrier to ion diffusion [1, 7]. However, this natural oxide layer is very thin (≈ 3 nm) and when it is in contact with counterpart surfaces in motion is easily damaged/removed [4].

2.2.1 History

Titanium is present throughout the universe and has been found in stars, meteorites, on the Moon, and in the Earth's crust. As the Earth's crust consists of approximately 0.6 % titanium, it is the fourth most abundant of the metals [4, 15, 85, 86].

Although it is abundant, it was only discovered relatively recently, where in 1791 William Gregor examined magnetic sand in a local river in Helford, Cornwall. He extracted black sand from it, since known as "ilmenite", and by removing the iron and treating it with hydrochloric acid he produced an impure oxide [4, 85–87].

A few years later Martin Heinrich Klaproth isolated titanium oxide from a mineral since known as "rutile". He named it titanium after the giants of Greek mythology, the *Τιτᾶνες* (Titans), as they were detained in the Earth's crust by their father and the ore being difficult to extract from the crust [4, 87, 88].

It posed a challenge to isolate titanium, so much so that it took more than 100 years. Matthew Albert Hunter managed it in 1910 by heating titanium tetrachloride with sodium at 800 °C and high pressure, known as the Hunter process. After this, Wilhelm Justin Kroll, the father of the titanium industry, in 1932 found a way to produce large quantities by reducing the titanium tetrachloride with calcium. He then went on to develop a method to commercially produce titanium during WWII by changing the reducing agent to magnesium (since known as the Kroll process). This is still the most used method [4, 87, 89].

Due to their high strength-to-weight ratio and superior corrosion resistance, titanium alloys have been adopted for a wide range of applications. Especially within the aerospace industry for which Ti-6Al-4V was the first developed workhorse [90]. Since then, as previously mentioned, it has been shown to have attractive and beneficial effects within the biomedical field in terms of satisfactory biocompatibility and desirable osseointegration for orthopaedic and dental implants. In addition to this, its low elastic modulus aids in reducing the stress-shielding phenomenon and therefore could reduce the number of failures due to aseptic loosening of load-bearing prosthesis [1, 4, 65].

2.2.2 Physical Metallurgy

Titanium's stable crystal structure is hexagonal close packed (hcp), known as the α-phase, but when the temperature rises above ≈885 °C there is an allotropic transformation to body centred cubic (bcc), known as the β-phase, up until its melting temperature of 1668 °C. Due to this allotropic change, depending on elemental composition, there exists different classifications: α, near-α, $\alpha + \beta$, stable-β, and metastable-β [1, 91, 92].

It is possible to control the micro-structure of titanium by alloying it with various phase stabilisers which enable the α and/or β phases to be present at altered temperatures as is shown in the schematic representation in figure 2.4. The stabilising elements are classified as either α or β depending on whether they increase or decrease the α/β transition temperature [93]. Most α alloys will contain some β phase, mostly due to tramp iron during manufacture [92].

An example of an α stabiliser is the substitutional element aluminium. Aluminium is soluble in both α- and β- titanium. Because of this solubility in both phases, it is the most commonly used stabiliser. As well as aluminium, interstitial elements oxygen, nitrogen, and carbon are also strong α stabilisers. Oxygen is commonly used to increase the strength of titanium, which is how the different grades of commercially pure (cp)-Ti are produced.

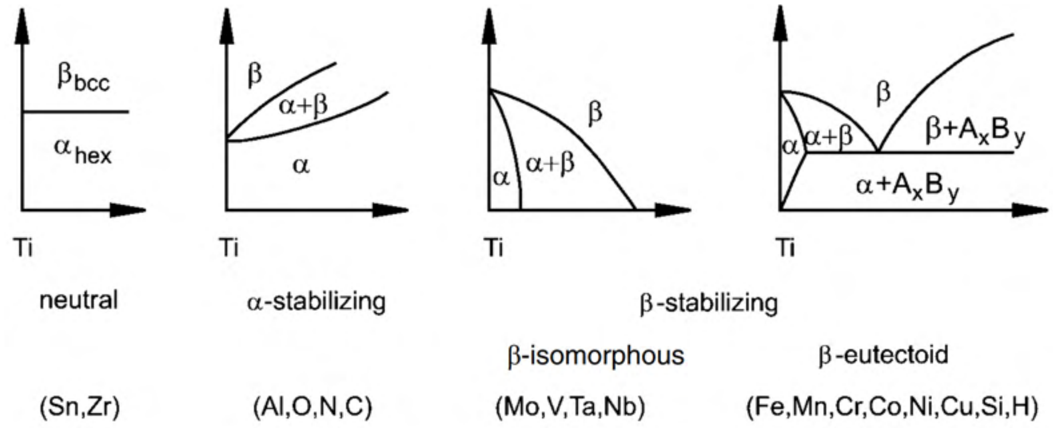

Figure 2.4: Schematic of the effect of alloying element on the titanium phase diagram. Source: [4]

Depending upon the concentration of these stabilisers, where increasing concentration increases their effect, they will increase the $\alpha + \alpha/\beta$ transus temperature [83]. The solutes are typically non-transition metals and, when dissolved with titanium, very few electrons are in the Fermi level, so most are in the lower bands. Because of this, titanium's d-band electrons will avoid the α-stabiliser's atoms, therefore diluting the sublattice of titanium and directionally strengthening the titanium-titanium bonds thus preserving the hcp structure. This α-phase yields good weldability, mechanical properties, and excellent corrosion resistance [33, 91, 94].

Depending upon their binary phase diagrams, β stabilisers are divided into 2 categories: isomorphous and eutectoid. These are shown in figure 2.4. Isomorphous stabilisers are bcc like β titanium, and the most commonly used isomorphous stabilisers are vanadium, molybdenum, and niobium. Chromium, iron, and silicon are commonly used eutectoid β stabilisers, although these types are not used as often as isomorphous stabilisers [83, 95]. Isomorphous elements are fully soluble in β titanium and have limited solubility in α titanium. Eutectoid elements have little solubility in β and form intermetallics by eutectoid decomposition of β [95]. The addition of β stabilisers reduces the α to β transus temperature, and therefore increases the strength of the alloy at lower temperatures due to the β-phase's higher strength. They are however meta-stable, and either cold working or elevating their temperature will result in partial transformation into α phase, which results in strength levels close to those of α+β [33, 91, 94].

By using a combination of 1 or more α- and β- stabilisers a two-phase system is produced, known as the α+β phase. The mixture will depend upon the concentrations of each stabiliser that is present. α+β demonstrates a good balance of strength and ductility and provides good fabrication properties. Because of this, these are the most common type of titanium used [33, 86, 91, 94]. However, if these titanium parts are not produced in a controlled manner, the temperature variations across the piece will result in a non-uniform α- and β- phase distribution. To help minimise this, the part is usually heated above the β-transus temperature. However, during normal cooling, equilibrium conditions are met, so α-phase forms within the β-grain boundaries and forms platelet α within the β-grains. The growth within the grain boundaries has negative consequences on the performance of the titanium piece. In order to limit this, a high cooling rate is utilised to suppress α formation [86, 94].

Currently three compositions are used within the body: cp-Ti, Ti-6Al-4V (Ti64), and Ti-6Al-7Nb (Ti67) [1, 33].

2.2.3 Niobium Containing Alloys

Despite Ti64's good mechanical properties, and therefore widespread adoption for implantation, it is not without issues. It has been shown that the release of aluminium and especially vanadium ions may contribute to long-term health issues, for example Alzheimer's, peripheral neuropathy, and osteomalacia [96,97]. Because of this, alternative alloys with more biocompatible elements are being developed and researched. An alloy of great interest for this within the biomedical field is Ti67 [98–100].

Sulzer Winterthur developed this alloy with IMI Titanium Ltd for use in medical and surgical devices, and it was released for sale in 1990. The microstructure and mechanical properties were optimised to be closely matched to that of the Ti64 alloy [101]. Along with titanium, niobium also self-passivates. Because of this, if the niobium ions were released into the host, they, like titanium ions, would have limited negative effects [102].

Niobium significantly increases the oxidation resistance of the alloy [98,102–104], thus resulting in different oxide growth characteristics compared with Ti64. It has been shown that niobium forms solid-solution within rutile [104]. Because of this, it decreases the oxygen vacancies within the rutile, and as rutile grows by oxygen diffusion through the oxide layer via vacancy diffusion this impedes mass transfer, and therefore increases oxidation resistance [98,100].

Niobium also increases the thermodynamic activity of aluminium compared with titanium [104]; therefore, favouring the formation of alumina over titania [104–106].

2.3 Tribology

The term tribology originates from the Greek *τρίβω* (tribos), meaning "rubbing" [107,108]. It is the science of wear, friction, and lubrication, and includes how interacting surfaces and their tribo-elements behave in relative motion [109]. It was first used in the United Kingdom within the Jost Report, which was conducted in 1996. It evaluated the amount of money lost annually to friction and wear [108].

Materials have multiple characteristics which will affect both the wear and friction considerably. These are surface chemistry, micro-structure, energy, hardness, and roughness. Other than surface roughness, these are inter-dependent and may be altered with chemical, thermal, and/or mechanical exposure during service. This potentially results in component degradation, thus causing premature end of service; or if purposely exposed in the form of material treatments, can drastically improve the tribological performance and increase service life of components [110].

The predominate material characteristic which determines its tribological performance is the chemical composition. This is because alterations in this will affect the phase/grain structure, and therefore ultimately cause alterations in surface hardness and energy. In addition to this, composition changes at the surface may cause solid solution hardening, precipitation, and dispersion hardening [110].

2.3.1 Friction

Friction force is the resistance that occurs when one body moves over another. This encompasses both sliding and rolling motions, and although they are not mutually exclusive as rolling almost always involves sliding, the distinction between them is important [111].

With both sliding and rolling wear, in order to move the counterpart over the material surface it is necessary to use a tangential force (F). The ratio between this and the normal load (W) is the friction of coefficient (μ), demonstrated in equation 2.1. [108, 111]

$$\mu = \frac{F}{W} \tag{2.1}$$

A method to reduce the amount of friction present between mating surfaces is the use of a lubricant. Lubricant systems function by having a lower shear strength than either of the sliding surfaces [111]. Many different types of lubricants exist, being either gaseous, liquid, or solid [111–113].

Viscosity of the lubricant plays a crucial role in its successfulness for its intended application. Although mineral oil is a common choice, it may not be appropriate depending upon the application parameters, such as load, speed, temperature, and location [113].

Methods such as electroplating or physical vapour deposition can be utilised to apply solid lubricant films of soft metals; where coatings such as lead, tin, copper, gold, silver, etc. are often used due to their low shear strength, ease of bonding, and high thermal conductivity [113]. However, their lubricating effect is limited by their respective melting points [112].

Additionally, some substrates are used which have indirect lubricating effects due to their high hardness. Examples of these are oxides, nitrides, and diamond-like carbon (DLC). These can prevent component seizure and significantly increase the wear resistance of components [112, 114, 115].

2.3.2 Wear

Wear involves the removal of the functional surface of a material and is one of the most commonly experienced surface degradation mechanisms. The effect that this removal has can vary from a change of surface roughness to, with increasing removal, a change in component size/shape which ultimately weakens the component and makes it prone to mechanical failure during service [110, 116].

Common mechanisms for wear of materials at these surfaces are adhesion, abrasion, galling, fatigue, fretting, and corrosion. The most common of which being from adhesion, abrasion, and corrosion, but depending on the component application, which mechanism dominates will vary [110, 116–118].

2.3.2.1 Adhesive wear

When the direct metal-metal contact via asperities (peaks and troughs) at the surface are in relative motion adhesive wear occurs. These asperities are always present, no matter how the material has been manufactured, where procedures such as polishing are only able to minimise the size of these asperities. Due to the fact that mating surfaces are only in contact at these asperities, the true stress is actually 100-1000x that of the nominal stress [110]. This leads to plastic deformation of the asperities, resulting in cold bonds forming. This is caused by three phenomena: the mating surfaces forming mechanical joints during deformation, which also causes work-hardening and therefore a harder layer than the sub-surface; free-electron transfer forming metallic bonds; inter-facial diffusion of alloying elements with elevated temperatures if the surfaces are mated for prolonged time periods. The bond that forms will not influence the surfaces until relative motion occurs, after which the bond will be broken. The bond will break at either the surface-surface interface, or at the subsurface layer of one of the materials. Typically, the latter occurs due to the work-hardening effect causing the inter-facial bonds to be stronger. This results in a small piece of material being detached from the subsurface of the weaker material [110, 117, 119], as demonstrated in figure 2.5, where material B is the weaker material.

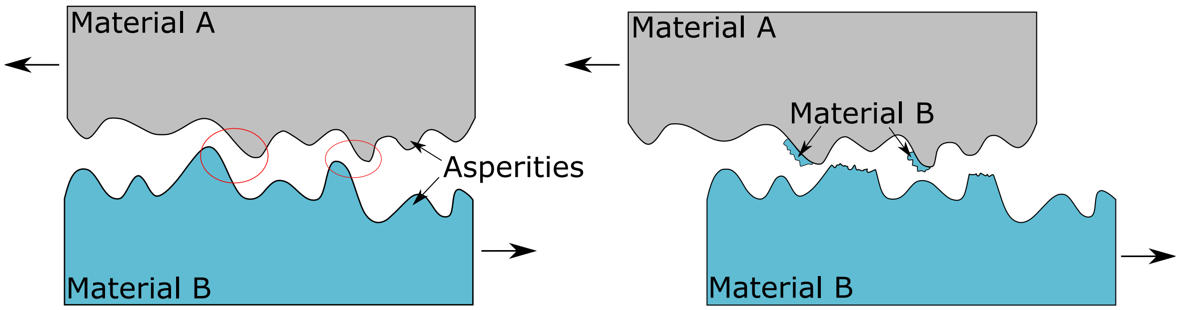

Figure 2.5: Schematic of adhesive wear of a surface.

2.3.2.2 Abrasive wear

When interacting surfaces are mated with hard particles it produces one of the most severe types of wear, known as abrasive wear. Simplified, the hard particles act as a fine cutting edge and cause micro-cutting of the surface. There are 3 ways that this occurs: ploughing, wedge formation, and cutting depending upon the hardness and depth of the particles. Ploughing predominates with ductile materials and increasing hardness results in cutting being the predominant mode. Increasing particle size results in the transition from ploughing, to wedge formation, to cutting [120]. The mechanisms in which this takes place are plastic deformation, leading onto work-hardening, followed by fatigue, grain debonding, and brittle fracture [110]. If the wearing surface is a hard material, when it wears it can transition from two-body to three-body abrasion due to the wear debris acting as hard third bodies. These will act to cause severe abrasive wear [117]. A schematic of the initial stages of this abrasive wear to produce hard third-body particles is shown in figure 2.6.

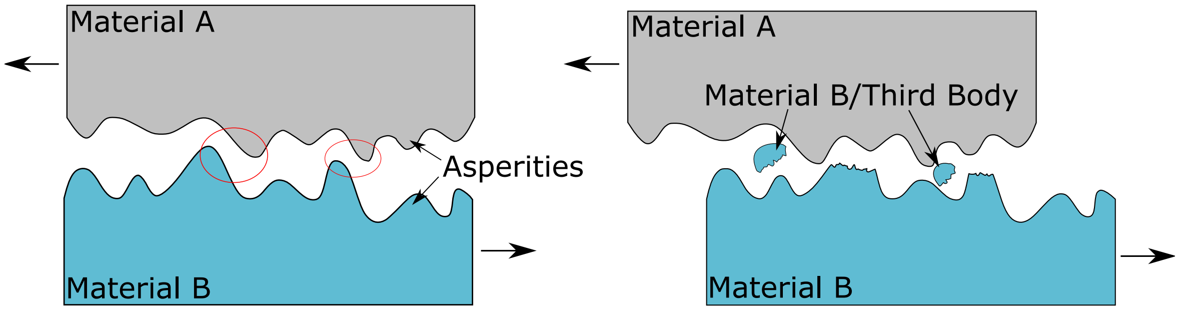

Figure 2.6: Schematic of the initial stages of abrasive wear of a surface. The third body acts as an abrasive particle to lead to abrasive wear.

2.3.3 Tribology of Titanium

Titanium and its alloys have relatively poor tribological properties as they are prone to galling. This is due to titanium's high reactivity, so therefore sliding surfaces adhere to one another, which causes seizure. In addition to this, the release of titanium and its alloy's constituent element's ions due to dissolution of wear particles may lead to tissue discolouration and/or illicit an adverse inflammatory response, which will cause inflammation and its associated pain. This will eventually cascade to aseptic implant loosening [82, 91]. In addition to these local implications, the release of ions into the surrounding tissue can result in systemic implications. This is because if the particles/ions diffuse through the tissue, they can get distributed through the lymphatic system, and therefore accumulate in the liver and spleen [121, 122]. The presence of vanadium within the Ti64 alloy make the risk of this process worse, due to the fact that vanadium is cytotoxic [123], so if it were to get released into the surrounding tissue, it would be toxic to the host's cells. In addition this, as previously mentioned, their release may contribute to long-term health issues such as Alzheimer's, peripheral neuropathy, and osteomalacia [96, 97].

A method to combine the relatively low modulus property of titanium with the relatively high wear resistance property of CoCr is to use a modular medical device, for example hip implants where the stem is made of titanium and the head CoCr. However, although titanium's spontaneous TiO_2 oxide provides excellent corrosion resistance, at the Ti-CoCr interface, fretting of the relatively soft titanium occurs, thus removing said oxide and when this is coupled with the lack of oxygen being present meaning this oxide is not able to reform, crevice corrosion occurs. This therefore leads to implant failure [124,125].

Because of this, titanium has limited use for applications where relative motion between material surfaces occur, such as screws, fixation pins, hip, knee, and spinal implants [126, 127], and metal-on-metal hip implants have been banned from use [128]. These problems result in a restriction in the use of titanium for orthopaedic biomedical implants. Therefore, the generation of a method to overcome the poor tribological performance of titanium could result in the re-evaluation of it as a material choice for these.

2.4 Roughness

Irrespective of precision, no method of machining can yield a molecularly flat surface [129]. Macro and micro/nano topographical features (surface textures) are important considerations when choosing and designing parts for satisfactory performance [119,130].

Depending upon the processing methods, surfaces will either be isotropic or anisotropic, and Gaussian or non-Gaussian. For example, surfaces produced by processes such as shot peening will be Gaussian due to the cumulative random local events; and extreme value processes such as grinding/milling will typically produce anisotropic non-Gaussian sur-

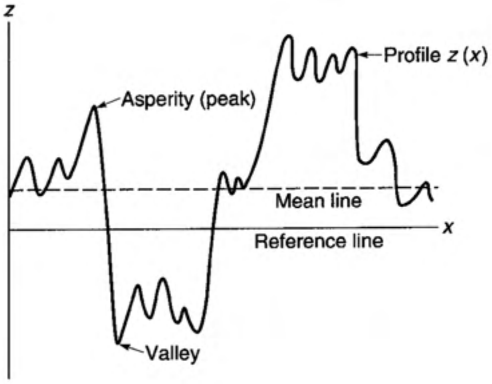

Figure 2.7: A surface profile, with the mean profile line and a reference line labelled. The deviation of the mean line from the reference line makes up the Ra value. Source: [130]

faces [130].

The most used parameter of roughness is the arithmetical mean deviation (Ra). This is an assessment of the variation of peak heights from a reference line to determine the average absolute values [131, 132], a schematic of which can be seen in figure 2.7.

2.4.1 Biological Response

A key factor for the adherence of cells is the surface's nanostructure [133]. This has a significant effect on cellular signalling, and influences their morphology, orientation, proliferation, and subsequent differentiation [31].

This is because cellular adhesion sites are in the 5-200 nm scale; and eukaryotic and bacterial cells are known to respond to external stimuli such as spatial arrangement/confinement and external environmental cues. So if surface features were within this range and/or promoted orientation/arrangement it will influence their adhesion potential. In addition to this, bacterial cells of similar size to topographical features have an increase in binding strength due to the associated increase in contact area [134, 135]. Once strong adhesion has occurred, subsequent proliferation and, in the case of bacterial

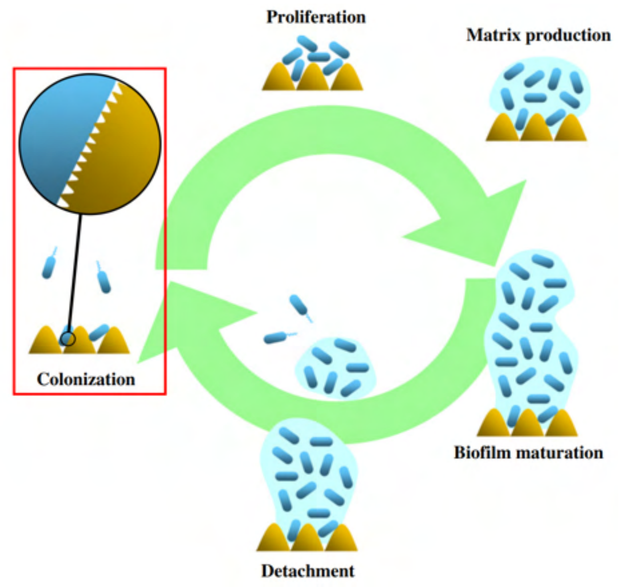

Figure 2.8: Schematic of bacterial colonisation on a rough surface, leading to biofilm formation and its life cycle. Source: [133]

cells, biofilm formation (figure 2.8), become easy. If the surface of an implant promotes bacterial adhesion, it would be detrimental to its performance.

Although a large number of investigations have taken place to study the influence of increasing surface roughness on bacterial attachment, no clear consensus has been drawn [134].

2.4.2 Tribological Response

The surface roughness of materials influences the friction and wear that they experience. This is due to the fact that with increasing roughness, more micro -peaks and -troughs are present. These lead to an increase in mechanical interlocking between mating surfaces, thus increasing frictional forces and likelihood of adhesive wear occurring [110].

If the wear mechanism remains the same, the surface roughness changes during the initial stages of wear, after which it stabilises to produce a wear scar. In addition to this, an increase in roughness typically increases the wear debris particle size, thus increasing the wear rate due to causing more severe abrasive wear [110].

2.5 Surface Engineering

There have been many studies into finding a solution to the problems discussed so far, where surface engineering best enables an improvement in tribological properties whilst maintaining the other superior mechanical properties present with titanium and its alloys.

Surface engineering can be divided into two groups, surface coatings and surface modification.

2.5.1 Surface Coating

An example of surface coating is titanium-nitride (TiN) coatings. A study by van Hove *et al.* [136] found that these showed to be biocompatible, whilst improving the wear resistance and having a low coefficient of friction. However, due to the large difference in elastic modulus between the TiN coating and the Ti6Al4V, debonding occurred on these samples when prepared by physical vapour deposition (PVD), which will potentially result in a cascade of abrasive wear and ultimately lead to failure. This is the main drawback with surface coating technologies, where typically [137–142] it is challenging to produce coatings which have good substrate bonding.

Micro-arc oxidation (MOA) is a process whereby a thick and hard ceramic oxide coating is able to be produced on the surface of titanium surfaces using electro-chemical oxidation and spark discharge [143–145]. However, these surfaces are porous, which leads to a reduced tribological performance. This is caused by cracks forming due to the increased stresses associated with the pores, leading to the ceramic surface-material being removed, and therefore causing severe abrasive wear. A method to try and overcome this is to polish the surface, as shown by Fei *et al.* [144], who found that removing the protruding ceramic particles via polishing eliminated the cracking of the surface and therefore improved the tribological performance. However, adding this extra step to the process is not suitable for applications with complex geometries commonly found within the medical industry.

In an attempt to try and overcome this poor tribological performance, a study by Muhaffel *et al.* [145] looked at producing composite MOA treatments. This was achieved by using additives in the electrolyte of Al_2O_3 and ZrO_2, which they hoped would yield an improved wear performance vs the traditional MOA treatment. However, they found that the additive treatments had either similar or worse wear performance vs the traditional MOA treatment. This is due to the Al_2O_3 additives producing oxides prone to spallation, especially with increasing load, and the ZrO_2 additives producing surfaces prone to cracking.

Another example of surface coating is physical vapour deposition (PVD), which will be discussed in the following section.

2.5.1.1 Physical vapour deposition (PVD)

PVD is a thin-film surface coating technology. It is split into two categories: thermal evaporation, and sputtering [146].

The particles for thermal evaporation deposition are transformed from the solid/liquid to gaseous state by a physical process [147]. Coating thickness can range from a few atomic layers to several microns [148] and occurs in a vacuum chamber typically below 10^{-1} mbar to reduce scattering [147, 149], and hence is typically termed vacuum deposition [146].

Faraday produced the first thin film by evaporation in 1852 by exploding wires under vacuum [150], and ion plating is the first important process from this development [151]. The process was first reported and patented in 1938 by Berghaus [152]; but it was not fully described until 1973 where Mattox provided reports of the modern form of the process [153]. High rate, full density coatings were developed in the 1960s and enabled dense, high-purity metal/alloy coatings to be produced [154].

The vaporisation occurs due to the kinetic energy increase associated with heating: with increasing temperature, more atoms overcome the separation energy and are able to evaporate. The amount of vaporisation depends on the elements present, and is made up of atoms, molecules, and clusters [147]. The heat for this is most commonly provided by resistive heating, however, this process cannot vaporise high melting point materials and has limited control. A method to improve on thermal evaporation is the use of pulsed lasers. This utilises high-power pulsed lasers to ablate/vaporise the surface, which then gets coated onto nearby surfaces producing thin films. Although this means compounds of a controlled composition can be coated, it does not yield a uniform coating and micro-globules are removed from the surface [146, 155].

Sputtering is caused by bombardment of energetic particles to a solid surface, causing surface atoms to be scattered due to the collisions, as demonstrated in figure 2.9. If the bombardment is onto a thin foil, it is possible for them to be transmitted through, known as transmission sputtering [146].

Sputtering of thin films is carried out using either dc diodes, rf diodes, magnetron, or ion beams [156]. Dc sputtering is the simplest of these, as is simply a cold cathode

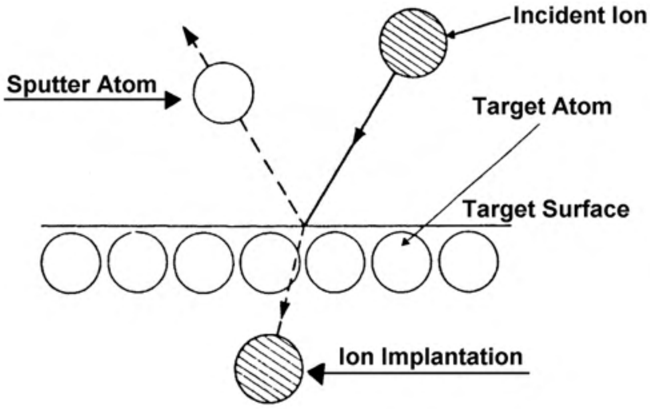

Figure 2.9: Schematic diagram of physical sputtering. Source: [146]

with the target materials on, and an anode. The samples to be coated are placed on the anode, and the chamber is filled with sputtering gas, typically argon. Glow discharge occurs between the electrodes, and the generated Ar^+ accelerate towards to cathode. This causes sputtering, and results in thin-film deposition on the samples. Since this process requires current flow, it can only be used with metallic electrodes. This is because if the target material were insulating it would result in a charge build-up of the positive ions. The implementation of rf voltage to the target enables the glow discharge to stabilise, and results in direct sputtering from the insulator target [146, 157–159].

Magnetron sputtering is an advanced sputtering technique. It involves a magnetic field over the cathode/glow discharge parallel to the target surface. This results in the electrons within the glow discharge to move in a cycloid motion, as demonstrated in figure 2.10. The field is positioned so that it forms a closed-field loop with the electron drifts; thus, increasing collisions between the electrons and gas molecules, and enables a reduced sputtering pressure. This increases the plasma density and therefore current density at the target, which results in an increased sputtering rate. Since the sputtering pressure is lower, the sputtered particles move through the space without collisions and therefore

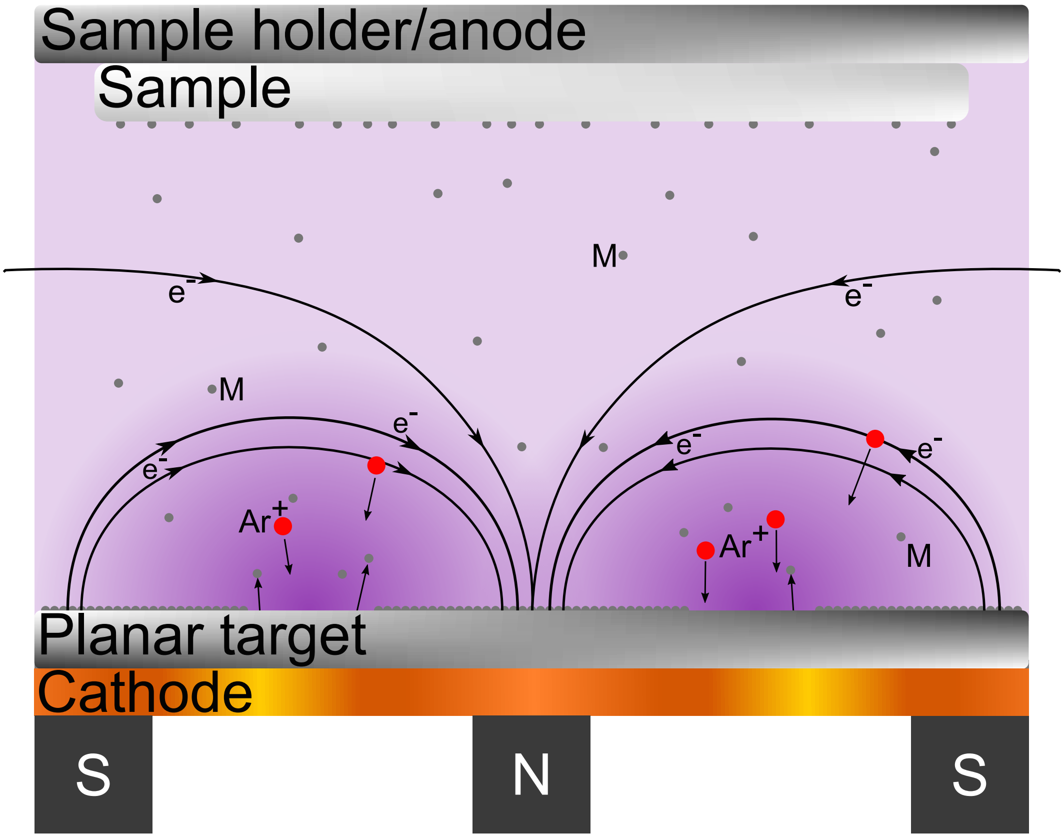

Figure 2.10: Schematic diagram of the workings of a closed-field unbalanced magnetron sputtering instrument. The grey circles (labelled M) denote the vaporised target material.

yields a high deposition rate [146, 159, 160].

2.5.2 Surface Modification

Taking advantage of titanium's highly reactive surface characteristics, diffusion-based treatments can be utilised to modify the surface in order to improve the durability of the material [161]. Early work on carburising and boronising [162] indicated that such treatments can produce a thin, brittle, but very hard, compound layer with poor load bearing capacity. This is mainly due the very low solid solubility of these elements, and hence extremely shallow diffusion zone.

A later example of surface modification is glow-discharge nitriding. However, a study by Bacci *et al.* [163] found that although nitriding of Ti-6Al-4V resulted in a hard diffusion/compound layer, it yielded unsatisfactory tribological properties due to microfragmentation of this nitrided layer, and therefore resulted in high wear caused by third-body abrasion mechanisms. In addition to this, Lanagan *et al.* [164] also reported that due to the associated high treatment temperatures (800-1000 °C), the fatigue strength was reduced by 20-35 %.

Another example of surface modification is ceramic conversion treatment (CCT), which will be discussed in the following section.

2.6 Ceramic Conversion Treatment

CCT is a thermo-chemical process based on thermal oxidation (TO). As mentioned previously, titanium naturally forms a thin passive titanium dioxide (TiO_2) layer on its surface at low temperatures. However, due to titanium oxide being an n-type semiconductor [165], when titanium is subject to high temperatures in an oxygen rich atmosphere, oxygen is able to diffuse through this TiO_2 layer to the substrate-oxide interface and react with the titanium substrate *in situ* to form a thicker TiO_2, hence termed ceramic conversion. This TiO_2 successfully grows as a hard surface layer without scaling/surface damage, and has low friction and high wear/corrosion resistance. Ceramic conversion describes the result of the thermal oxidation process, and therefore is how it is termed from this point onwards [15, 99, 166].

In addition to this oxide layer formation, the oxygen is able to diffuse into the substrate's interstitial sites below this oxide, thus causing interstitial hardening, known as the oxygen diffusion zone (ODZ) [99, 166]. A theoretical study by Wendt *et al.* [167]

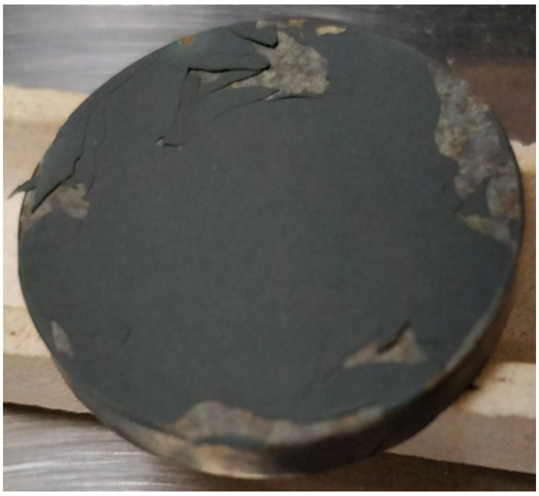

Figure 2.11: Spallated surface oxide on a Ti64 sample treated at 800 °C.

demonstrated that interstitial titanium ions near reduced titania forms a gap state, which is capable of providing electrons for adsorption and dissociation of O_2 on TiO_2.

This TiO_2 exists as three polymorphs, stabile rutile, meta-stable anatase, and brookite, although the two of importance are rutile and anatase as brookite is so difficult to synthesise so is rarely studied [168]. A thick TiO_2 layer can reduce the amount of metal ion released into the surrounding tissue [82], therefore helping reduce clinical complications.

The treatment conditions need to be carefully selected as high temperatures (≈800 °C) and/or long treatment times lead to an oxide that is too thick, which leads to an increased Ti-rutile ratio; because of this and its associated lattice mismatch, when coupled with the difference of thermal expansion coefficients, will cause de-bonding from the substrate (spallation) [169, 170], an example of which can be seen in figure 2.11. This also occurs even for short treatment durations at high temperatures, as it results in high residual stresses at the bulk-oxide interface [4]. Additionally, low treatment temperatures and durations yields an oxide too thin for tribological applications [169].

When heating titanium above ≈600 °C it causes a non-reversible phase transformation of the oxide from anatase to rutile [168]. This rutile is a lubricious oxide [166] and is able to stimulate the production of poorly crystalline bone apatite. This is due to rutile's iso-electric point of pH5-6 being more acidic than that of the body (pH≈7.4), resulting in rutile releasing H^+ ions and forming negative TiO^- groups. These groups attract Ca^{2+} ions to the surface and form calcium titanate, therefore attracting PO_4^{3+} ions to form unstable calcium phosphate, which then gets converted into the bone apatite [171].

As a method to better understand this oxidation mechanism, a study by Zhang *et al.* [165] applied a thin layer of gold (Au) prior to CCT. However, they found that this Au layer accelerated the formation of the TiO_2 layer and altered the oxidation mechanism. They found it to increase the oxide-substrate interface quality but reduce the oxygen hardened zone underneath said oxide. It was postulated that the mechanism for this involved the Au acting to activate titanium diffusion through the Au and react with the oxygen. However, due to the reduced ODZ beneath the oxide it was speculated that the higher rate of outward titanium diffusion resulted in a reduction in oxygen inward diffusion into the substrate.

Due to its high reactivity, titanium is highly susceptible to contaminants, which negatively impacts the treatment quality, as demonstrated in figure 2.12, so care is needed during material preparation for treatment in order to achieve high quality layers.

A drawback to the CCT process is that in order for it to produce layers useful for improving durability (2-5 μm) it requires long treatment durations of 80+ hours [14, 16]. This is both time and energy consuming, so the application of catalysts in order to improve upon the CCT process is merited.

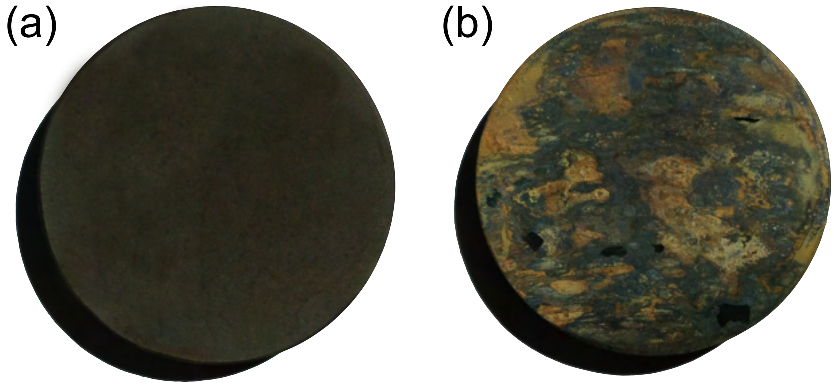

Figure 2.12: Surface condition of a non-contaminated (a) and contaminated (b) Ti64 CCT treatment. Note (a) shows a uniform treatment, but (b) demonstrates regions of varying colours

2.7 Catalysis

Catalysis, from the Greek words $\kappa\alpha\tau\alpha$ (kata) and $\lambda\nu\sigma\iota\zeta$ (lúsis), which means "wholly loosening", was first coined in 1836 by Berzelius describing the "decomposition of bodies" using a "catalytic force". Armstrong later (1885) proposed the term catalyst, which participates in a reaction without itself being consumed by altering the activation energy for a given reaction (figure 2.13) and therefore altering the rate of reaction. The way in which it does this is by forming a transition state which has a lower potential energy. This offers an opportunity to reduce both the financial and environmental cost of reactions/industrial processes [172–175].

2.7.1 Noble Catalysts

The efficiency of catalytic reactions using solids is determined by how their surfaces are able to convert reactants into adsorbed forms capable of producing the desired product. Group 8-10 metals are proficient at hydrogen dissociation, whereas group 11 are only able

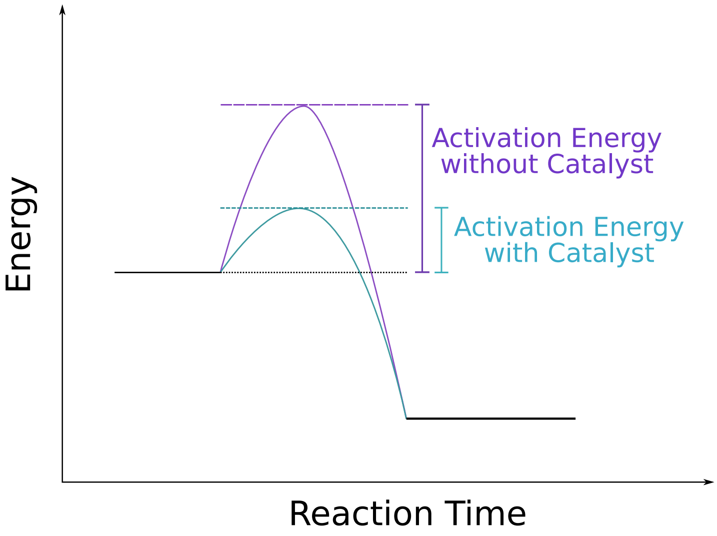

Figure 2.13: Schematic of a potential energy curve of a catalysed reaction.

to weakly adsorb hydrogen so are not ideal for this application. Additionally, the base metals within these groups are readily oxidised themselves so cannot be used for oxidation catalysis, so only the noble metals within these groups can be used for this. [176]

A lot of work has been carried out to investigate the use of noble metals for the oxidation of CO for many applications ranging from the manufacture of methanol, to their addition into automotive exhausts to reduce emissions contributing to global warming. This work typically has the metals of interest supported on oxides such as alumina (Al_2O_3) and titania (TiO_2) [17–19].

Although gold was initially believed to be inactive and not useful for catalysis [177], it was discovered that if it was finely dispersed as nanoparticles on metal oxide supports it is a very active CO oxidation catalyst [178]. This is attractive for air purification and helping reduce environmental concerns [179].

As silver is more economical than the other transition metals, is environmentally safe, and is stable, it is of high interest for the catalysis of processes. It is used in two main areas: heterogeneous oxidation, and homogeneous silver-mediated reactions. It was first

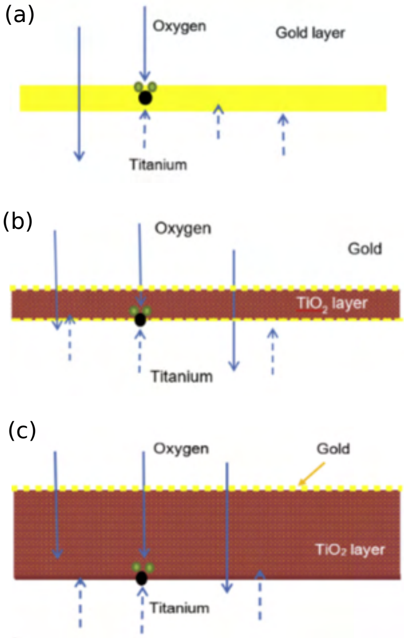

Figure 2.14: Schematic of a proposed mechanism of the 'catalytic' thermal oxidation of Ti-6Al-4V with gold pre-deposition. Source: [182]

used as a catalyst in 1933 to oxidise ethylene, and has since been used for a number of reactions [180].

Gold [165, 181, 182] and silver [183, 184] have been shown to catalyse the thermal oxidation of titanium alloy Ti-6Al-4V, producing thick and dense titanium oxide layers which are significantly more durable than without the use of the catalytic dopant.

Zhang *et al.* [182] proposed a potential mechanism for the catalytic effect of gold on CCT, which can be seen in figure 2.14. It was proposed that in the early oxidation stages the presence of a gold layer increases titanium cation outward diffusion (a). Increasing treatment duration results in the gold layer being dispersed throughout the oxide (b), thus reducing the catalytic potential of the element. Further treatment duration results in a thicker oxide layer, which therefore further impedes diffusion, thus further reducing the oxidation rate compared with the early stages.

2.7.2 Bimetallic Catalysts

Bimetallic surfaces show unique properties compared with their constituent elements. This is due to the interaction of electrons between the metals, for example d-band, or charge changes resulting from bonding, and modifications to active sites and morphologies. These changes will alter the reactivity of the catalyst [185–187].

The selectivity of a catalyst is controlled by the ensemble. The ensemble is the number of active sites on the surface required for a particular reaction [186]. In addition to this, atomic distribution will have a significant influence on catalytic performance due to changes in the crystal architecture, therefore, changes in geometry can occur depending upon which elements are present and how they are arranged [188]. This enables control of the catalyst's roles.

If one metallic layer covers the other, the second layer will grow on all faces of the first. This will form the core-shell/egg-shell structure. If the active shell is covering, and therefore supported by, another metal it produces a high efficiency catalytic system. However, since the reaction typically only occurs at the outermost layer (with some influence from the immediately underlying layers), the support metal is typically wasted. If this was a noble-noble system this would cause a problem due to the associated high costs [188–190].

Homogeneous distribution of two metals will produce an alloyed structure. This is typically during wet-chemical production, where the metals will nucleate separately. This leads to individual activity, where the properties are assumed to be a linear combination of the individual metals, but they can also interact to yield different reactivity [188, 191].

Chapter 3

Experimental Procedure

3.1 Material and Sample Preparation

Coupon discs were cut from a 1-inch diameter bar of Ti-6Al-4V (Ti64), 4mm thick, and a 20 cm diameter bar of Ti-6Al-7Nb (Ti67) diameter, 3 mm thick, using Struers Acuom 30 with a silicon carbide blade. Their compositions are summarised in table 3.1.

These coupons were ground to 1200 grit from 240 using silicon carbide paper, and cleaned using domestic detergent and water, and then using >99 % laboratory acetone in a Kemesonic Plus ultrasonic cleaner, for 10 minutes, and then dried using a hair dryer. This cleaning methodology was used throughout the study.

Table 3.1: The composition of the titanium alloy compositions used in this study.

Alloy Name	Constituent Element/wt%			
	Ti	Al	V	Nb
Ti64	90	6	4	0
Ti67	87	6	0	7

Table 3.2: Machine parameters for PVD coating of each treatment.

Coating	Coating Conditions						
	Frequency /kHz	Pulse Width/ns	Voltage	Start Current	End Current	Ramp /s	Total Time/s
Ag	50	1500	40	0.3	1.0	30	240
Pd	50	1500	40	0.3	1.0	30	240
Ag/Pd	50	1500	40	0.3	1.0	30	240

3.2 Surface Treatment

3.2.1 Pre-coating via Sputter Coating

Gold sputtering was done using an EMITECH K550 vacuum depositor. The chamber was evacuated to 0.05 torr, then purged and filled with argon gas to 0.1 torr, after which the Au was deposited using glow discharge at 25 mA for 6 minutes, and cleaned again.

3.2.2 Pre-coating via Physical Vapour Deposition (PVD)

Physical vapour deposition (PVD) was carried out using a Teer Coatings closed-field unbalanced magnetron sputtering instrument, which is capable of sputtering up to 4 target materials simultaneously. The layout of this instrument can be seen in figure 3.1, and the workings in figure 2.10. Silver, palladium, and a mixture of silver and palladium were sputtered using this method. The parameters for these coatings can be seen in table 3.2.

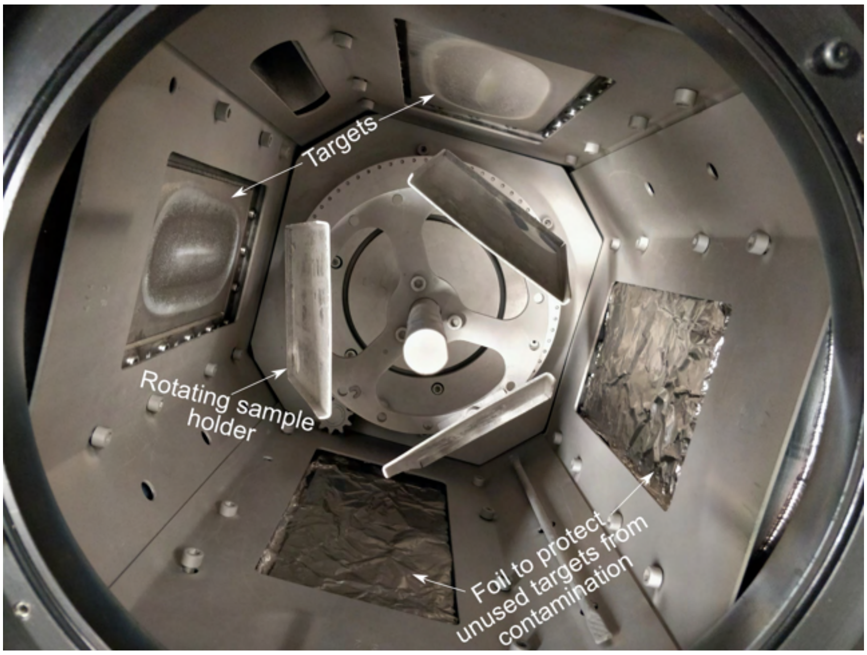

Figure 3.1: Internal layout of the PVD chamber, where samples are rotated within the chamber to allow an even coating from the target materials.

3.2.3 Ceramic Conversion Treatment (CCT)

CCT treatments were carried out on the test samples under atmospheric conditions in a laboratory furnace (Elite Thermal Systems Limited). Four TO treatment temperatures were selected based on a patented treatment [14], these were 580 °C, 620 °C, 660 °C, and 700 °C. For the treatments of duration longer than 20 h, samples were placed in the furnace and heated at a rate of 8 °C/min, and then left in the furnace in order to cool back to room temperature. For treatments of duration less than 20 h the furnace was first heated to treatment temperature and then the samples were placed into the furnace. Following completion of the heat treatment cycle, the samples were removed from the furnace and cooled at room temperature.

The treatments are summarised in tables 3.3 and 3.4.

Untreated (unt) samples were used as controls for both alloys.

Table 3.3: Treatment criteria of each treatment for Ti64.

Sample Name	Treatment Conditions		
	Temperature/C	Time/hours	Pre-deposition
Ti64 580	580	80	No
Ti64+Au 580	580	80	Yes - Au
Ti64+Ag/Pd 580	580	80	Yes - Ag/Pd
Ti64 620	620	80	No
Ti64+Au 620	620	80	Yes - Au
Ti64+Ag/Pd 620	620	80	Yes - Ag/Pd
Ti64 660	660	5, 80	No
Ti64+Au 660	660	80	Yes - Au
Ti64+Ag 660	660	5, 80	Yes - Ag
Ti64+Pd 660	660	5, 80	Yes - Pd
Ti64+Ag/Pd 660	660	1, 5, 10, 20, 40, 60, 80	Yes - Ag/Pd
Ti64 700	700	80	No
Ti64+Au 700	700	80	Yes - Au

Table 3.4: Treatment criteria of each treatment for Ti67.

Sample Name	Treatment Conditions		
	Temperature/C	Time/hours	Pre-depostion
Ti67 620	620	80	No
Ti67+Au 620	620	80	Yes - Au
Ti67 660	660	80	No
Ti67+Au 660	660	80	Yes - Au
Ti67+Ag/Pd 660	660	80	Yes - Ag/Pd
Ti67 700	700	80	No
Ti67+Au 700	700	80	Yes - Au

3.3 Characterisation

3.3.1 Roughness

Surface profiles of untreated and treated samples were measuring using a surface profilometer (Ambios XP-2). A diamond tipped stylus was dragged along the surface with a sliding distance of 5 mm and stylus force of 10 mg. This was repeated a minimum of 5 times for each sample and arithmetical average roughness (R_a) of these profiles were calculated within the software and used as the roughness parameter.

3.3.2 Scanning Electron Microscopy (SEM) and Energy Dispersive X-ray Spectroscopy (EDX)

Surface morphology was observed using SEMs (Oxford JEOL6060 and JEOL7000) with 20 kV accelerating voltage and 10 mm working distance for both microscopes. Energy dispersive X-ray spectroscopy (EDX) was also carried out using the same respective SEM to show the elemental compositional data on the sample's surface.

The samples were also cut and mounted in Bakelite. Subsequent grinding from P240-P1200 with SiC paper, diamond suspension polishing at 6 and 3 μm, and final polishing with activated-colloidal silica suspension allowed cross-section morphology to be observed using the same SEM (JEOL7000). Etching with Kroll's reagent revealed the metallographic micro-structure of these cross-sections. EDX surface mapping was also carried out to show the elemental distribution throughout the sample's cross-section, using this SEM equipped with a Oxford Instruments Inca 300 detector. Part way through this study the detector was upgraded to an Oxford Instruments Ultim Max 40 (SDD).

The cross-sectional images obtained were then analysed using ImageJ to measure the layer thickness.

3.3.3 Glow Discharge Optical Emission Spectroscopy (GDOES)

Layer-by-layer compositional data was collected using a GDOES instrument (GDA-650HR Spectruma Analytik). Due to the non-conducting TiO_2 surface oxide, RF pulsed mode was used, with a working gas of Argon, at 335 Pa pressure. Analysis was carried out for all elements within the alloy, at a diameter of 2.5 mm. The measured emission spectra were recorded and measured against a built-in database within the computer software to calibrate them.

3.3.4 X-ray Diffraction Analysis (XRD)

The phase composition was analysed using an X-ray diffraction instrument (XRD, Bruker D8 Advanced or Proto AXRD), with a Cu source ($K\alpha$ = 0.145 nm). The 2Θ angles ranged from 20-80°, at 40 kV voltage and 40 mA current.

The results of this were analysed using X'pert High Score Plus software, with COD and PDF-2 databases.

3.3.5 Transmission Electron Microscopy (TEM)

Detailed surface layer micro-structure and phase composition were analysed for the C3T Ag/Pd 660 20 h sample by transmission electron microscopy (TEM). The TEM specimens were prepared perpendicularly to the surface (XTEM) by using focused ion beam milling (FIB, FEI Quanta 3D) following the standard steps of Pt deposition, bulk out, u-cut, lift out, mounting, thinning and cleaning. The micro-structure was examined under a Jeol 2100 electron microscope (LaB6, 200 kV). High angle annular dark field (HAADF) imaging and Energy-dispersive X-ray spectroscopy (EDX, Oxford) analysis was performed using scanning TEM (STEM) mode with a Philips Tecnai F20 instrument (FEG, 200 kV).

3.4 Mechanical and Tribological Property Testing

3.4.1 Micro-hardness

Surface micro-hardness was measured for each sample using either a Mitutoyo MVK-HR or a Zwick Roell ZHVμ, the latter being fitted with an eo Edmund camera and uEye cockpit software. Both machines were equipped Vickers diamond intenders. A load of either 25 or 50 g for 10 s was used. Before measurements were taken, calibration was done using a calibration block with hardness 753.3HMV0.3. Each measurement was repeated a minimum of 5 times.

Cross sectional micro-hardness was measured using the same machines and used to determine the thickness of the oxygen diffusion zone (ODZ). Micro-hardness was measured at increasing depth from as close to the oxide as possible, until the obtained values plateaued. A load of 25 g for 10s was used for this.

Table 3.5: Calculated maximum hertzian contact pressures for untreated and treated samples.

Sample Type	Approximate Maximum Contact Pressure/MPa	
	15N	50N
Untreated	1200	2000
Treated	1600	2700

3.4.2 Tribological Behaviour

The wear and friction properties of the samples were investigated. Ball-on-disc reciprocating tribotests were carried out using a Phoenix TE79 tribometer with an 8mm tungsten carbide (WC) counterpart. The cycle distance was 5mm for 1000 cycles, resulting in a total sliding distance of 5 m. Loads of 15 or 50 N were utilised. This resulted in a range of approximate maximum hertzian contact pressures, which can be seen in table 3.5.

The wear tracks yielded from this were then investigated using a surface profilometer (Ambios XP-2) to obtain their average cross-sectional area. These were then used to calculate both the wear volume (equation 3.1) and wear factor (equation 3.2).

$$Wear\ Volume\ (mm^3) = Wear\ Track\ Cross\ Sectional\ Area\ \cdot\ Ball\ Sliding\ Distance\ (mm) \tag{3.1}$$

$$Wear\ Factor\ (\frac{m^3}{N \cdot m}) = \frac{Wear\ Volume\ (m^3)}{Normal\ Load\ (N) \cdot Ball\ Sliding\ Distance\ (m)} \tag{3.2}$$

After this, the wear tracks were imaged with an SEM (Oxford JEOL7000/JEOL6060), using 20 kV accelerating voltage and a 10 mm working distance, and EDX analysis carried out using the same SEMs to study the wear modes and potential mechanisms involved.

3.5 Simulated Bone Fixation Pin Drilling

A comparison of biomechanical properties of untreated, C2T, and C3T Ag/Pd fixation pins were evaluated by insertion tests using a cortical bone simulating material from SAWBONES® (Europe AB, Sweden). A schematic of the procedure can be seen in figure 3.2. Initial testing was conducted on untreated and C3T Ag/Pd 660 5h treated Ti-6Al-4V pins. The bone blocks (30 x 17 x 10 mm) were used to simulate pin insertion. An industrial drilling machine (Mazak Vertical Center Smart 430A) was employed to conduct the insertion test under a constant feed rate (i.e., insertion speed) of 70 mm/min and rotation speed of 360 rpm. The driller was connected to a Kistler Piezoelectric Dynamometers (Type 9273) for the measurement of axial insertion force. The pin was inserted a distance of 25 mm without pre-drilling through the plate. The applied axial force needed to achieve this fixed insertion speed was continuously recorded by the Kistler Piezoelectric Dynamometers. The insertion performance was evaluated by determining the maximum and average axial insertion force.

Post-insertion observation was conducted to reveal the wear on the cutting surfaces of the untreated and treated pins using Toolmakers optical microscopy and SEM analysis at the cross-section of the pin. After this the treatment duration was optimised to 3h.

Untreated, PVD of Ag/Pd only, C2T 660 3h, C2T 620 80h, and C3T Ag/Pd 660 3h were selected for further analysis. This was carried out using the same parameters,

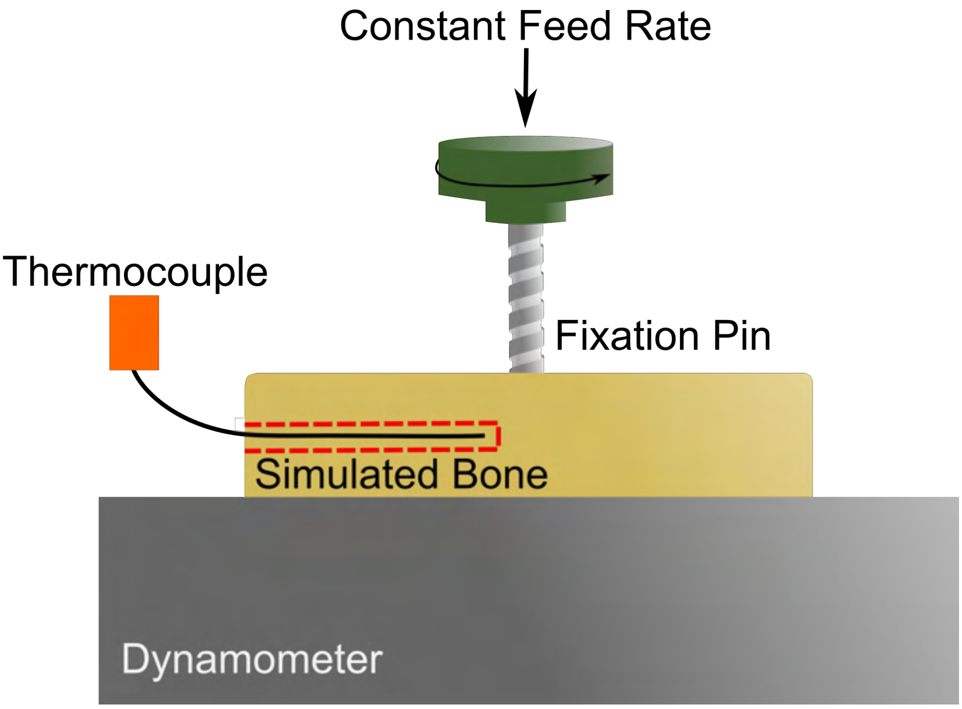

Figure 3.2: Schematic of the fixation pin drilling procedure.

but thermal analysis was also carried out by placing a thermal couple into a drilled hole adjacent to where the drilling would be carried out. In addition to this, post-drilling temperature was monitored on the pin tip. Additionally, post-insertion observation was conducted to reveal the wear on the cutting surfaces of the untreated and treated pins using Toolmakers optical microscopy and SEM analysis.

3.6 Anti-microbial Testing

3.6.1 Coupons

Antibacterial testing was carried out on the coupon samples using a methodology based on the Miles and Misra method [192]. Single colonies of gram-positive *Staphylococcus aureus* (*S. aureus*) NCTC 6571 were serially diluted in tryptone soya broth (TSB) (Oxoid) down to 10^4 from 10^9 cells/ml. Each autoclaved sample ($n = 3$ per sample group) was inoculated with 20 μl of this solution in a petri dish and incubated at 37 °C for 6 h before dilution in 10 ml of phosphate buffered saline (PBS) and vortexing to dislodge the surface adhered bacteria. Serial dilutions to reduce the concentration by 10^{-7} were then made in a 96 well plate (as shown in figure 3.3) by first pipetting 200 μl of the original solution into well A. Wells B-H contain 180 μl of PBS. After this, 20 μl of A was transferred into well B and mixed well (pipetted up and down multiple times). 20 μl from well B is then pipetted into well C, and this continues until well H. Each dilution in the 96 well plate (A-H) was pipetted into a quadrant on a trypton soya agar (TSA) plate of their respective dilution factor. These were then incubated at 37 °C overnight, after which each quadrant was observed for growth and colonies counted. The number of colony-forming units (CFU) per ml from the original aliquot was calculated from this.

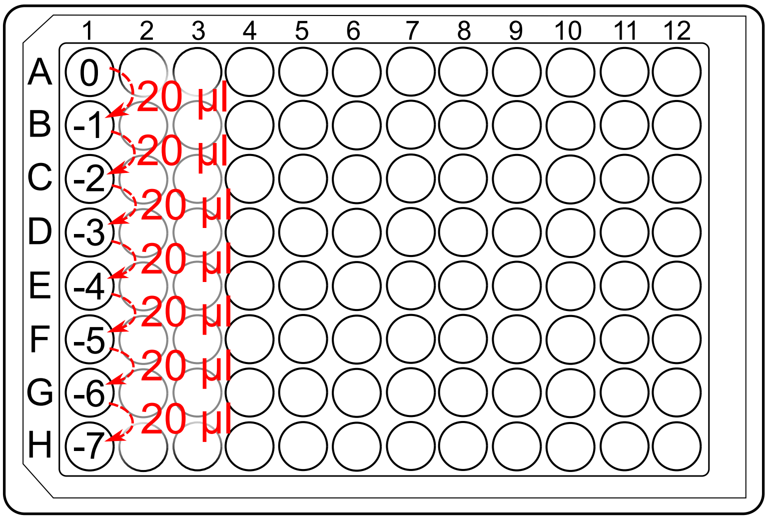

Figure 3.3: Schematic of the serial dilutions carried out in a 96-well plate. Well A contains 200 μl of the original solution, and wells B-H contain 180 μl of PBS.

3.6.2 Fixation Pins

Antibacterial testing of the same NCTC 6571 *S. aureus* strain was carried out on the post-drilled autoclaved fixation pins of untreated, C2T 660 3 h, C2T 620 80 h, and C3T Ag/Pd 660 3 h (n = 3 for each sample type), using a methodology based on that from Furkert *et al.* [193]. The pins were cut to 15 mm in length from the cutting tip and the initial stages of creating the bacterial suspension and diluting it is the same as for the coupon samples. Following the bacterial suspension creation, the pins were immersed in 1.5 ml of bacterial suspension in individual microfuge tubes and incubated at 37 °C for 6 h.

After the incubation period, the suspension was discarded, and the pins were vortexed in 1 ml of PBS. After this, the methodology was as for the coupon samples, where serial dilutions were carried out in a 96 well plate and plated into quadrants of the respective dilutions. Incubation was carried out overnight at 37 °C, and the plates were observed for growth. The colonies counted provided the number of colony-forming units (CFU) per ml from the original aliquot.

3.7 Statistical Analysis

Unless specified, the mean values and standard deviations (SD) of all numerical data were calculated and reported. Within each test parameter, the data sets were analysed using SigmaPlot (version 14.5), with a significance value of $p = .05$. Normality was tested for, and analysis of variance (ANOVA) run at a significance level of $p < .05$. Post-hoc Tukey's tests were also run on data deemed significantly ($p < .05$) different.

Chapter 4

Experimental Results

4.1 Pre-coating Physical Vapour Deposition (PVD)

In order to determine the particle size and coating thickness a silicon wafer was used as a flat and smooth substrate. The sputtered particles of Ag and Pd from the PVD process onto this silicon wafer are shown in figure 4.1. The average particle size is measured as 57 ± 18 nm.

A layer of foil was applied to the silicon wafer prior to this PVD coating and removed post-coating to allow the measurement of the surface profile. The profile can be seen in figure 4.2, and the subsequent average coating thickness is measured to be approximately 330 nm.

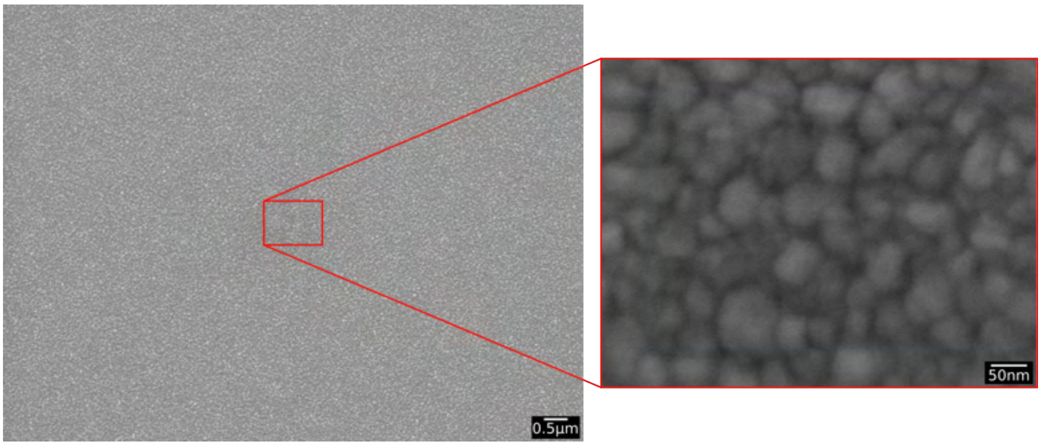

Figure 4.1: Surface images of an untreated silicon wafer with Ag/Pd particles post-PVD. Inset image presents a higher magnification of the same region.

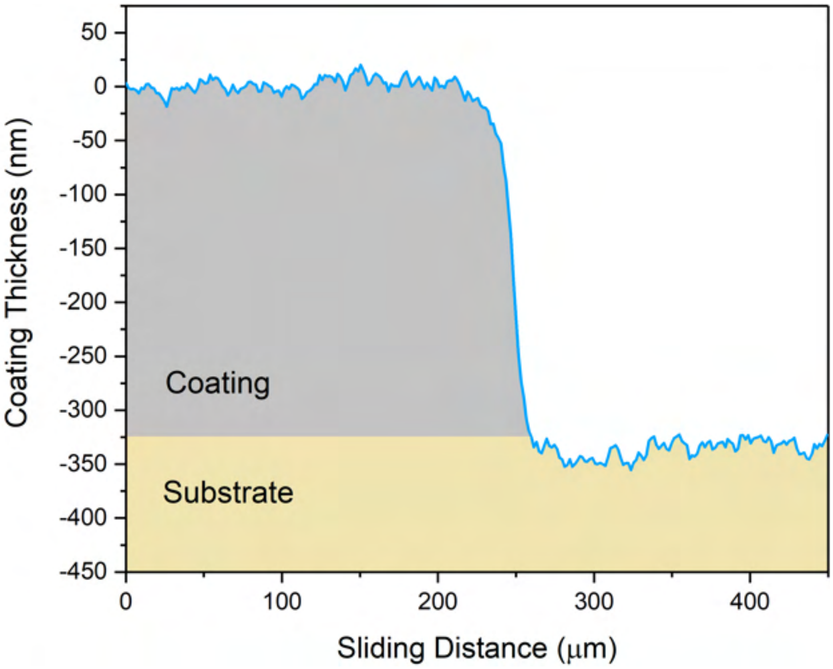

Figure 4.2: Surface profile of an untreated silicon wafer with Ag/Pd particles post-PVD.

4.2 Ceramic Conversion Treatment (CCT)

4.2.1 Surface Morphology and Cross-Section Layer Structure

Cross-sectional SEM images of untreated Ti64 and Ti67 can be seen in figure 4.3. It can be seen that for both Ti64 (a) and Ti67 (b) no visible surface layer is present. A refined grain structure can be seen for both alloys, with a primary α phase structure surrounded by β grains, examples of which have been labelled.

The surface morphology images of Ti64 untreated, C2T, and C3T Au samples treated at 620, 660, and 700 °C for 80 h are shown in figure 4.4. Untreated displayed grinding grooves (a) at the surface from the sample preparation procedure.

C2T produced an agglomerated surface structure, as labelled, suggesting the growth of a layer onto the surface. Increasing the treatment temperature (b to d and d to f)

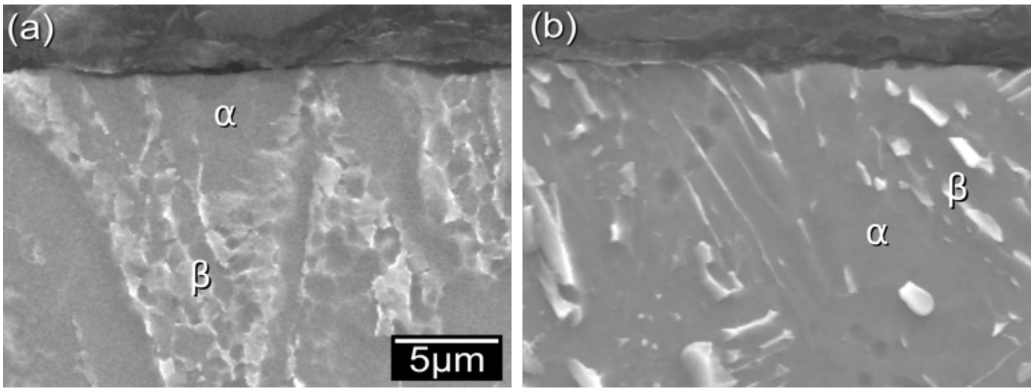

Figure 4.3: Cross-sectional micro-morphology SEM images of untreated Ti64 (a) and Ti67 (b). Examples of regions with different grain structure have been labelled. Magnification is the same for both images.

increased the size of these agglomerates.

C3T Au samples (c, e, and g) showed a similar appearance to C2T, but also with the presence of small particles spread over the surface, an example of which is labelled in (c). The size of the agglomerates although increased with increasing treatment temperature, did not grow as large as for the respective temperatures of C2T. Additionally, the size of the surface particles decreased with increasing treatment temperature, potentially due to being dispersed throughout a thickening layer. Both C3T Au 660 (e) and 700 (g) displayed the presence of surface blisters, as labelled, which is likely caused by the layer growth being unstable.

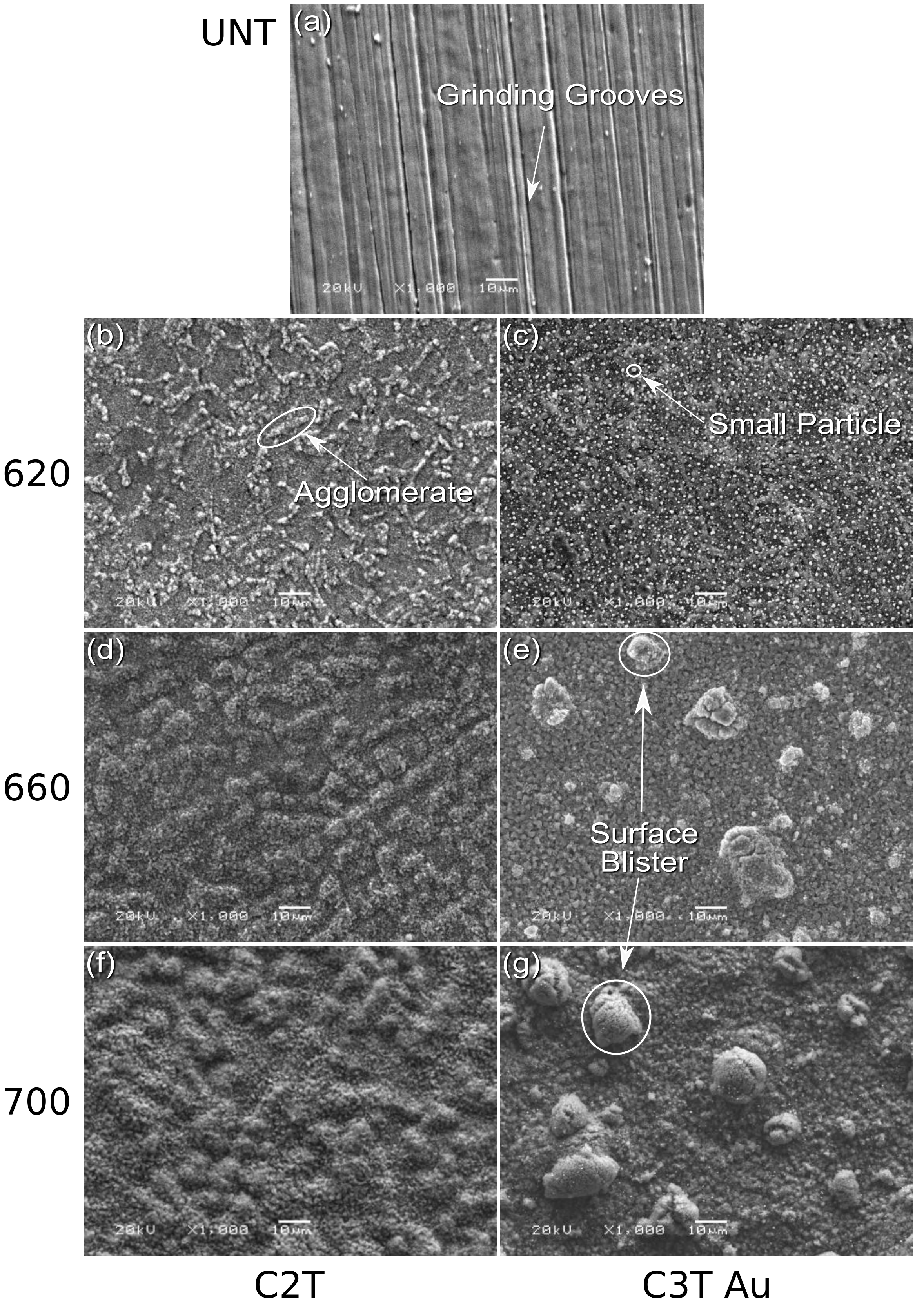

Figure 4.4: Surface micro-morphology secondary electron SEM images of Ti64. Where: (a) untreated, (b) 620, (c) 620 + Au, (d) 660, (e) 660 + Au, (f) 700, (g) 700 + Au.

The surface morphology images of Ti67 untreated, C2T, and C3T Au samples treated at 620, 660, and 700 °C for 80 h are shown in figure 4.5.

Both untreated (a) and C2Ted Ti67 still demonstrated grinding grooves for all non-pre-deposited samples but increasing treatment temperature reduced their depth. Au pre-deposition masked the presence of these grinding grooves and increasing from 620 to 660 reduced the Au particle size also. However, increasing further to 700 (figure 4.5(g)) resulted in clustering of the Au particles.

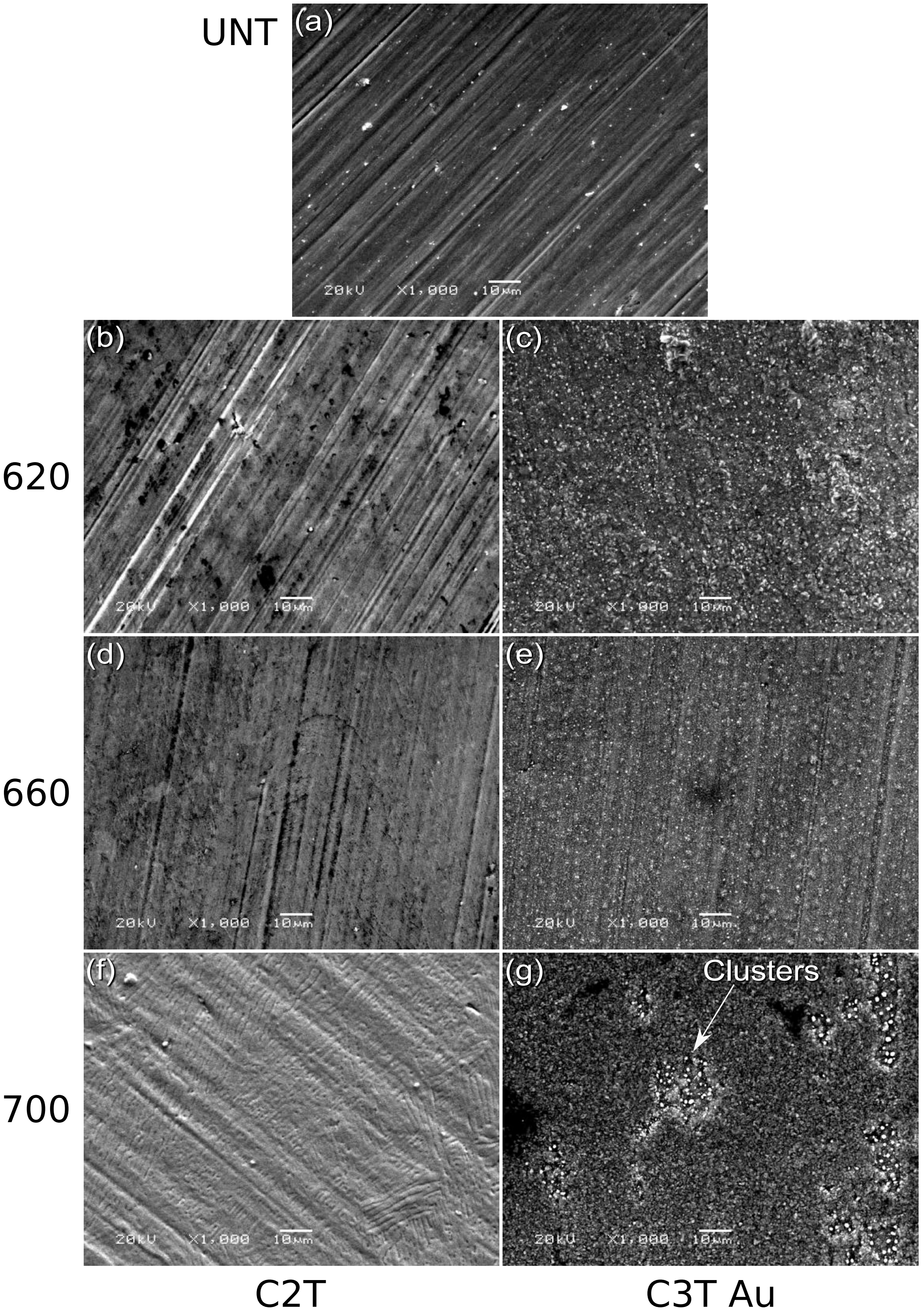

Figure 4.5: Surface micro-morphology secondary electron SEM images of Ti67. Where: (a) untreated, (b) 620, (c) 620 + Au, (d) 660, (e) 660 + Au, (f) 700, (g) 700 + Au.

Cross-sectional SEM images for Ti64 C2T and C3T Au treated at 580, 620, 660, and 700 °C for 80 h can be seen in figure 4.6.

After treatment, regardless of condition, a surface layer formed. This layer typically increased in thickness with increasing treatment temperature, with C3T Au 700 (h) being the exception to this. However, it can be seen that although the oxides are thicker, their quality does not follow the same trend. For C2T it can be seen that with increasing treatment temperature the substrate-layer interfacial bonding decreases, where large cracks are present, as labelled in c, e, and g. The same is true for C3T Au, and in addition to this, both 660 (f) and 700 (h) present blisters in the layer, as labelled. These suggest an unstable growth occurred. C3T Au 580 (b) and 620 (d) produced a dense and well bound surface layer, which was significantly thicker for C3T Au 580, and slightly thicker for C3T Au 620 than that of the same C2T condition (580 (a) and 620 (c)). This suggests that the catalytic layer had a greater influence at the lower temperature of 580.

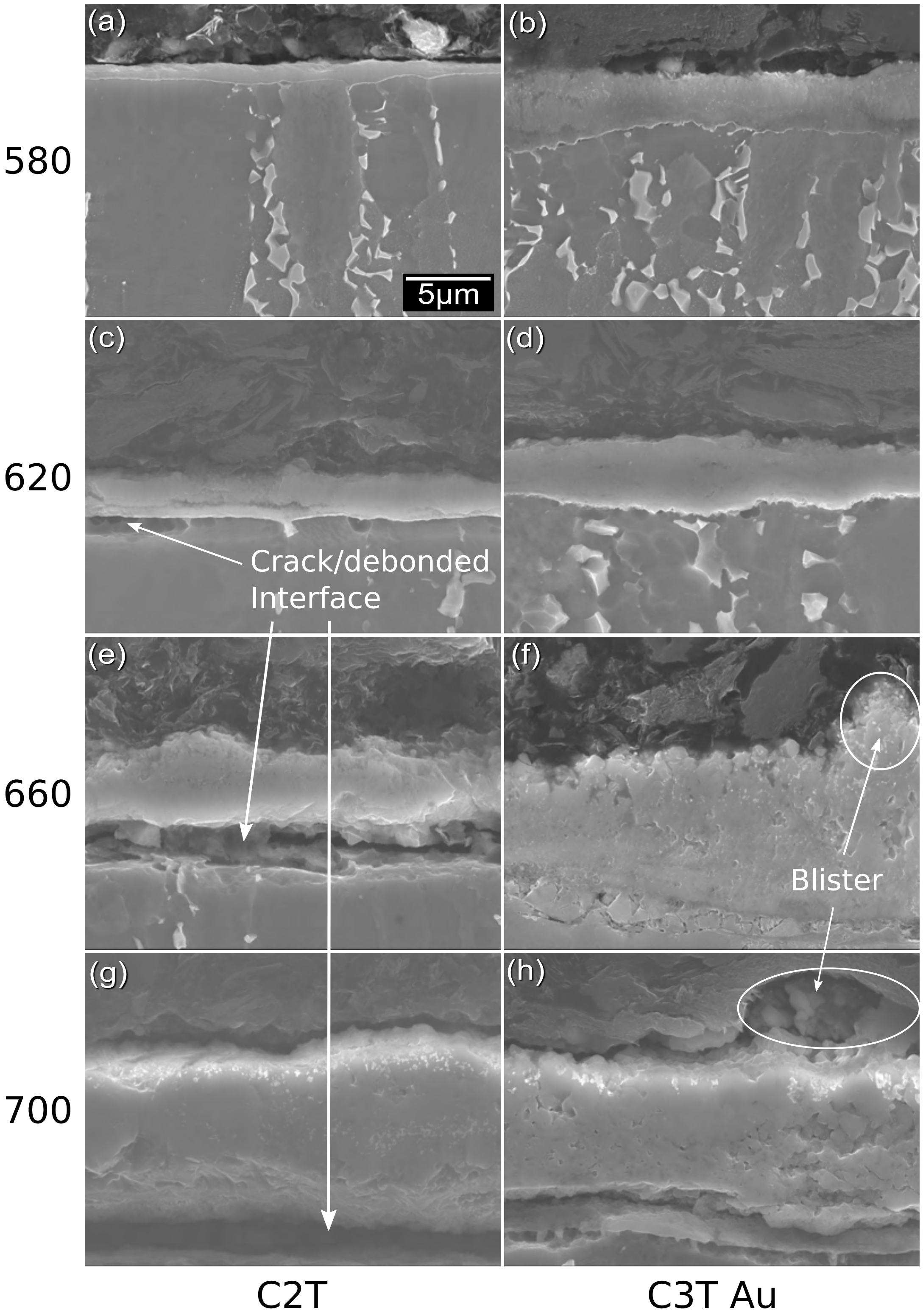

Figure 4.6: Cross-section micro-morphology secondary electron SEM images of Ti64 C2T and C3T Au. Where: (a) 580, (b) 580 + Au, (c) 620, (d) 620 + Au, (e) 660, (f) 660 + Au, (g) 700, and (h) 700 + Au. Magnification is the same for all images.

Cross-sectional SEM images for Ti67 untreated, C2T, and C3T Au treated at 620, 660, and 700 °C for 80 h can be seen in figure 4.7.

It can be seen that after treatment a surface layer is present on all treated samples (a-f). For both C2T (a, c, and e) and C3T Au (b, d, and f), increasing treatment temperature resulted in an increase in layer thickness. In addition to this, the presence of gold meant that for the same treatment condition, C3T Au was also thicker than for C2T (a vs b, c vs d, and e vs f).

When comparing C2T to C3T Au, it can be seen that C2T presented a substrate/layer interface with great adhesion strength due to it forming a structure which increases mechanical bonding, as labelled in (c), whereas C3T Au presented some lighter regions beneath the substrate/layer interface, suggesting the presence of β grains here, as labelled in (f).

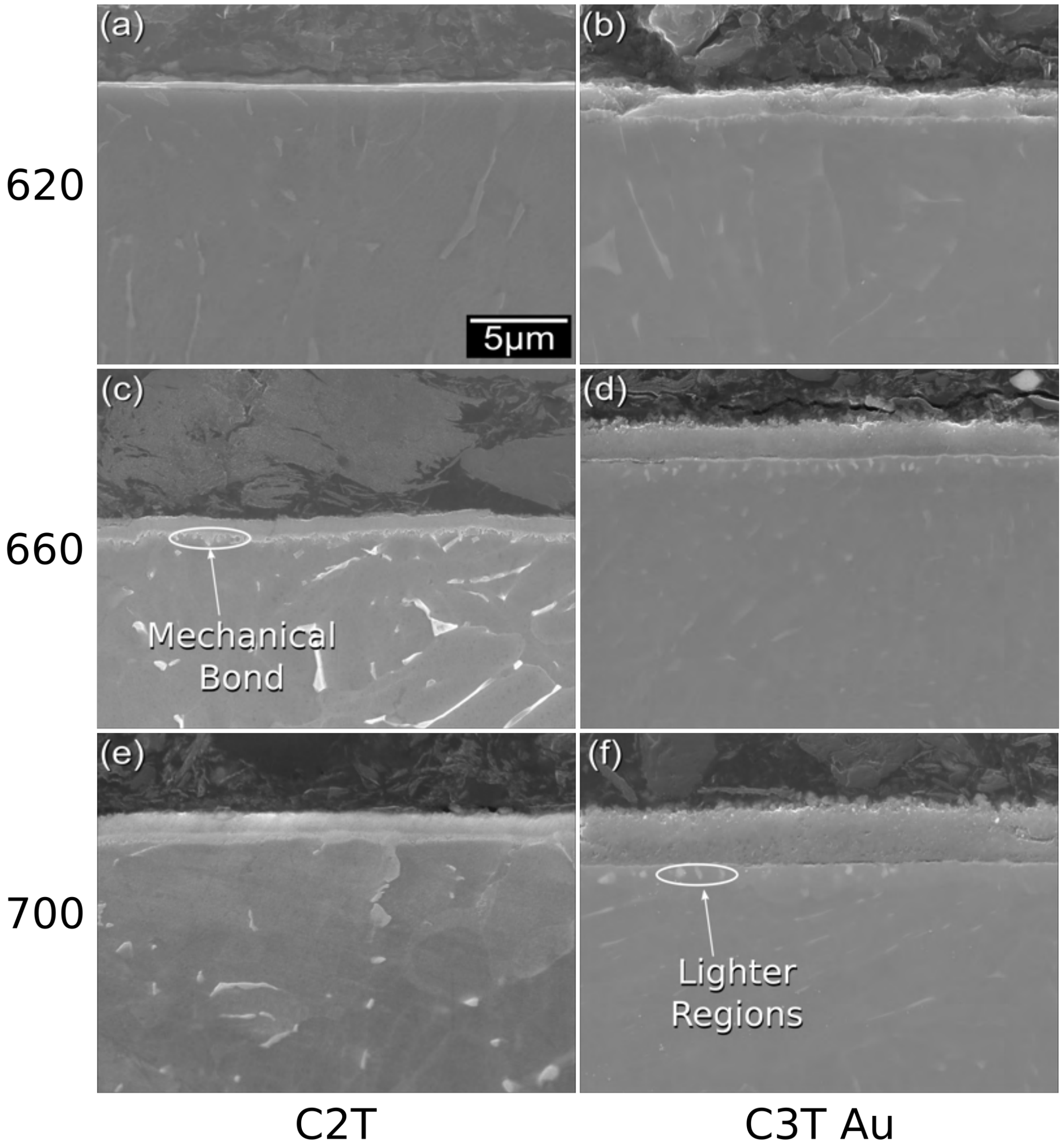

Figure 4.7: Cross-section micro-morphology secondary electron SEM images of Ti67. Where: (a) 620, (b) 620 + Au, (c) 660, (d) 660 + Au, (e) 700, (f) 700 + Au. Magnification is the same for all images.

Surface morphological images of Ti64 C3T Ag/Pd 660 1-80 h are shown in figure 4.8. It can be seen that initially an agglomerated surface structure can be seen (a), which when increasing treatment duration to 5 h (b), begins to disperse and a needle-like structure begins to form in the gaps between (an example is labelled). A further increase in treatment duration to 10 h (c) results in the agglomerated structures coalescing into larger agglomerates (labelled), suggesting their migration to each other, and the needle-like structures becoming well-defined around these agglomerates. After 20 h (d), the needle-like structures begin to smooth/become less defined, which suggests that an additional layer is potentially growing over them. The agglomerates begin to change in shape to have sharper edges after 40 h (e), which continues to further sharpen after 60 h (f). In addition to this, the appearance of spherical shapes occurs in the agglomerates vicinity (labelled), suggesting the growth of a new phase. After 80 h (g), the needle-like structures are replaced by these spherical shapes and the agglomerates remain with sharp edges.

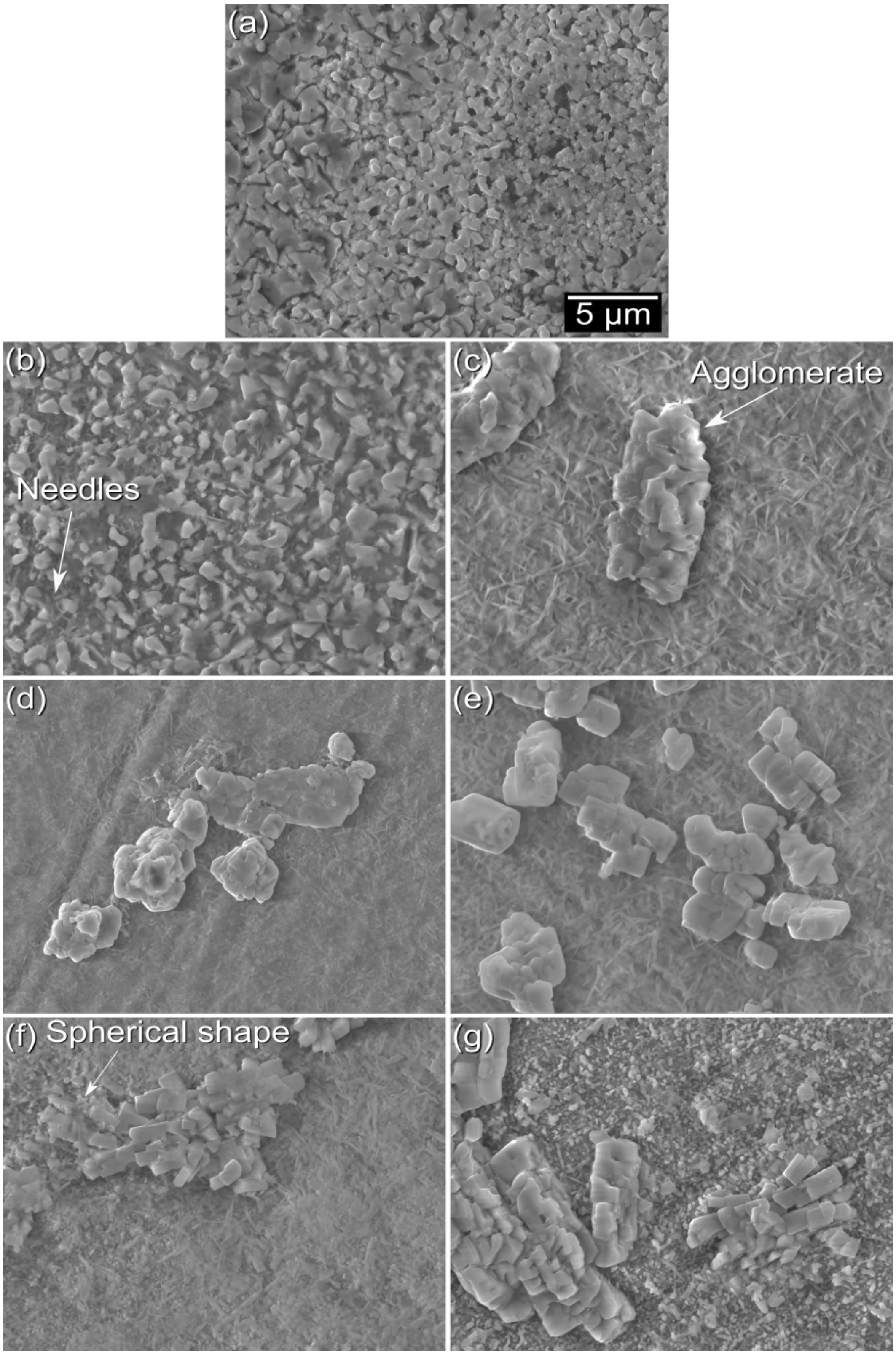

Figure 4.8: Surface micro-morphology secondary electron SEM images of Ti64 C3T Ag/Pd 660. Where: (a) 1h, (b) 5h, (c) 10h, (d) 20h, (e) 40h, (f) 60h, (g) 80h. Magnification is the same for all images.

Surface roughness of Ti64 C3T Ag/Pd treated at 660 °C for varying treatment durations ranging from 1 to 80 h can be seen in figure 4.9. Results statistically non-significant ($p > .05$) are denoted by * and/or ** in the figure.

It can be seen that increasing treatment duration resulted in an increase in surface roughness until 60 h, after which a decline occurred. However, this is only a significant ($p < .05$) increase when increasing in the earlier durations (between 1 and 20 h) and between 60 and 80 h. 20, 40, and 80 h treatments did not show a significant difference ($p > .05$), and neither did 40 and 60 ($p < .05$). This signifies that although the general trend does show an increasing roughness with increasing treatment duration, it was not a very significant change for treatments beyond 20 h. This denotes that not as significant of a surface structure change occurred compared within the previous treatment stages.

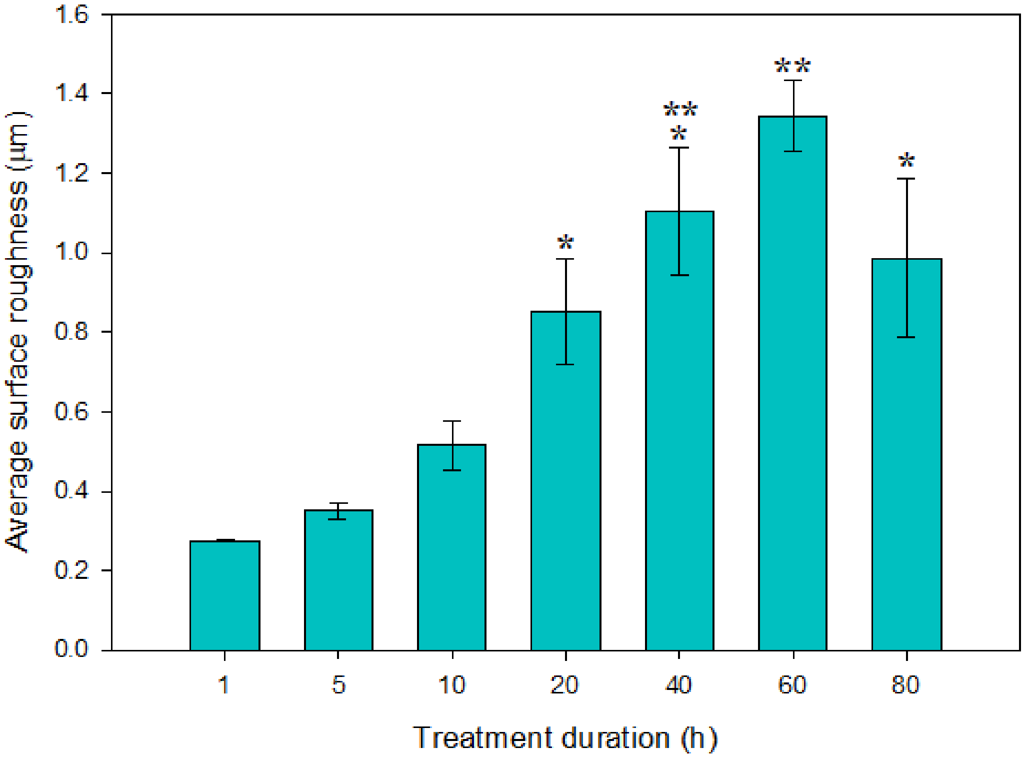

Figure 4.9: Surface roughness of Ti64 C3T Ag/Pd 660 1-80 h. * and ** denote $p > .05$.

Cross-sectional SEM images for Ti64 C3T Au and C3T Ag/Pd treated at 580, 620, and 660 °C for 80 h can be seen in figure 4.10. The 700 °C treatment has been left out due to C3T Ag/Pd experiencing severe spallation, meaning that imaging was not possible. Note, the C3T Au images are of the same samples from figure 4.6, but with lower magnification, to match that of the C3T Ag/Pd in this figure.

It can be seen that after treatment, as expected, all samples have got a surface layer present. Additionally, increasing treatment temperature resulted in a significant increase in layer thickness; especially for C3T Ag/Pd when increasing from 620 (d) to 660 (f). However, although the substrate/layer interface demonstrates good bonding and quality, it can be seen that for C3T Ag/Pd 620 (d) and 660 (f) the layer contains pores.

When comparing C3T Au and C3T Ag/Pd for the sample treatment temperature (a vs b, c vs d, and e vs f) it can be seen that, although C3T Au has an improved thickness compared with C2T, C3T Ag/Pd has a much greater catalytic effect than Au.

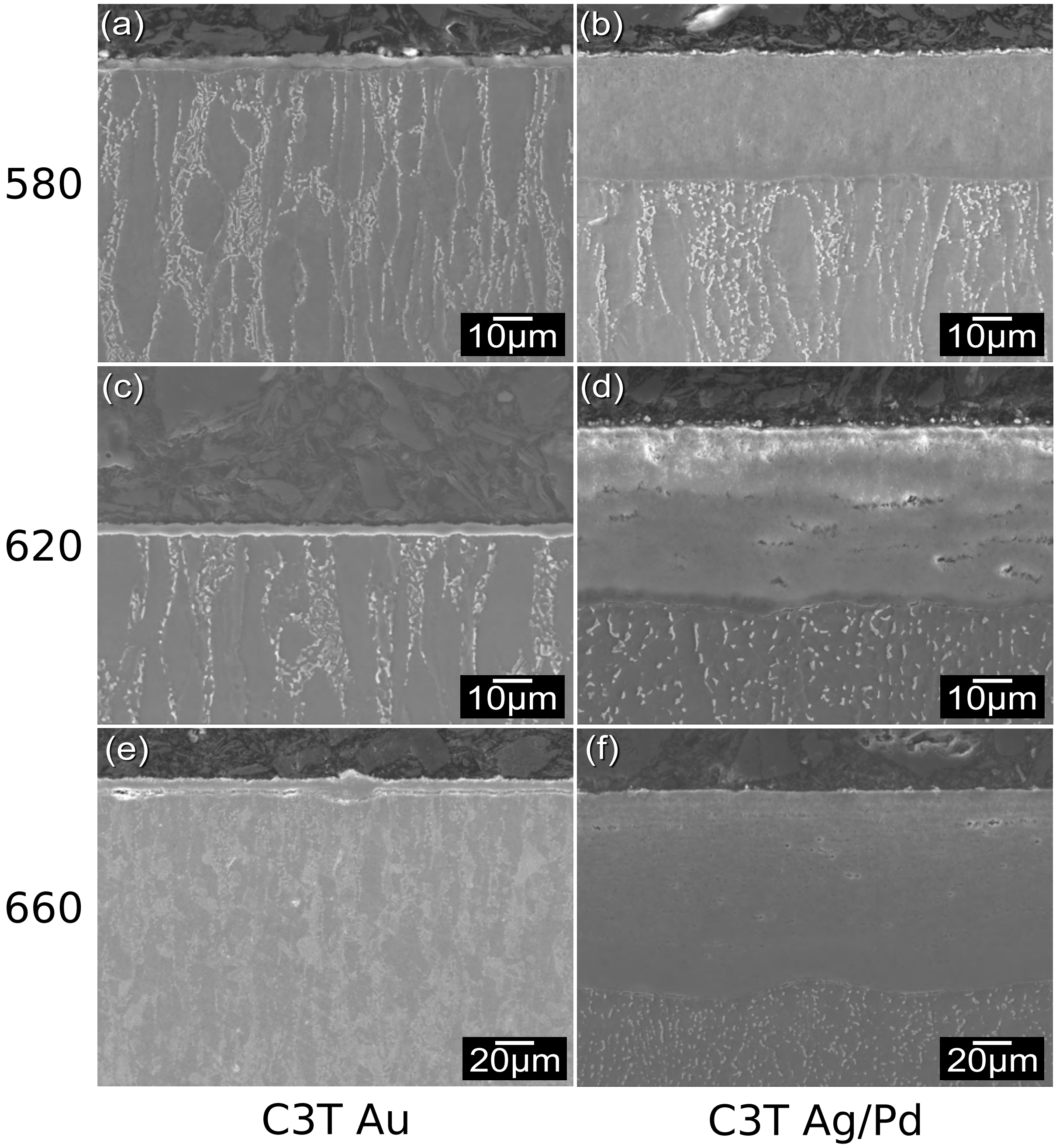

Figure 4.10: Cross-section micro-morphology secondary electron SEM images of Ti64 C3T Au and C3T Ag/Pd. Where: (a) 580 + Au, (b) 580 + Ag/Pd, (c) 620 + Au, (d) 620 Ag/Pd, (e) 660 + Au, and (f) 660 + Ag/Pd. Please note the scale bar change for 700 (e and f) due to different magnifications being required to image the layers.

Cross-section SEM images for Ti64 C3T Ag/Pd treated at 660 °C for treatment durations between 1 and 80 h can be seen in figure 4.11 and Ti67 C3T Ag/Pd treated for 80 h can be seen in figure 4.12. Please note the scale bar changes for Ti64 when increasing treatment duration due to the magnification change requirements with increasing layer thickness to enable the whole layer to be visible adequately.

It can be seen that all treatment conditions produced surface layers, and that these layers demonstrate good substrate-layer interfacial bonding. For Ti67 it can be seen that the treatment resulted in an oxide layer of poor quality with large de-bonding agglomerates. Because of this, further treatment conditions were not carried out for this alloy and catalytic layer combination.

For Ti64 it can be seen that increasing treatment duration resulted in an increase in layer thickness, and as shown in figure 4.11 (a), the C3T Ag/Pd 660 1 h treatment produced a surface layer with two distinct regions. These consist of a darker region with a lighter one above it at the surface/subsurface, suggesting the presence of two different phases within the layer. This lighter region reduces in size with increasing treatment duration (b-g).

Initially, the layers are dense (a-c), but after 20 h (d) pores begin to appear in the layer. These increase with increasing treatment duration beyond this (e-g), although there is slightly fewer for the 80 h treatment (g).

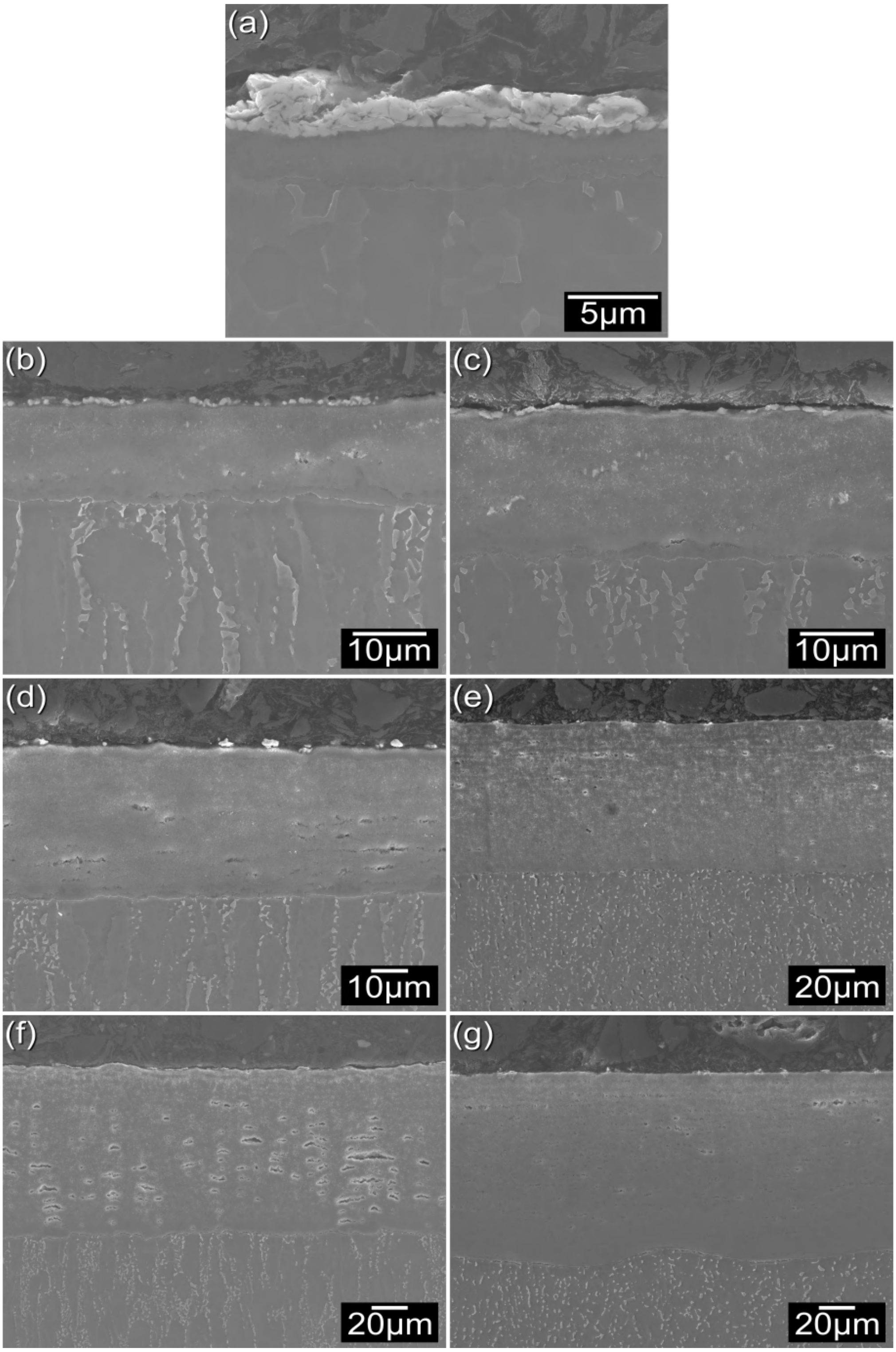

Figure 4.11: Cross-section micro-morphology secondary electron SEM images of Ti64 C3T Ag/Pd 660. Where: (a) 1h, (b) 5h, (c) 10h, (d) 20h, (e) 40h, (f) 60h, (g) 80h. Please note scale bar differences for (a), (b, c, d), and (e, f, g) due to requiring different magnifications.

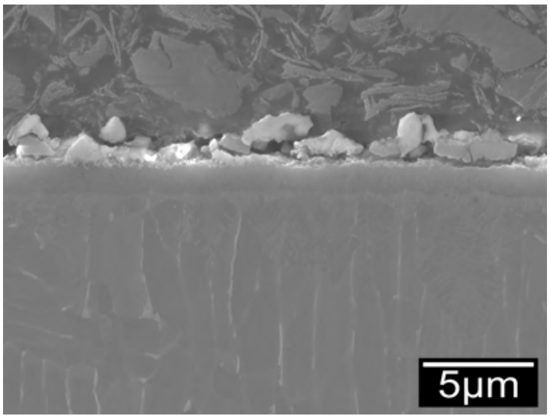

Figure 4.12: Cross-sectional micro-morphology SEM images of Ti67 C3T AgPd treated at 660 for 80 h.

Surface morphology SEM images for C2T and C3T Ag, Pd, Ag/Pd, 660 5 h samples can be seen in figure 4.13. It can be seen that for C2T (figure 4.13(a)), a fine agglomerated structure has been formed, with some larger agglomerates displayed in a similar structure to Ti64's grain structure.

The C3T surfaces can be seen in figures 4.13(b-d). C3T Ag (figure 4.13(b)) demonstrated a needle-like rose-petal appearance. Changing the Ag to Pd (figure 4.13(c)) resulted in a change to the structure of the agglomerates, where they became cauliflower-like. Combining the Ag and Pd (figure 4.13(d)) resulted in a mix of globular agglomerates with interspersed needle structures.

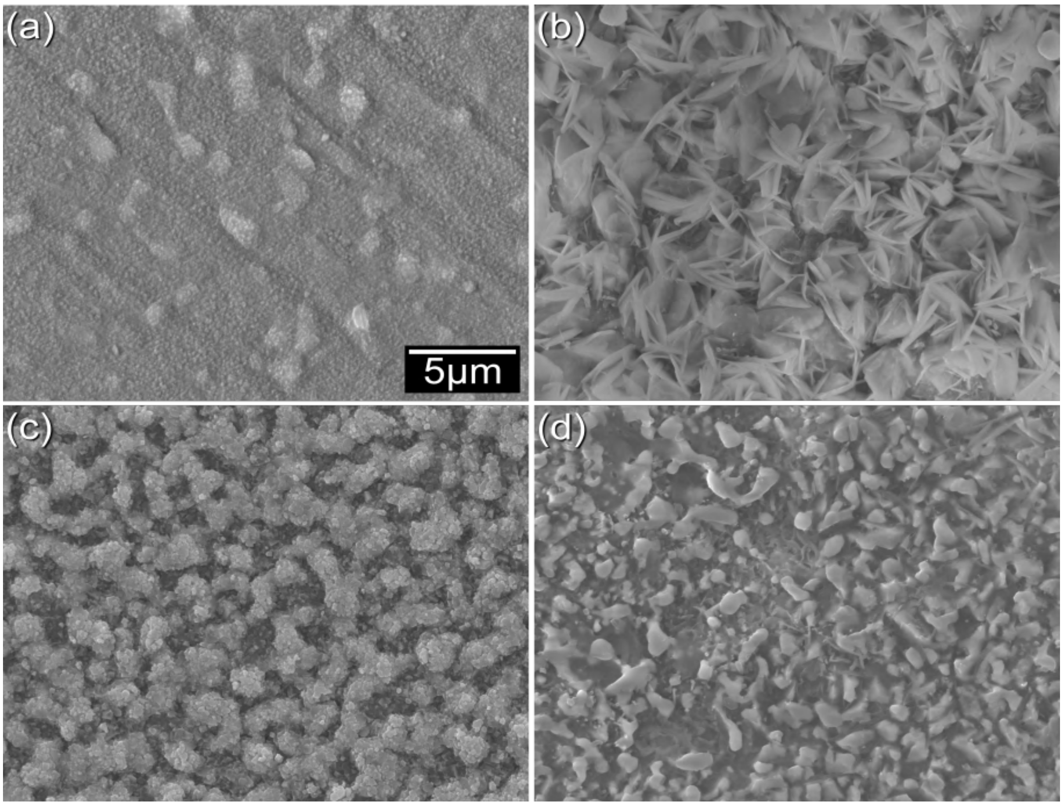

Figure 4.13: Surface micro-morphology secondary electron SEM images of Ti64 C2T and C3T with depositions of either Ag, Pd, or Ag/Pd. All treatments were at 660 C for 5 h. Where: (a) C2T, (b) C3T Ag, (c) C3T Pd, (d) C3T Ag/Pd. Magnification is the same for all images.

Figure 4.14 is a comparison for Ti64 between C2T (a, e) and C3T Ag (b, f), Pd (c, g), and Ag/Pd (d, h). All of the treatments are at 660 and for either 5 h (a-d) or 80 h (e-h). As shown in (a) and (e), C2T treatments regardless of treatment duration have a poor substrate/oxide interfacial bonding, although it is more severe for the longer duration.

In contrast, all of the C3T treatments (b-d and f-h) demonstrate good interfacial bonding. Regardless of treatment duration, C3T Ag (b and f) and C3T Ag/Pd (d and h) have similar thickness and appearances, with Ag/Pd being marginally thicker for the 5 h treatment duration (b vs d). However, although the interfacial bonding and layer density are good for C3T Pd (c and g), it can be seen that the layer thickness is much thinner than both Ag and Ag/Pd.

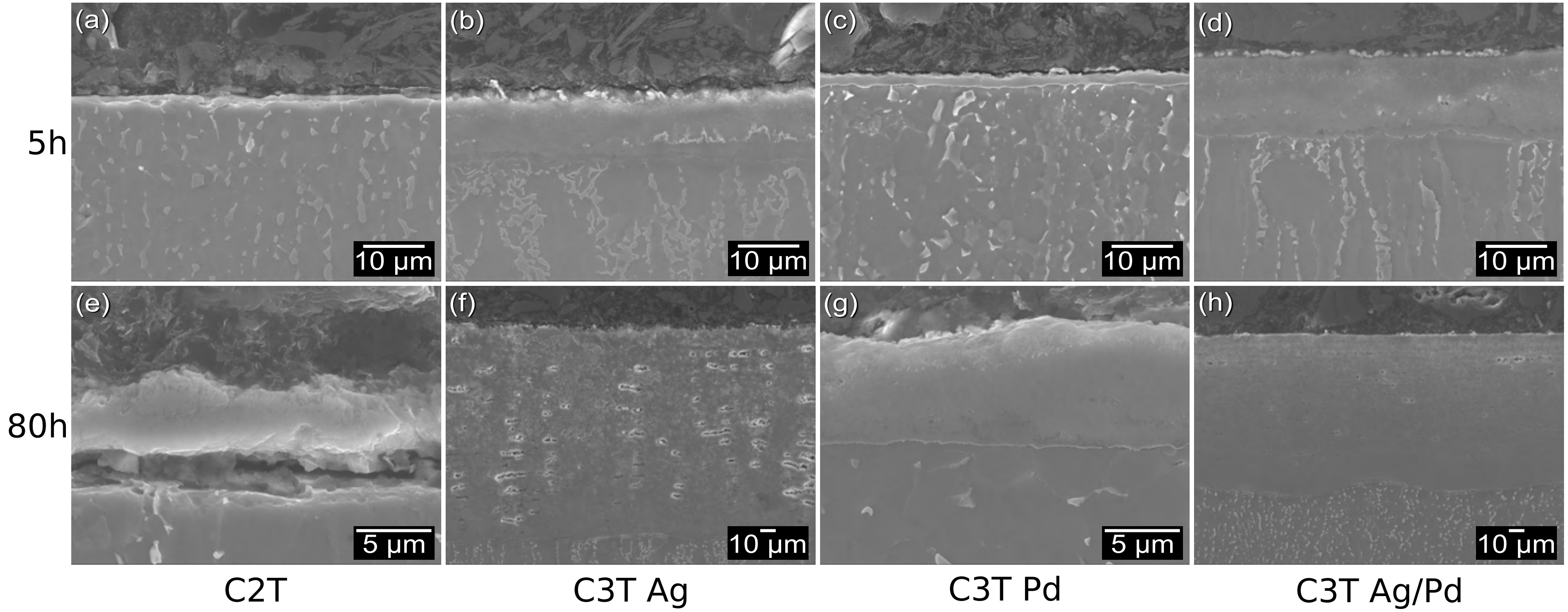

Figure 4.14: Cross-section micro-morphology secondary electron SEM images of Ti64 C2T and C3T 660 5 and 80 h. Where: (a) C2T 660 5 h, (b) C3T 660 5 h Ag, (c) C3T 660 5 h Pd, (d) C3T 660 5 h Ag/Pd, (e) C2T 660 80 h, (f) C3T 660 80 h Ag, (g) C3T 660 80 h Pd, (h) C3T 660 80 h Ag/Pd. N.b. please note the scale bar changes due to different magnifications being required.

4.2.2 Micro-structure and Composition

Cross-sectional energy dispersive X-ray spectroscopy (EDX) maps of Ti64 C2T 620 80 h, and Ti67 C2T 700 80 h can be seen in figures 4.15 and 4.16, respectively. As expected, it can be seen that the traditional CCT lead to the production of an oxygen-rich layer for both Ti64 and Ti67, which is attributed to the titanium oxide (TiO_2) formation during the CCT process. At the outermost region close to the air/oxide interface, there is also increased aluminium content, which could be associated with the production of aluminium oxide (Al_2O_3).

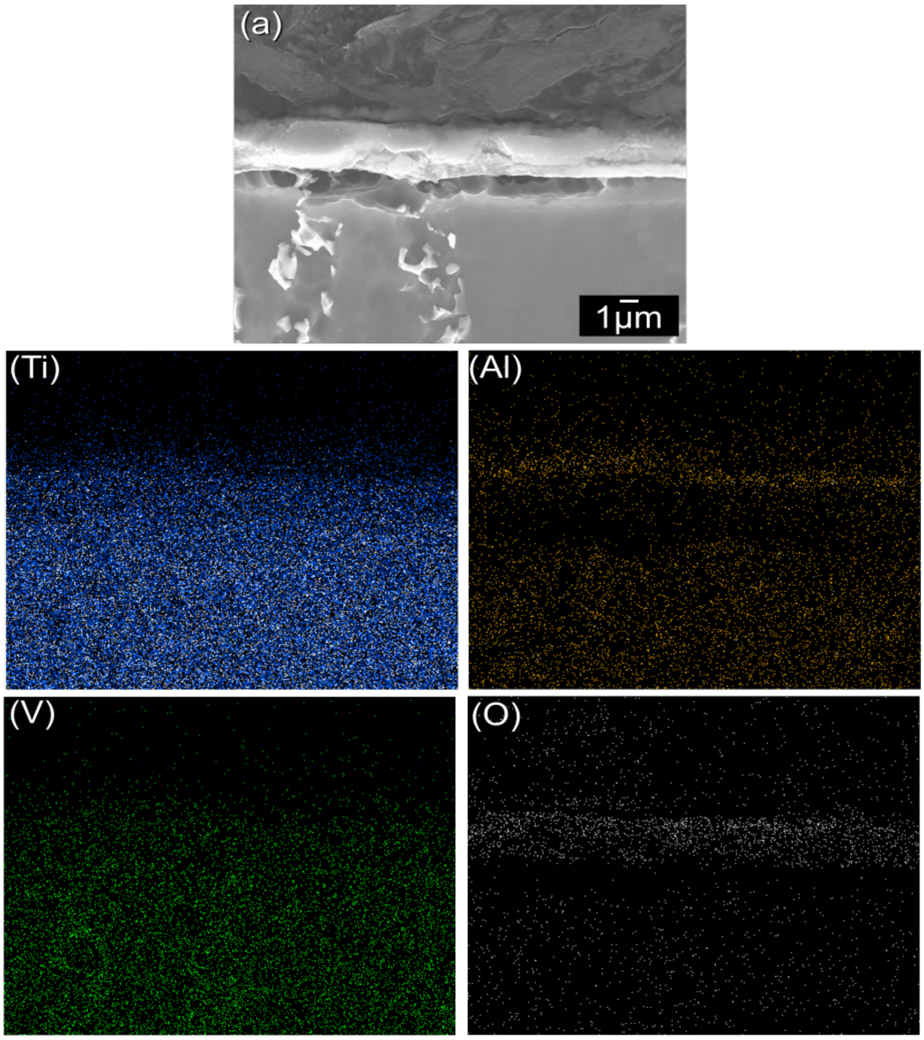

Figure 4.15: EDX elemental maps of a Ti64 C2T 620 80 h cross-section. Where (a) is the SEM image of the region that the maps are of. Each element is labelled.

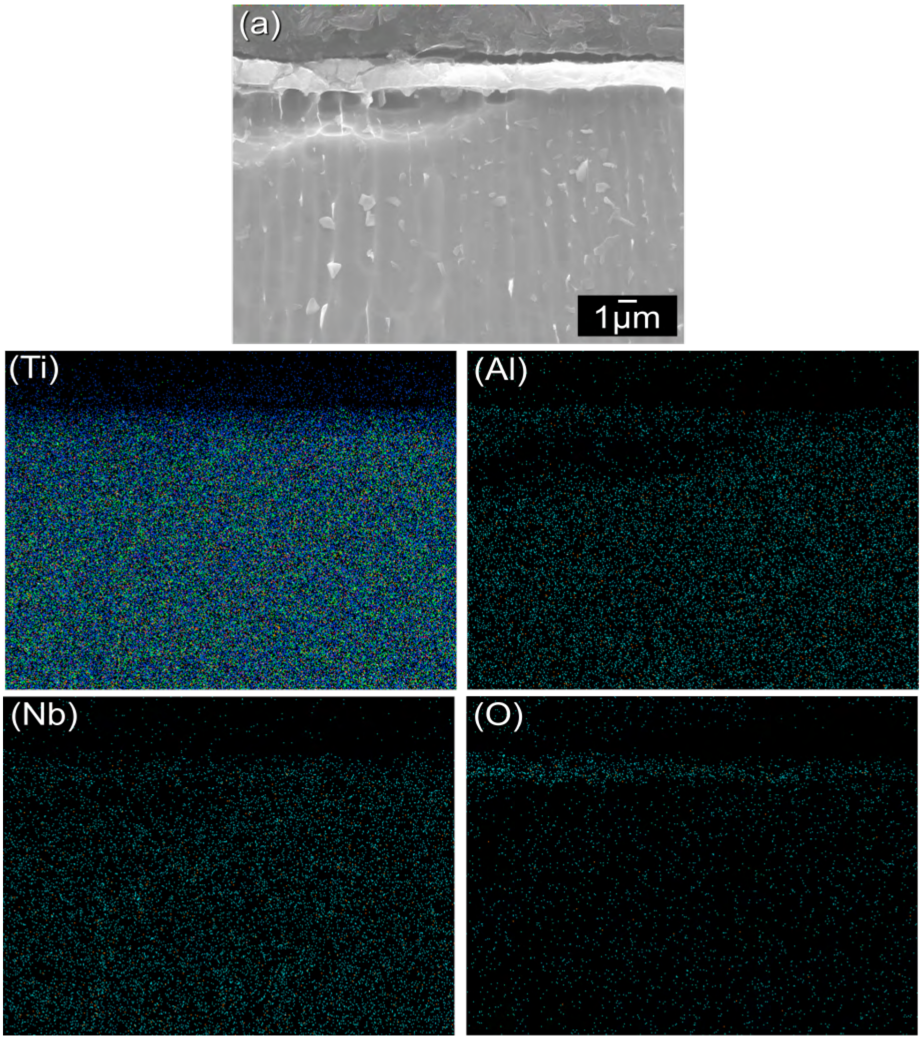

Figure 4.16: EDX elemental maps of a Ti67 C2T 700 80 h cross-section. Where (a) is the SEM image of the region that the maps are of. Each element is labelled.

The influence of the addition of catalytic films prior to CCT on the cross-sectional EDX maps can be seen in figures 4.17, 4.18, 4.20, 4.21, and 4.22.

Ti64 C3T Au 620 and Ti67 C3T Au 700 80 h can be seen in figures 4.17 and 4.18, respectively.

As with C2T, the surface layer can be seen to contain oxygen (O), providing additional evidence of the layer consisting of oxides, most likely attributed to the presence of TiO_2 from CCT.

It can be seen that titanium (Ti) is present in both the surface layer and substrate. However, it is at a higher intensity in the substrate than the surface layer, and the surface layer can be seen to have 2 regions of different intensity, where the subsurface is of lower intensity than the rest of the surface layer.

In the region of the surface layer of lower titanium intensity, it can be seen (Al) that it is an aluminium-rich area. This suggests that there is some aluminium oxide here in addition to the TiO_2.

For Ti67 (figure 4.18), due to niobium (Nb) and gold (Au) having overlapping characteristic X-rays, unfortunately their maps look similar. But it can be seen that there are clusters in the oxide layer (as also seen by bright regions in the BSEM image), which can be assumed to be gold (Au). Additionally, at the interface and in the region underneath the interface there are also brighter regions, which can be assumed to be β grains from the niobium (Nb) stabilising β in these regions, thus suggesting that it is niobium in these areas. Because of this, further elemental analysis was done by glow-discharge optical emission spectroscopy (GDOES), which can be seen in figure 4.19. Due to the relatively poor resolution of the detector used to analyse Ti64 C3T Au compared to Ti67 C3T Au (figure 4.17 vs 4.18), no/limited gold can be discerned within the Ti64 cross-section, but due to the agglomerates at the surface of Ti64 (figure 4.4c) being similar to for Ti67 (figure 4.5c,e,g), it could potentially have the same EDX map as with Ti67.

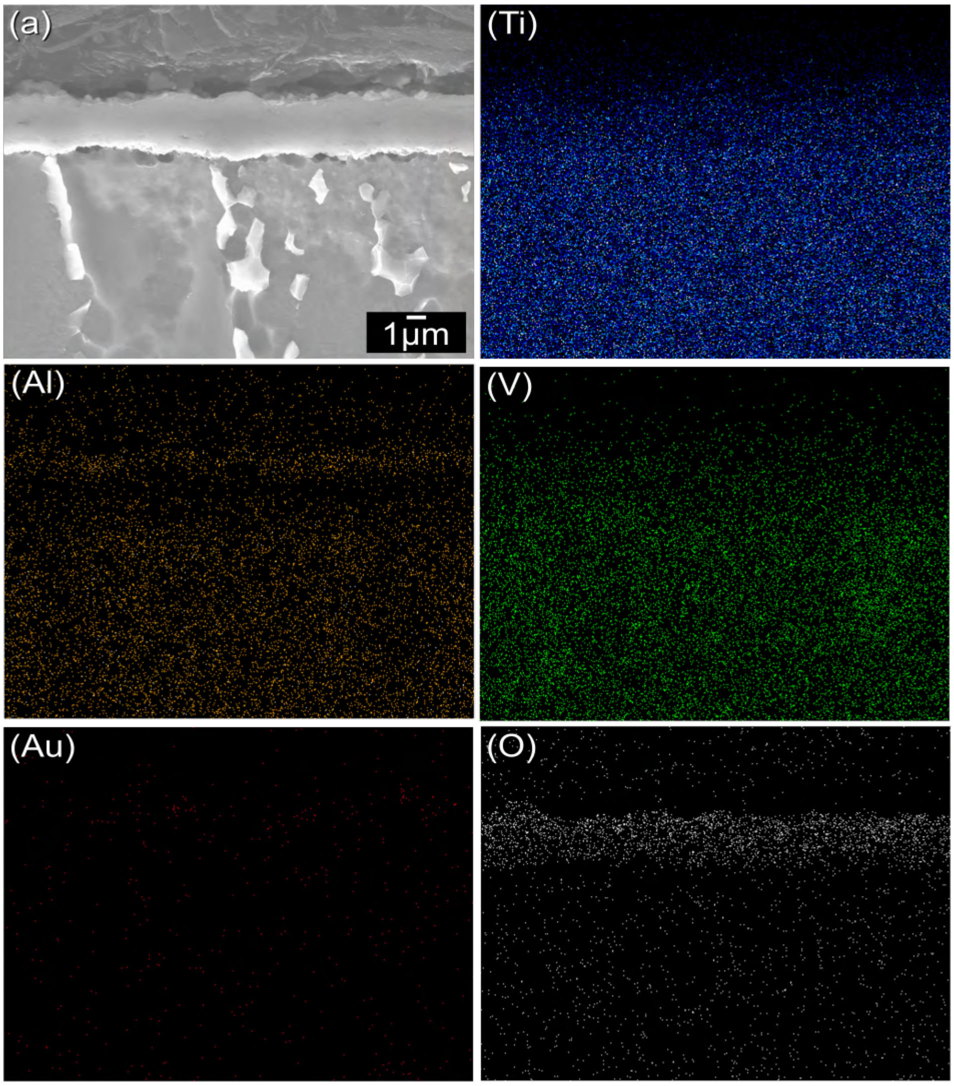

Figure 4.17: EDX elemental maps of a Ti64 C3T Au 620 80 h cross-section. Where (a) is the SEM image of the region that the maps are of. Each element is labelled.

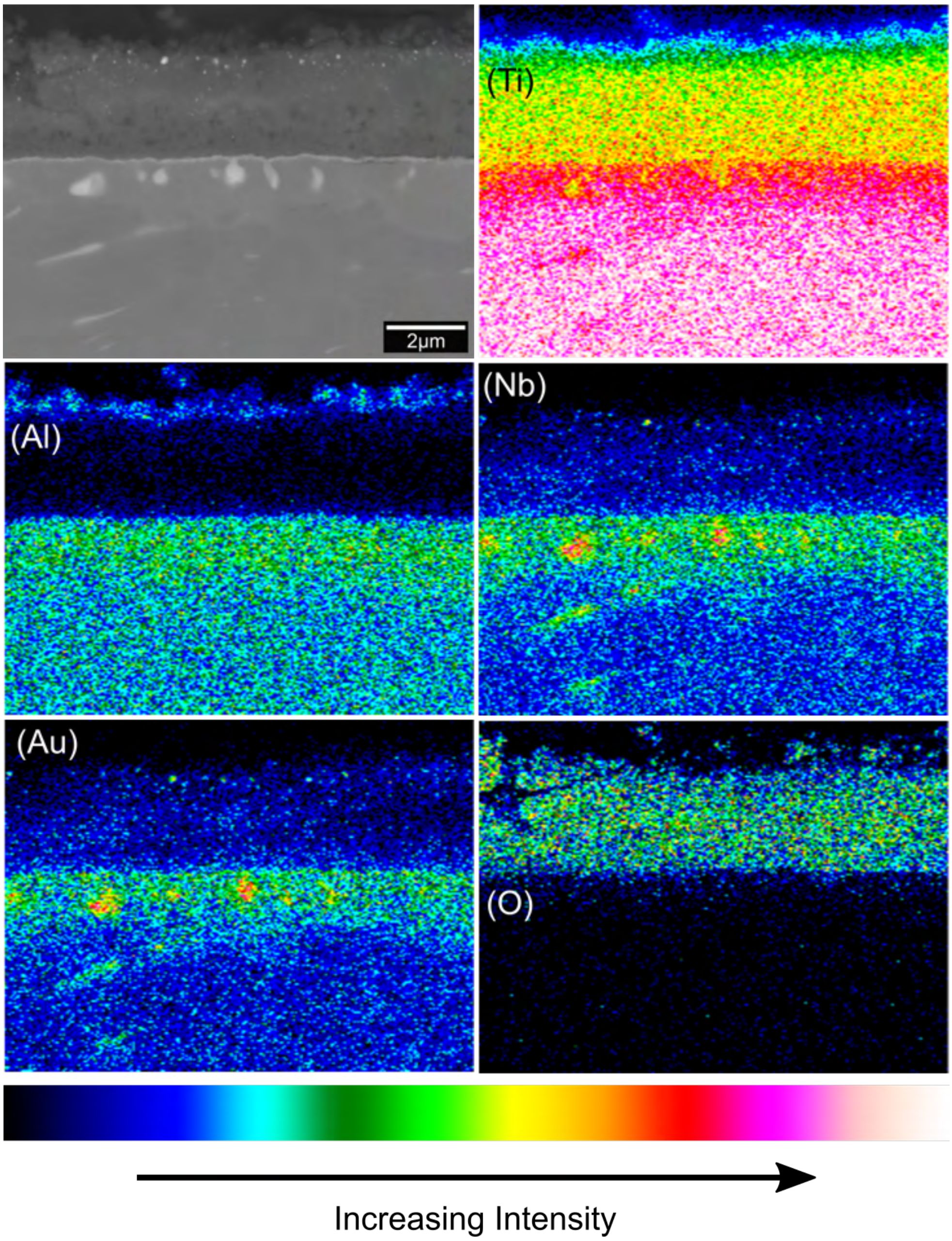

Figure 4.18: EDX elemental maps of a Ti67 C3T Au 700 80 h cross-section. Where (a) is the back-scattered SEM image of the region that the maps are of. Each element is labelled. Colour intensity mapping (relative to each image) was used.

Figure 4.19 shows a GDOES depth profile of Ti67 C3T Au 700 80 h, with a BSEM image overlay to allow comparison of the different regions.

Within the surface layer there is a high % of oxygen (O) further indicating that the layer is an oxide. The % of oxygen reduces with increasing depth into the oxide. A oxygen diffusion zone (ODZ) can also be seen beneath the oxide layer.

Owing to the presence of aluminium (Al) and titanium (Ti) at the subsurface, where the Al content reduces and Ti increases with increasing depth, it can be deduced that there are two layers present: aluminium oxide mixed with titanium oxide, and titanium oxide.

It can be seen that within the surface layer, there is a very low % of niobium (Nb), which increases to above the substrate bulk level once the measurement depth reaches the substrate, and then gradually reduces. This helps with the analysis of figure 4.18 to deduce that the clusters in the oxide are unlikely to contain niobium, but the lighter region underneath the interface does contain niobium.

Due to the lack of calibration sample for gold, it was not possible to get the depth profile for this element.

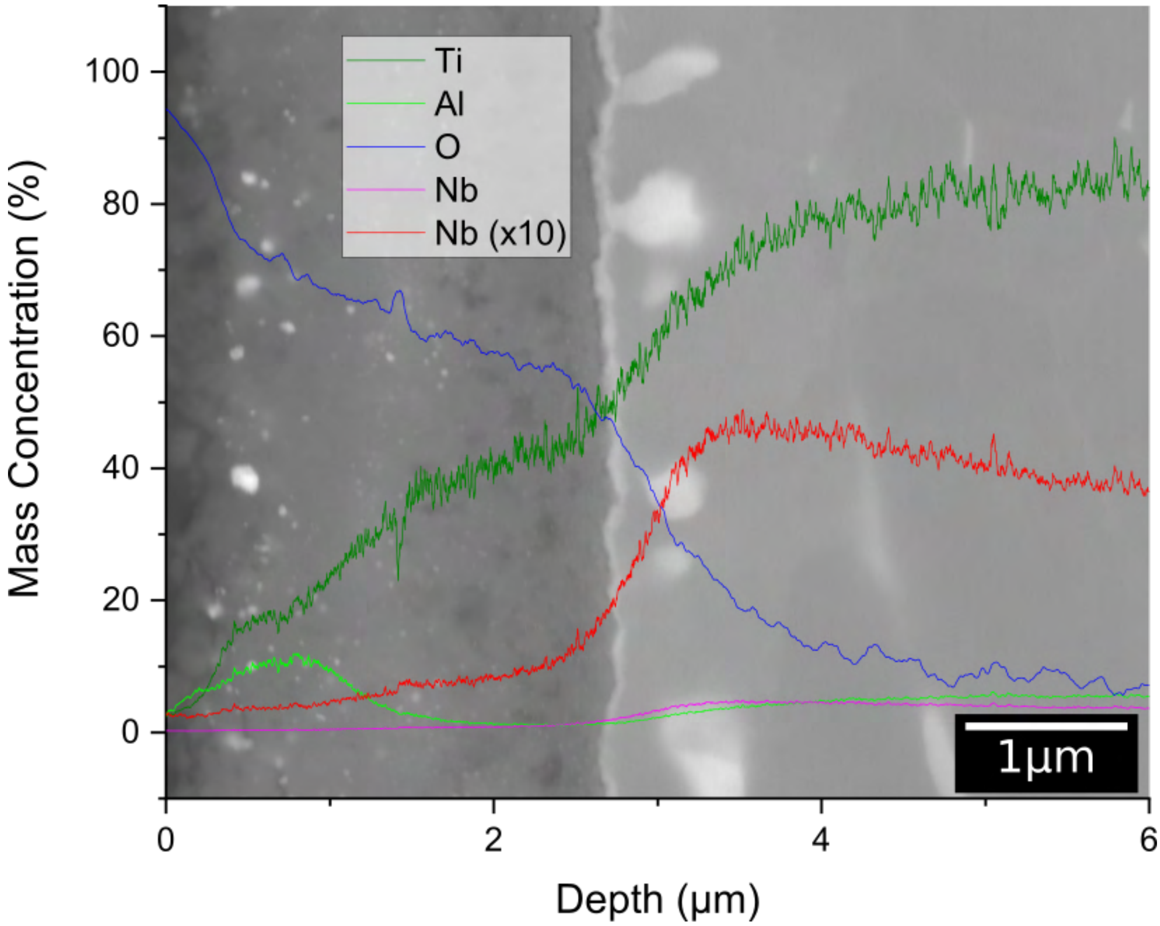

Figure 4.19: Glow-discharge optical emission spectroscopy (GDOES) depth profile of Ti67 C3T Au 700 80 h with a BSEM overlaying the data. Each element is labelled in the figure legend. Please note that niobium (Nb) has been plotted twice, once as standard, and also once multiplied by 10 to allow easier reading of the data.

The influence of changing to Ag/Pd on the Ti64 cross-sectional EDX maps can be seen in figures 4.20, 4.21, and 4.22. Treatment durations of 1, 20, and 80 h were selected for analysis, all at 660 °C.

Short treatment durations of 1 h (figure 4.20) resulted in regions rich in palladium (Pd) and silver (Ag) within the white clusters seen in the BSEM image (a) and demonstrated reduced oxygen (O) intensity. Surrounding these white regions were rich in aluminium (Al). The region bellow the white clusters were rich in titanium (Ti) and oxygen (O), as with C2T (figure 4.15) and C3T Au (figure 4.17).

Increasing the treatment duration to 20 (figure 4.21) and 80 (figure 4.22) h, it can be seen that titanium (Ti) is seen throughout all of the surface layer, but at a lower intensity than in the substrate. The layer contains oxygen (O) throughout, with a slight increase in intensity near the surface, which suggests that the layer consists of a mixture of oxides. At the sub-surface there is an aluminium (Al) -rich layer present, which suggests that this region may be an aluminium oxide. Within the layer, there is a lower intensity of vanadium (V) present, attributed to the poor solubility of this within the layer. At the surface a layer rich in silver (Ag) and palladium (Pd) is present with a stronger Pd intensity than Ag, but unlike the shorter treatment duration, oxygen (O) is still present here, suggesting the formation of an Ag and/or Pd oxide with the increasing treatment duration.

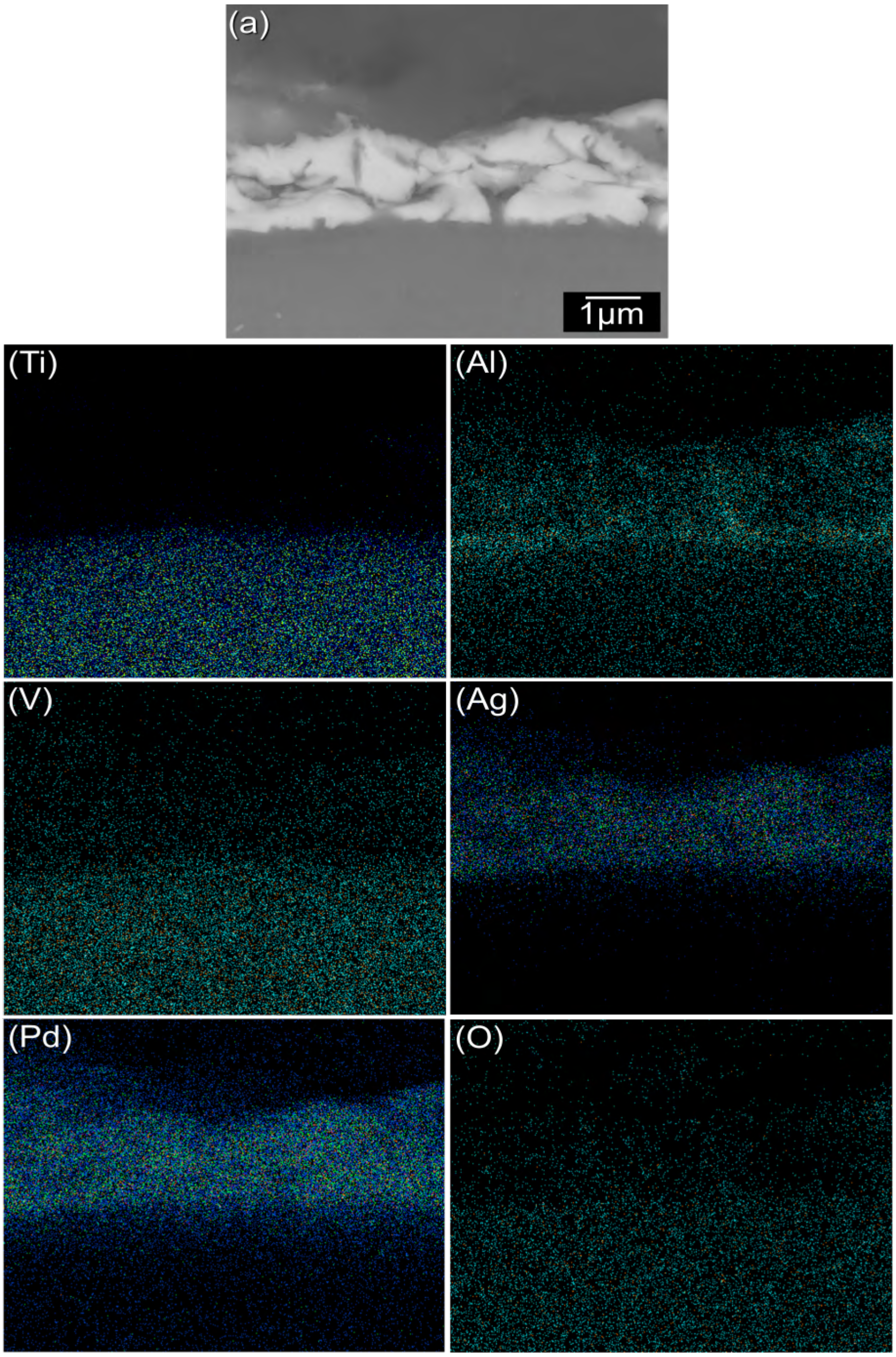

Figure 4.20: EDX elemental maps of a Ti64 C3T Ag/Pd 660 1 h cross-section. Where (a) is the back-scattered SEM image of the region that the maps are of. Each element is labelled.

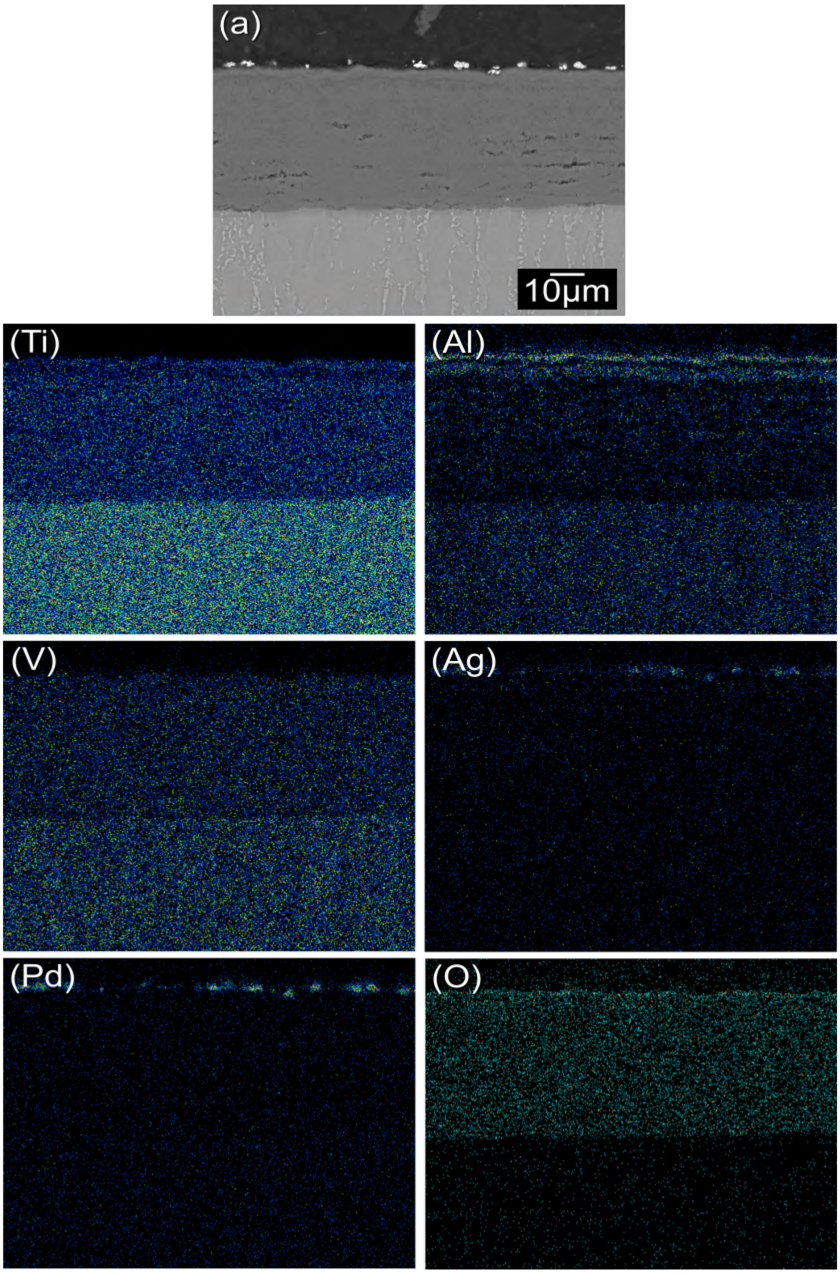

Figure 4.21: EDX elemental maps of a Ti64 C3T Ag/Pd 660 20 h cross-section. Where (a) is the back-scattered SEM image of the region that the maps are of. Each element is labelled.

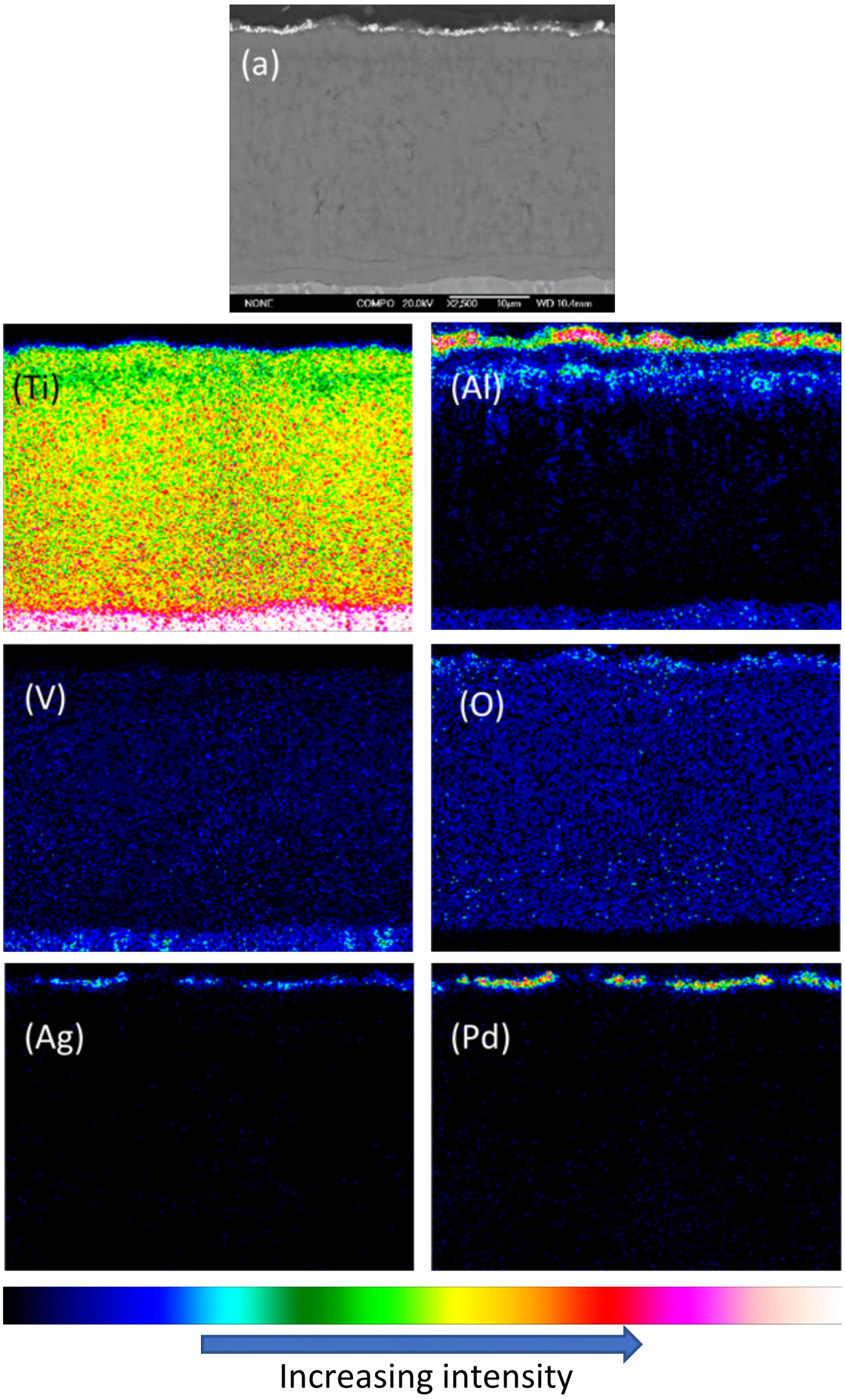

Figure 4.22: EDX elemental maps of a Ti64 C3T Ag/Pd 660 80 h cross-section. Where (a) is the back-scattered SEM image of the region that the maps are of. Each element is labelled. Colour intensity mapping (relative to each image) was used.

Further analysis of the agglomerated structures (as seen in figure 4.8(g)) on the Ti64 C3T Ag/Pd samples in the form of EDX scans of a cross-section of one of the regions containing a surface agglomerate on Ti64 C3T Ag/Pd 660 80 h is shown in figure 4.23.

It can be seen that both the agglomerate and the surrounding area contains oxygen (O), as these regions are likely composed of oxides of the corresponding elemental mapping in each region. Within the agglomerate, a strong intensity for palladium (Pd) is seen, with a slightly reduced intensity of silver (Ag). These are also seen in the region below the surface agglomerate in the lighter region as seen in (a). This suggests the presence of palladium oxide within this region, with some silver/silver oxide clustered throughout.

The surrounding regions excluding this lighter region show a strong intensity for titanium (Ti), aluminium (Al), and vanadium (V), in order of reducing intensity. This suggests that it is a titanium oxide with some regions of aluminium oxide and some vanadium/vanadium oxide dispersed throughout.

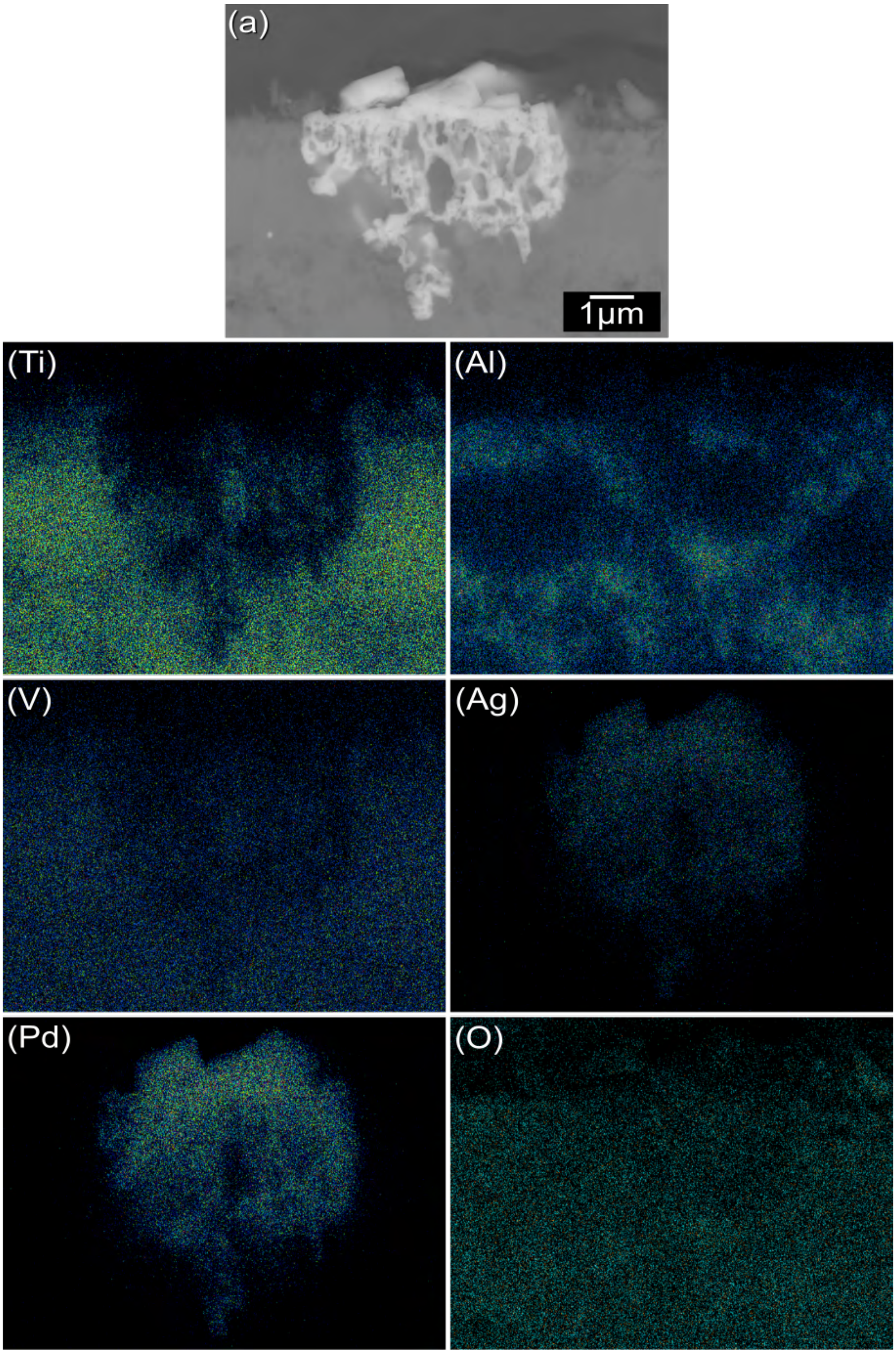

Figure 4.23: EDX map of a cross-section of a Ti64 C3T Ag/Pd 660 80 h agglomerate. Where (a) is a BSEM image of the region and the elements are labelled for their respective image.

Analysis of one of the agglomerates at the surface of Ti64 Ag/Pd 660 20 h (as also seen in figure 4.8(d)) by EDX elemental mapping can be seen in figure 4.24. There are 3 main regions of interest: within the agglomerate, the surrounding area of the agglomerate with elongated needle-like structures, and surrounding this being a smoother surface.

It can be seen that within the agglomerate there is little titanium (Ti), aluminium (Al), and vanadium (V). But there is a presence of palladium (Pd), silver (Ag), and oxygen (O) detected, and they demonstrate reducing intensity respectively.

The region surrounding the agglomerate consisting of needle-like structures shows to be rich in V, with less O than the other regions. The presence of the other elements was not detected in these regions.

The area surrounding this with the smoother appearance displayed the presence of Ti, Al, and O, with the greatest intensity being for Al. This suggests either a mixture of Ti and Al oxides, or due to the nature of EDX analysis, a thin Al oxide layer, with a Ti oxide underneath (due to the stronger intensity for Al) in this region.

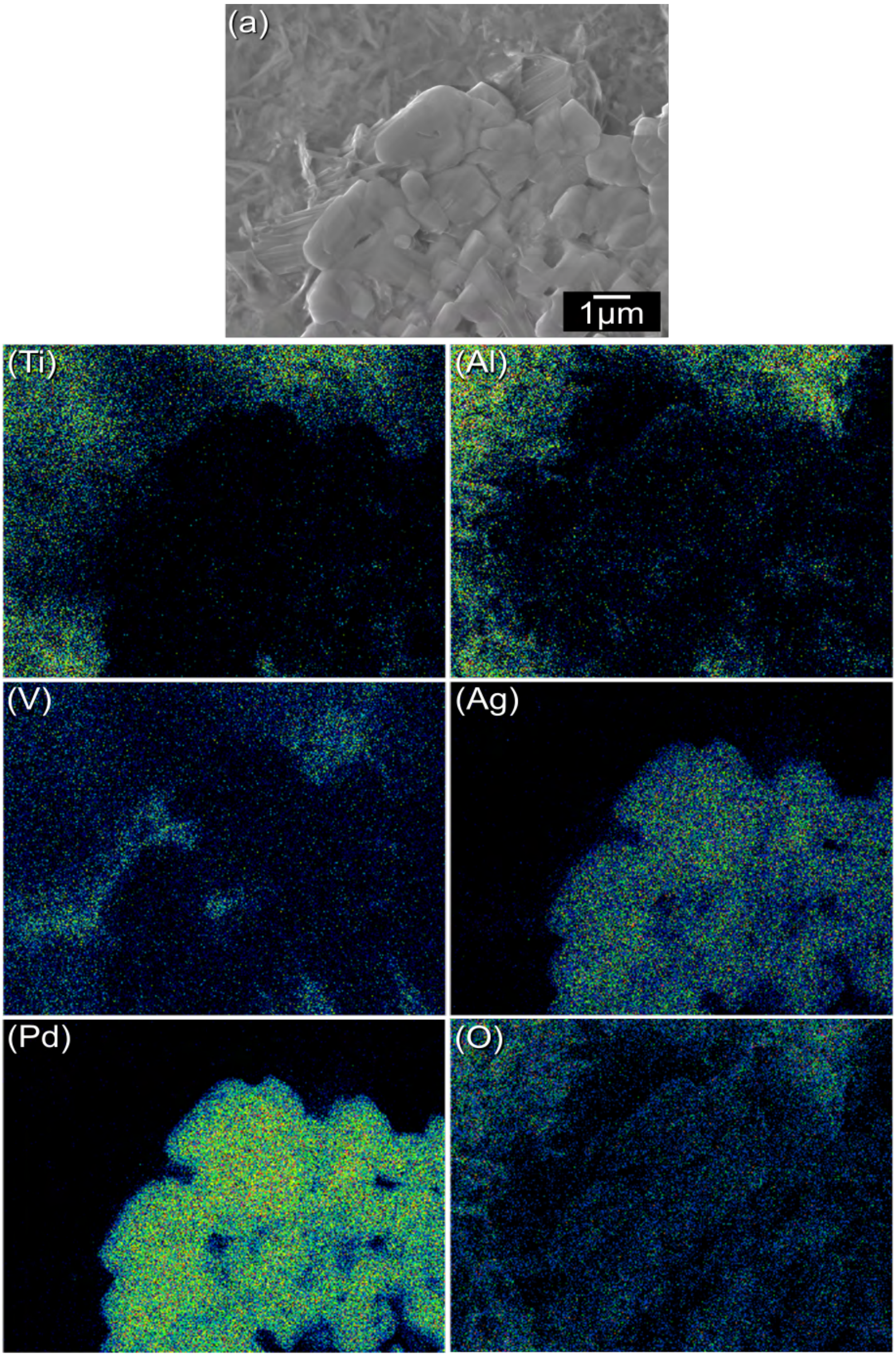

Figure 4.24: EDX mapping scan of a surface agglomerate and surrounding area on a Ti64 C3T Ag/Pd 660 20 h sample. Where (a) is a SEM image of the region scanned, and the elemental maps are labelled as their corresponding element.

Quantitative analysis of the agglomerates seen on the Ti64 C3T Ag/Pd samples can be seen in figure 4.25 in the form of EDX spot analysis. Samples treated at 660 °C for 10, 20, and 80 h were selected. For all treatment durations region A denotes a scan of the agglomerated structure and region B denotes a scan of the surrounding area, both of which are labelled for each treatment. The colours for the labels are matched with their bars for each element in the chart (figure 4.25 (d)).

Oxygen (O) is present in high wt % in both region A and B, confirming the presence of oxides in these regions. There is significantly more O present in region B compared with region A for both 10 and 80 h treatments, suggesting the oxide/s present in the surrounding area of the agglomerate are ones which contain more O, such as TiO_2 and Al_2O_3.

It can be seen that for all treatment durations there is more Ti present in region B than region A. Additionally, increasing the treatment duration to 80 h from 10 and 20 results in a higher wt% of Ti. Region B also contained more Al and V than in the agglomerate. But unlike with Ti, increasing treatment duration to 80 h resulted in a reduction in the wt % of these elements. Combined with the Ti data, this suggests that a potential change in composition with increasing treatment duration from a more aluminium- and vanadium-rich layer to a more titanium-rich one has occurred.

For the 10 h treatment, the wt% of Ag was significantly higher surrounding the agglomerate (region B). Increasing the treatment duration to 20 and 80 h resulted in a significant decrease in the amount of Ag for both regions A and B, where there was a very low wt% detected for both, which may be attributed to the dispersion of Ag throughout the layer with increasing thickness of the layer with increasing treatment duration.

Region A demonstrated a significantly higher wt% of Pd than for region B for all treatments, where there was almost none detected in region B. There was no influence on this when increasing the treatment duration from 10 h to 80 h. This suggests that the agglomerated structures consist of palladium oxide rather than silver oxide due to the relatively high amounts of palladium and oxygen detected in these regions, regardless of treatment duration.

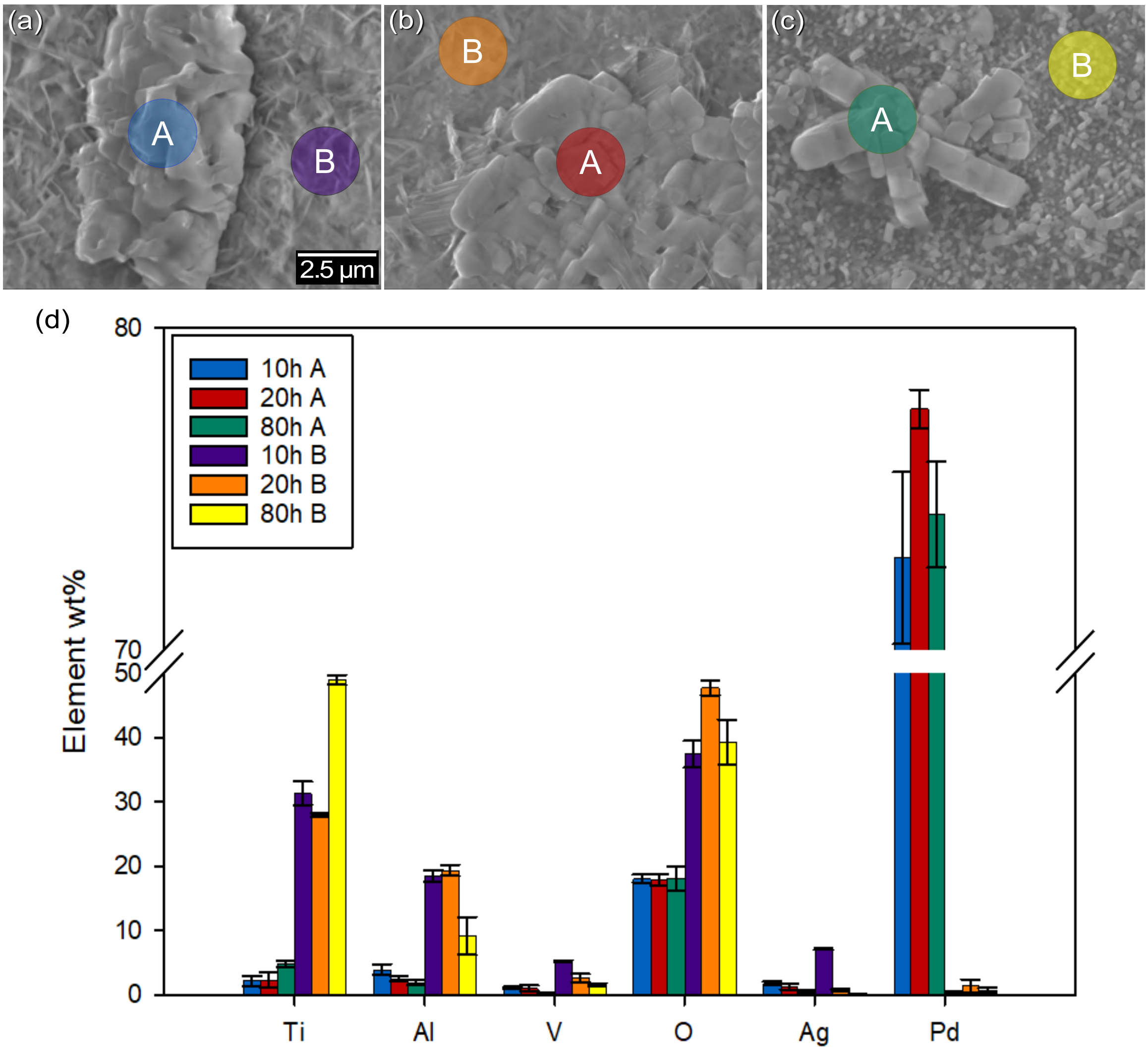

Figure 4.25: EDX spot analysis of Ti64 C3T Ag/Pd 660 10, 20, and 80 h. Where (a) is an SEM image of the analysis region of the C3T Ag/Pd 660 10 h, (b) is an SEM image of the analysis region of the C3T Ag/Pd 660 20 h, (c) is an SEM image of the analysis region of the C3T Ag/Pd 660 80 h, and (d) is a graph representing the quantitative data associated with the EDX spot scans, where region A is within the agglomerate and region B is the from the surrounding area. These regions are labelled on figure 4.25 (a), 4.25 (b), and 4.25 (c), and the colours of the bars are matched with their corresponding region. N.b. y-axis split between 50 and 70 wt% in 4.25 (d). Magnification is the same for all SEM images.

Following from figure 4.25, figure 4.26 shows an EDX analysis of Ti64 C3T Ag/Pd 660 20 h, as this treatment presents a middle point in the transition between the matrix structures thus allowing a comparison between the agglomerate, needle-like structure, and matrix.

It can be seen that the agglomerate (A) consists of palladium (Pd) and oxygen (O), evidencing the presence of palladium oxide here. The matrix consists of high wt % of titanium (Ti), aluminium (Al), and oxygen (O), with low readings of vanadium (V), evidencing the presence of titanium and aluminium oxides. Contrasting with this, the needle-like structure (region C) consists of high wt % of vanadium (V), oxygen (O), and silver (Ag) relative to the other regions. This suggests the presence of vanadium and/or silver oxides being present here. Titanium and aluminium can also be seen here at similar levels to region B, but this may be due to the deep generation depth of the characteristic X-rays resulting from the under-lying region of the needle-like area to also be detected.

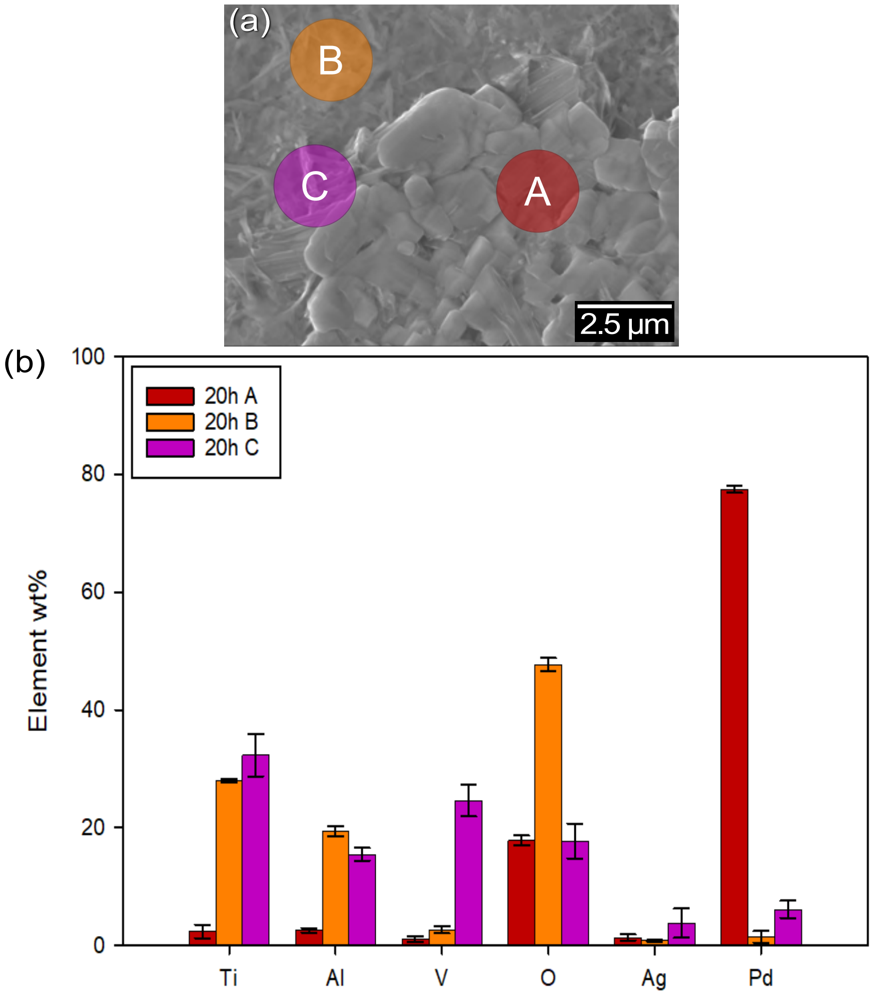

Figure 4.26: EDX spot analysis of Ti64 C3T Ag/Pd 660 20 h. Where (a) is an SEM image of the analysis region and (b) is a graph representing the quantitative data associated with the EDX spot scans. Region A is within the agglomerate, region B is the from the surrounding matrix, and region C is from the needle-like region at the edge of the agglomerate. These regions are labelled on figure 4.26 (a). The regions are colour matched to their representative bars on the chart in figure 4.26 (b).

Deeper analysis was conducted on the Ti64 C3T Ag/Pd 660 20 h sample in the form of TEM. Figure 4.27 shows an elemental map of the region of interest from the surface, and the dashed rectangle in the SEM image shows the region to be removed via focused ion beam (FIB) milling to analyse.

As with previous analysis, areas within the dashed rectangle show high intensity for Ag, Pd, V, Al, and O. This is because it contains both agglomerates which are rich in Ag, Pd, and O, and the needle-like structures, which are rich in V, Al, and O.

Post-FIB milling and subsequent mounting, high-angle annular dark-field scanning transmission electron microscopy (HAADF-STEM) imaging, and subsequent EDX elemental mapping were carried out on the milled cross-section. This can be seen in figure 4.28. A dashed line has been added to distinguish between the sub-surface 'catalytic' layer, and underlying titanium oxide dominated layer.

Three distinct layers can be seen in figure 4.28; a platinum (Pt) rich layer, from the deposition during FIB preparation to protect the specimen; a sub-surface layer, where agglomerates are shown on the LHS and RHS, which show a high intensity for silver (Ag), palladium (Pd), and oxygen (O). The region between these agglomerates is the needle-like area, which presents high intensity for vanadium (V), aluminium (Al), silver (Ag), and oxygen (O); and finally, a layer rich in titanium (Ti), aluminium (Al), vanadium (V), silver (Ag), trace palladium (Pd), and oxygen (O).

Further BF-TEM analysis and subsequent selected area (electron) diffraction (SAD) patterns of the FIB'ed region can be seen in figure 4.29. In the BF-TEM image (a), a top-most layer can be seen consisting of granular and acicular grains, and a sub-layer dominated by columnar grains is present. Just beneath these, an approximately 500 nm layer is present. This consists of nano-crystalline grains of 50-100 nm in diameter. Beneath the nano-crystalline layer is a columnar structured region with well-established columns of 100-200 nm width and 400-600 nm length.

The SAD patterns from the granular grained region (A) identify as palladium oxide (PdO), evidenced by the B = [5,3,1] pattern. Within the granular grains no silver oxides could be detected. As the STEM-EDX (figure 4.28) detected the presence of silver in this region, and the EDX analysis in figure 4.25(d) presented the co-existence of silver and palladium in the granular grains, a PdO-like oxide produced by the substitution of some Pd for Ag, or a Pd(Ag)O phase was considered for here. Additionally, the presence of an Ag-capping layer cannot be dismissed.

SAD patterns of the acicular region (B) revealed the presence of $AgVO_3$ (JCPDS 0029-1152). Faint diffraction patterns were present in the Pd(Ag)O and $AgVO_3$ patterns, potentially due to the presence of an amorphous or poorly crystalline aluminium oxide, as aluminium was present along the grain boundaries in these regions; demonstrated in the EDX map in figure 4.28(Al). However, it is hard to identify an Al_2O_3 phase in the SAD patterns from these regions.

Patterns from the columnar region (C) present some discrete rings, indicating that the region is polycrystalline. An example of a pattern from this region is shown in figure 4.29C. Indexing of this revealed a dominate titanium oxide (TiO_2) phase, and a few aluminium oxide (Al_2O_3) rings. No other oxides could be found in this region. As the elemental mapping of this region (figure 4.28) identified silver (Ag), palladium (Pd), and vanadium (V) in this region, it suggests that they may have been present as substitutional elements to titanium in the titanium oxide, or simply as their pure element.

It can be seen that the interface between the columnar layer and substrate is dense and void-free. SAD patterns taken from the substrate just below the surface layer revealed an expanded HCP structure of α-Ti(O), otherwise known as the oxygen diffusion zone (ODZ).

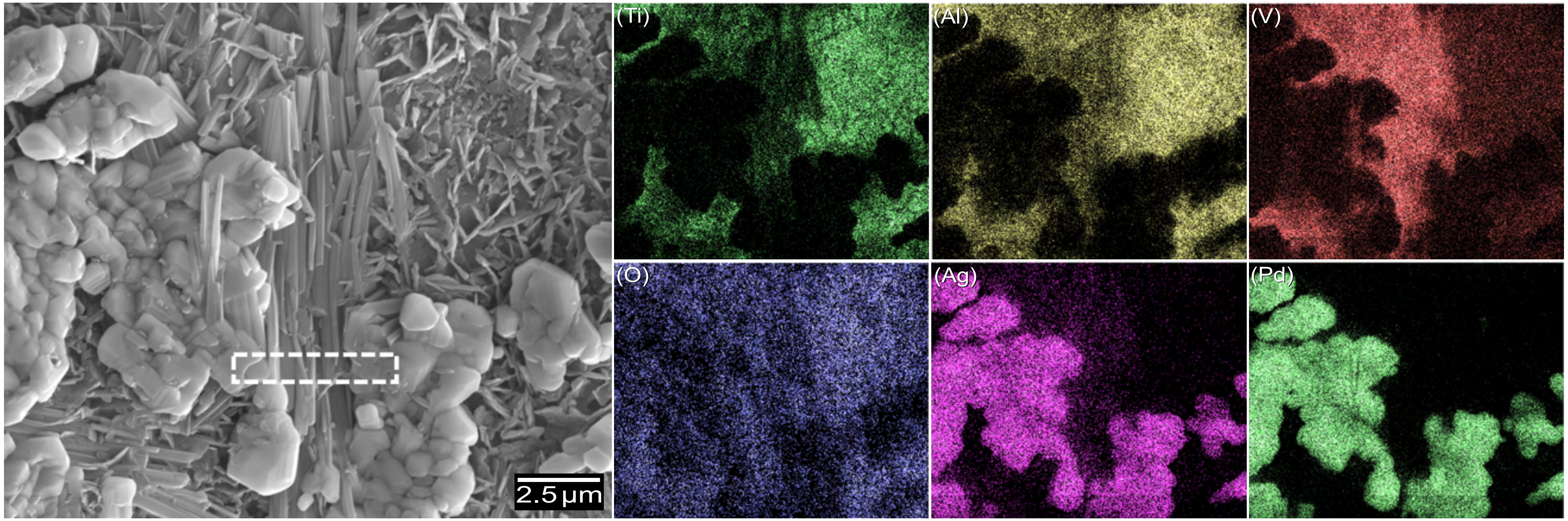

Figure 4.27: SEM-EDS showing the morphology and elemental distribution from top of the C3T Ag/Pd 660 20 sample surface. The FIB sampling location is highlighted in dashed rectangle in the SE image.

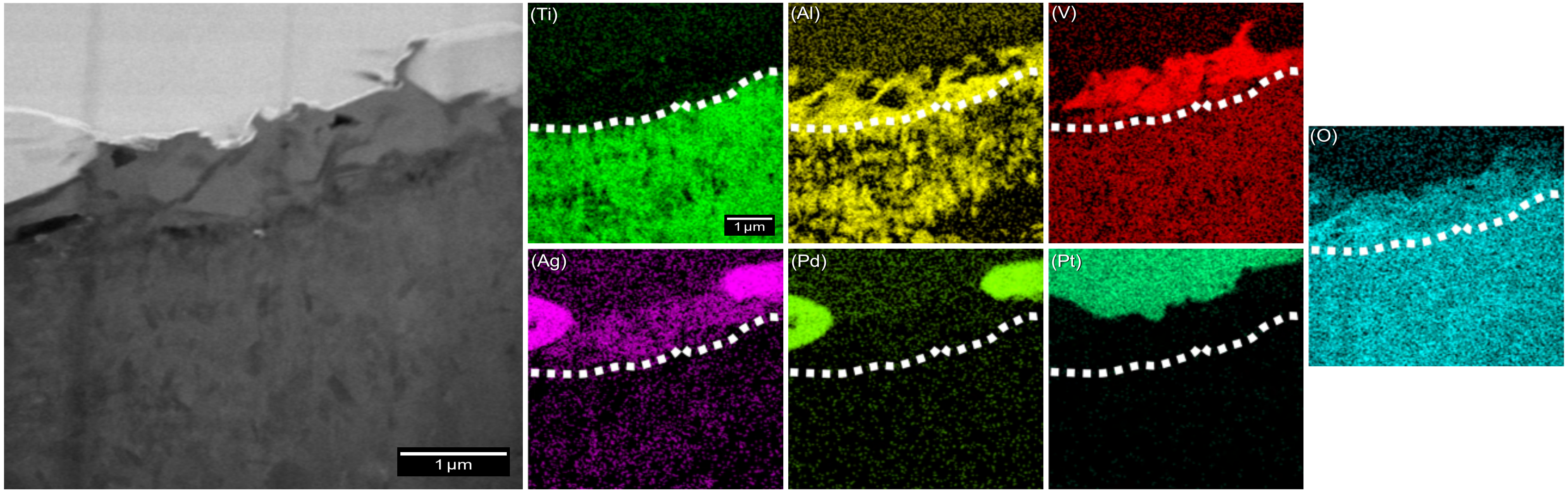

Figure 4.28: STEM-EDX analysis for the FIB-prepared C3T Ag/Pd 660 20 sample showing the elemental distribution cross-sectionally. The region for testing is shown in the HAADF image, EDX elemental maps are labelled Ti, Al, V, O, Ag, Pd, Pt. N.b. the Pt layer shown was deposited during the FIB sample preparation process. A dashed line indicates the boundary between Ti substrate and the 'catalytic' topmost substances.

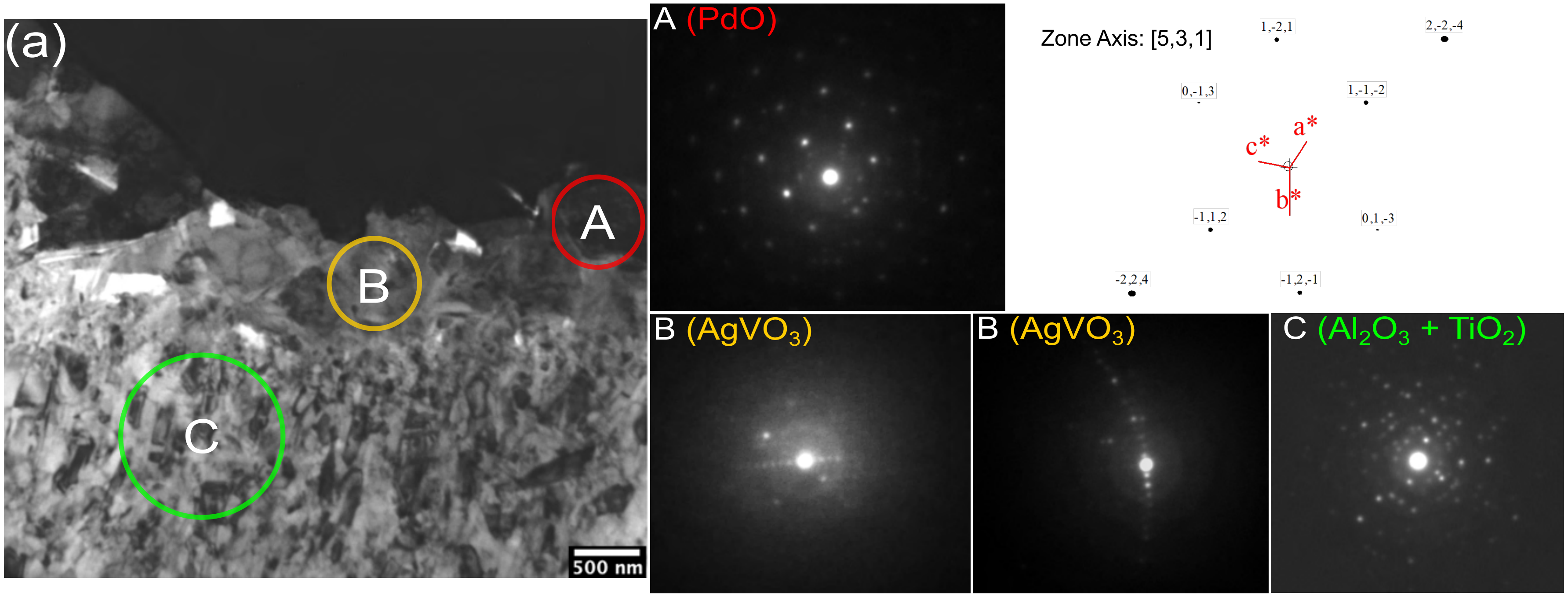

Figure 4.29: BF-TEM analysis of C3T Ag/Pd 660 20 and the corresponding SAD patterns. Where (a) is the BF-TEM image and regions of interest A, B, and C from image (a) are shown within the coloured circles. These regions were used for SAD patterning. Region A shows patterns of PdO, region B shows patterns of AgVO$_3$, and region C shows patterns of Al$_2$O$_3$ and TiO$_2$.

4.2.3 Phase

The results of X-ray diffraction (XRD) analysis are shown in figures 4.30, 4.31, 4.32, and 4.33. The phases and orientations have been displayed in as much detail as possible.

Untreated samples for both Ti64 (figure 4.30) and Ti67 (figure 4.31) showed α-Ti to be the dominate phase, with a few weak peaks of β-Ti.

CCT lead to the production of a rutile phase on all treatments, as expected. However, for the Ti67 C2T treatments (figure 4.31), alumina was also present. It can be seen that increasing the treatment temperature from 620 to 660 (and 660 to 700 for Ti67) did not result in a change in what phases were detected at the surface.

The application of catalytic films prior to CCT (C3T) resulted in some additional peaks being present, irrespective of alloy. These typically included peaks of the element which was pre-deposited.

For Ti64 C3T Ag/Pd, it can be seen that treatments at/above 10 h (figure 4.32) resulted in the detection of an aluminium oxide and palladium oxide. Aluminium oxide was also present when individual Ag or Pd elements were pre-deposited (figure 4.33), and palladium oxide when Pd was deposited.

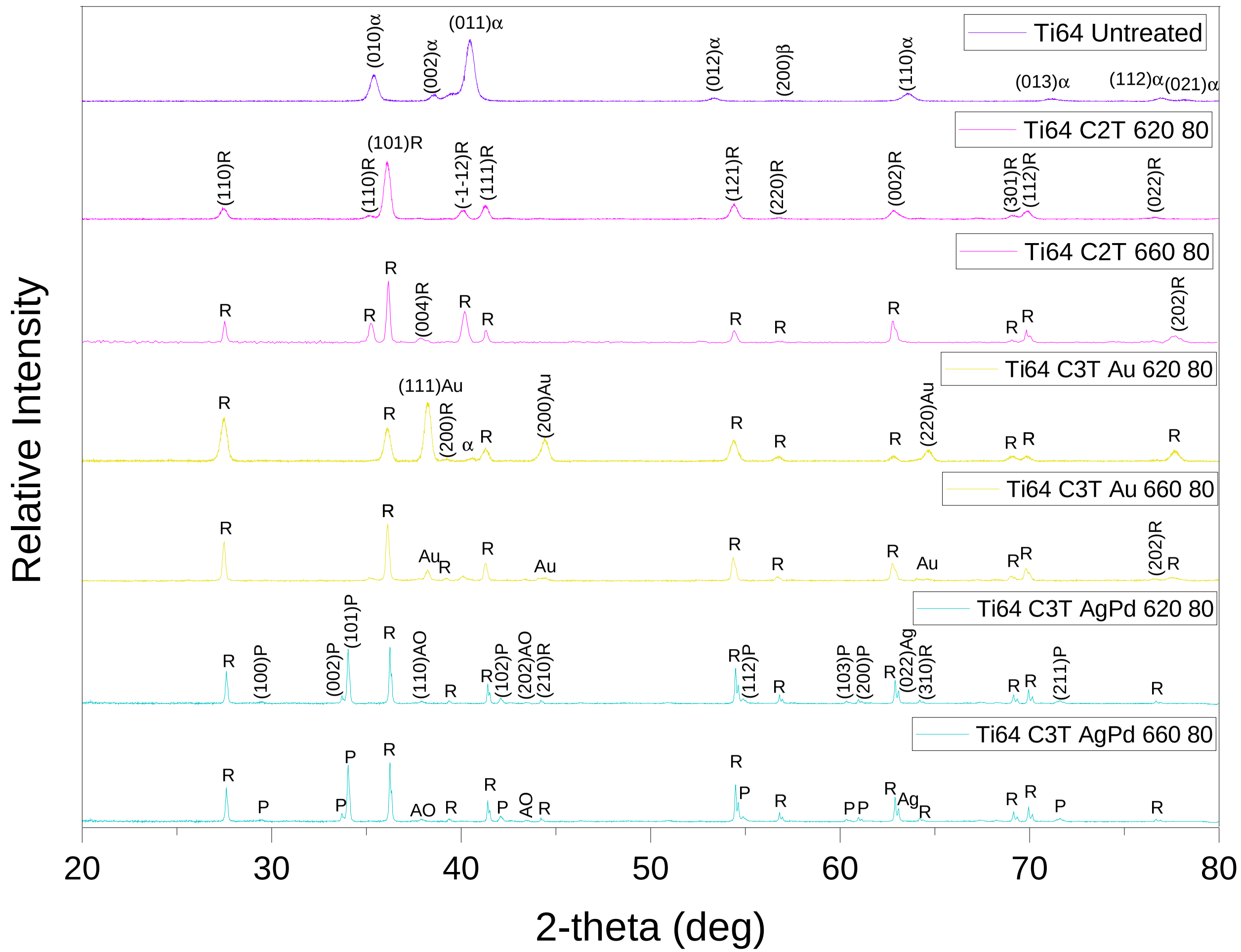

Figure 4.30: XRD analysis of Ti64 untreated, C2T, C3T Au, C3T AgPd. Treatment conditions were either 620 or 660 C for 80 h. α = alpha titanium, β = beta titanium, R = rutile, Au = gold, P = palladium oxide, AO = aluminium oxide, Ag = silver.

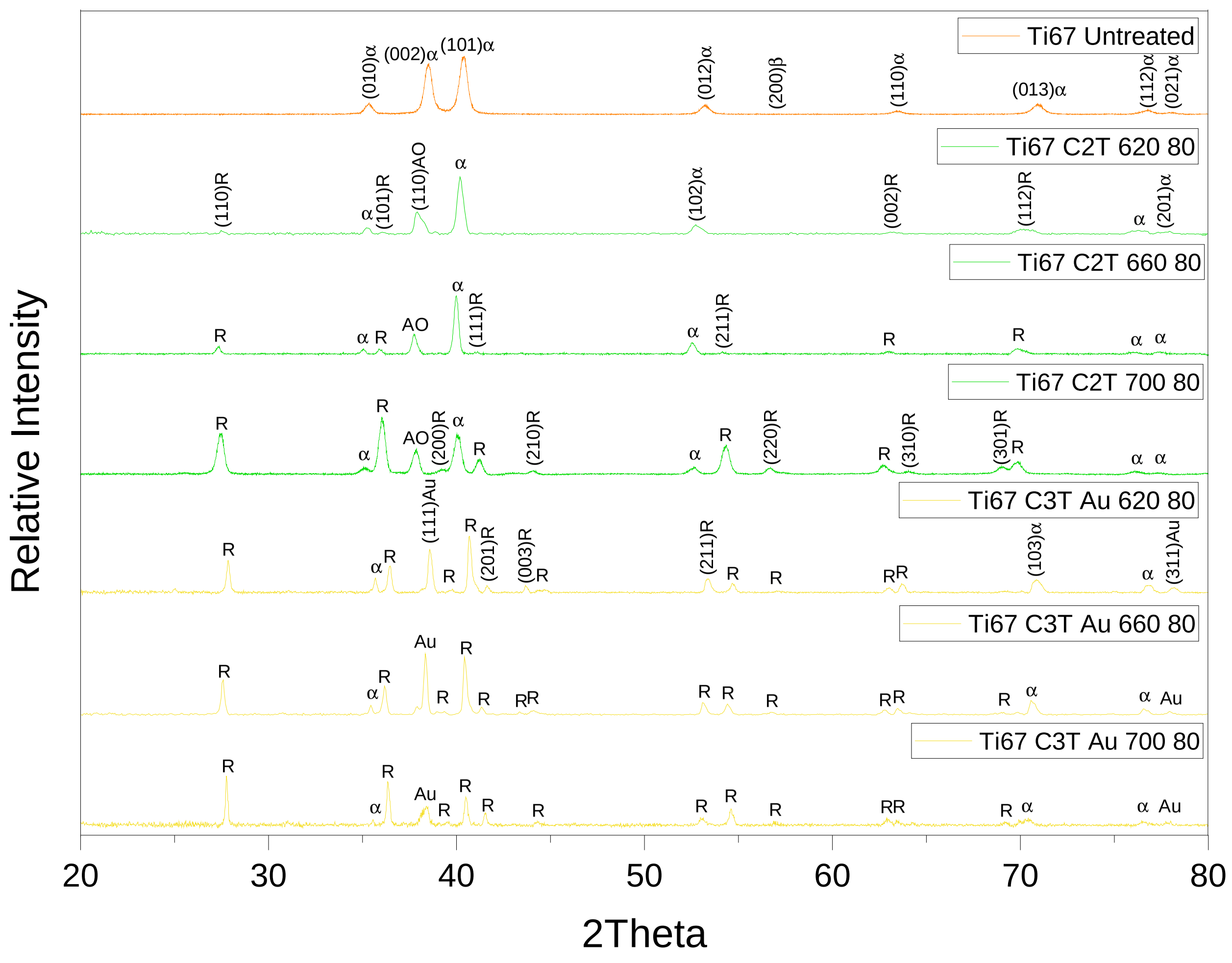

Figure 4.31: XRD analysis of Ti67 untreated, C2T, C3T Au. Treatment conditions were either 620, 660, or 700 C for 80 h. α = alpha titanium, β = beta titanium, R = rutile, Au = gold.

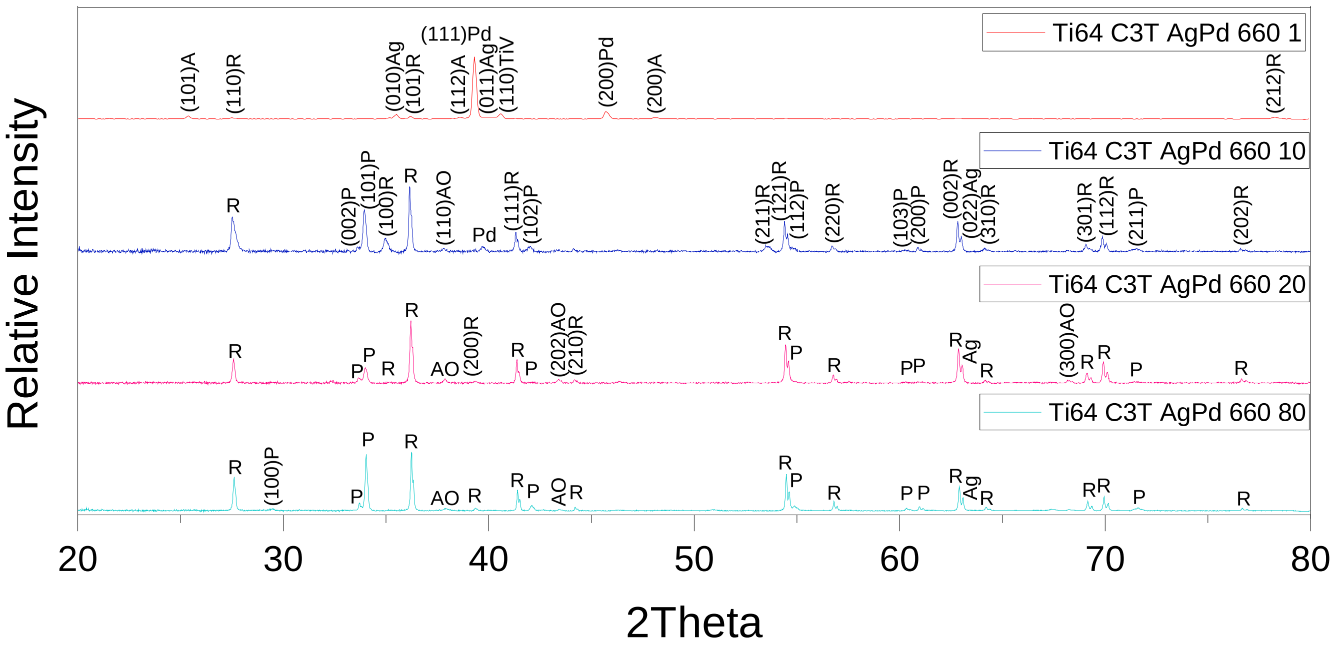

Figure 4.32: XRD analysis of Ti64 C3T AgPd treated at 660 for either 1, 10, 20, or 80 h. A = anatase, R = rutile, Ag = silver, Pd = palladium, P = palladium oxide, AO = aluminium oxide.

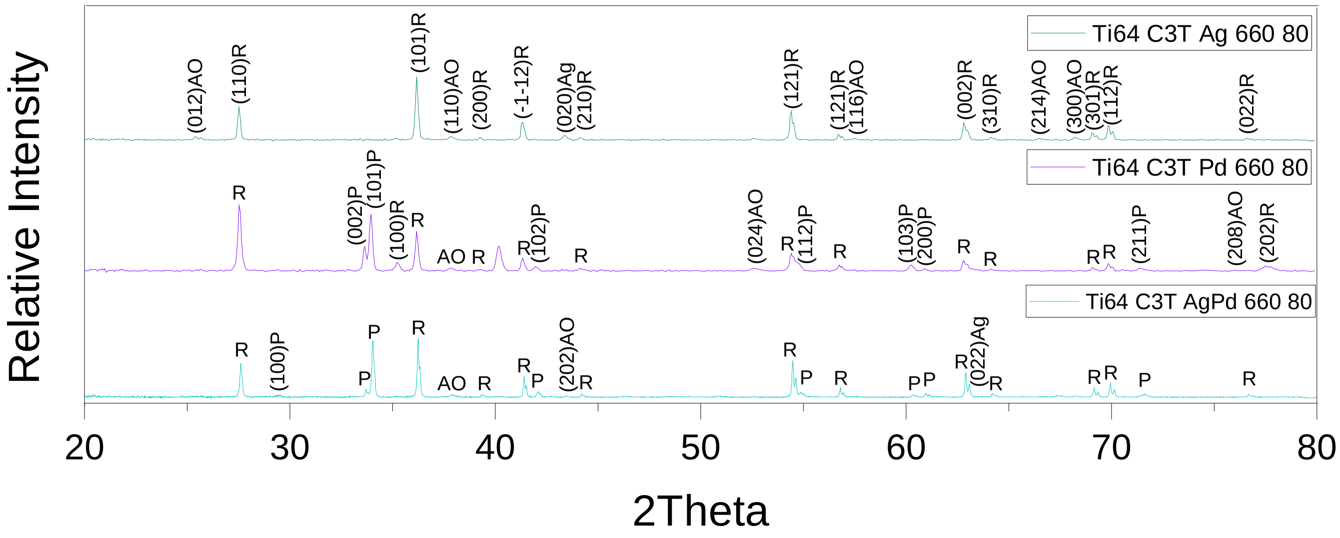

Figure 4.33: XRD analysis of Ti64 C3T Ag, C3T Pd, and C3T AgPd. Treatment conditions were 660 C for 80 h. AO = aluminium oxide, R = rutile, P = palladium oxide, Ag = silver.

4.2.4 Layer Thickness

A chart comparing the surface layer thickness of Ti64 C2T and C3T Au treated at 580, 620, 660, and 700 °C for 80 h can be seen in figure 4.34.

It can be seen that the addition of a catalytic layer resulted in an increased surface layer thickness for all but the 700 °C treatment. This was especially true at 580 °C, where a 255 % growth increase took place.

For the traditional C2T treatments, as expected, increasing treatment temperature resulted in an increase in surface layer thickness. However, this was not the case for C3T Au, as increasing from 580 to 620 and then 660 to 700 did not yield a significant change in layer thickness. This indicates either a change in thermodynamics or layer morphology altering the rate in which layer growth occurs over these temperature ranges.

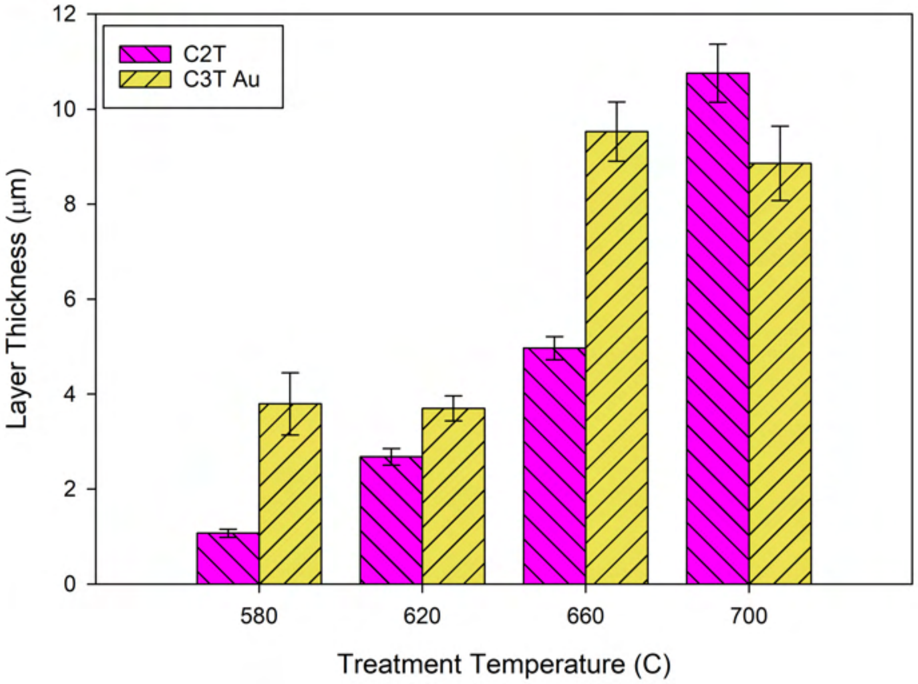

Figure 4.34: Surface layer thickness of Ti64 C2T and C3T Au treated at either 580, 620, or 660 °C for 80 h.

Surface layer thickness for Ti67 C2T and C3T Au treated at 620, 660, and 700 °C for 80 h is charted in figure 4.35.

As expected, for both C2T and C3T Au increasing treatment temperature resulted in an increase in layer thickness.

The addition of the Au catalytic layer prior to treatment resulted in a significant increase in layer thickness compared with C2T, with an average increase of 154 %. This was especially true at 620 °C, where a 240 % increase occurred from 0.4 to 1.4 μm.

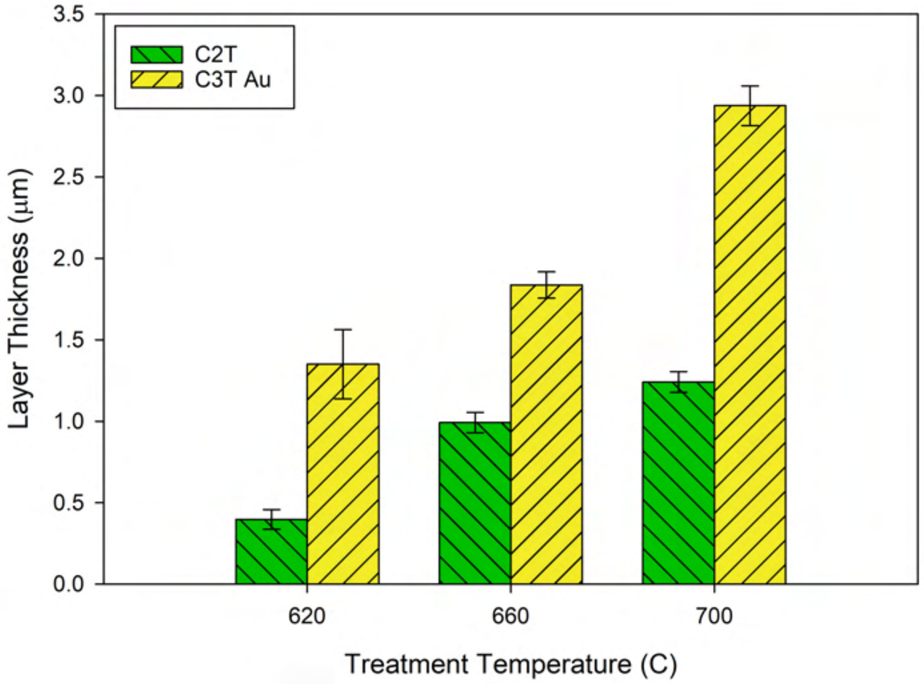

Figure 4.35: Surface layer thickness of Ti67 C2T and C3T Au treated at either 620, 660, or 700 °C for 80 h.

Surface layer thickness measurements of Ti64 C2T and C3T Ag/Pd treated at either 580, 620, or 660 °C for 80 h can be seen in figure 4.36.

As expected, for both C2T and C3T AgPd increasing treatment temperature increased layer thickness.

Regardless of treatment temperature, C3T Ag/Pd resulted in a significantly larger layer thickness compared with C2T, where on average an approximate 20-fold increase occurred.

Comparing the same treatment temperatures of 580, 620, and 660; C3T Ag/Pd 580 resulted in a 2800 % increase from 1.1 to 32 μm; 620 resulted in a 1640 % increase from 2.7 to 47 μm; 660 resulted in a 1920 % increase from 5 to 101 μm. These findings signify the great catalytic effect of the Ag/Pd layer compared with the conventional C2T treatment with Ti64.

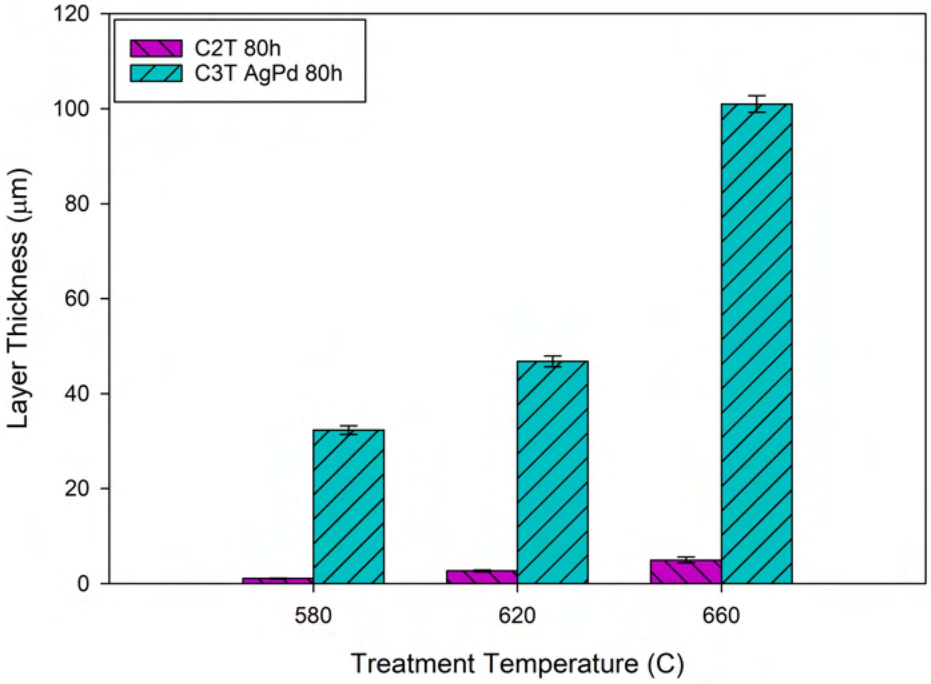

Figure 4.36: Surface layer thickness of Ti64 C2T and C3T Ag/Pd treated at either 580, 620, or 660 °C for 80 h.

The surface layer thickness of C2T and C3T Ag/Pd treated at 660 °C for different time durations is charted in figure 4.37.

It can be seen that the Ag/Pd catalytic layer pre-deposition resulted in a much thicker oxide layer than the coupons without pre-deposition. As can be seen, the growth rate over the time period (1-80 h) is logarithmic. This is due to the diffusion-based nature of the layer growth, and therefore 2 regions have been separated along the C3T Ag/Pd curve to allow more in-depth analysis.

A significant catalytic effect of Ag/Pd on the formation of the oxide layer on Ti64 was observed and a growth rate of about 2 μm/h was extrapolated for C3T Ag/Pd treated coupons when treated within 40 h. This was 22 times faster than that of the C2T treatment coupons within the same time period. It can be seen that the growth rate is not quite linear when compared with the line of fit, due to the layer growth impeding diffusion with increasing growth, and therefore reducing the rate.

When the treatment duration increases to over 40 h, the oxide layer growth rate was reduced to 0.5 μm/h, but this is still 5 times higher than the growth rate of the C2T samples. The growth rate almost perfectly matches the line of fit ($R^2 = 0.99999$), meaning it is linear and therefore the maximum potential thickness growth has not yet been reached. Additionally, it can be seen that the y-intercept point is approximately 60 μm; but this is not the starting thickness. This is due to the presence of the surface layer impeding diffusion with increasing thickness, as mentioned previously.

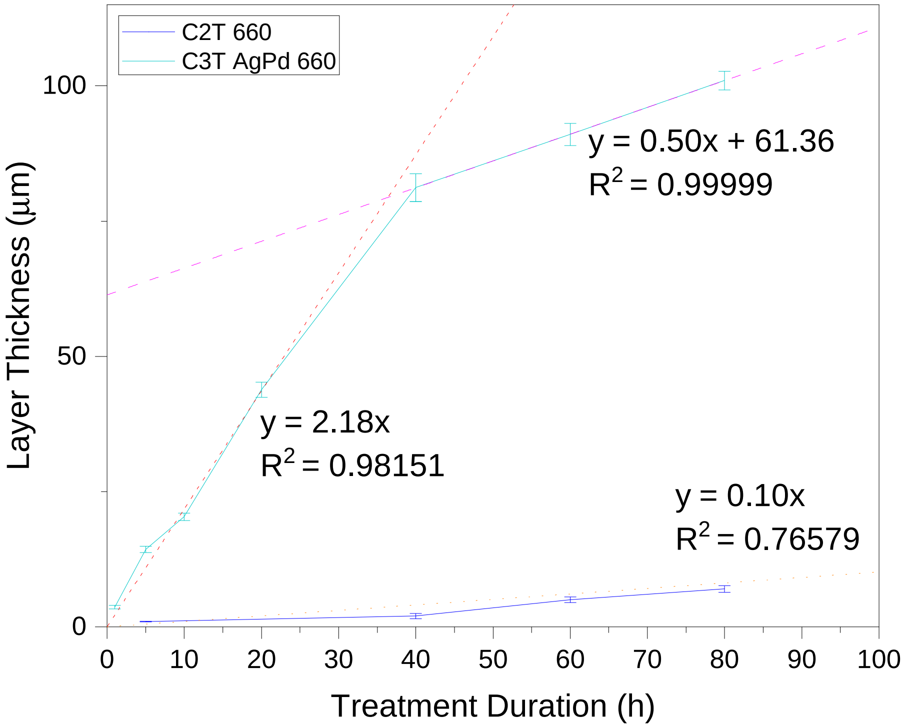

Figure 4.37: Surface layer thickness of Ti64 C2T and C3T Ag/Pd treated at 660 °C for various durations between 1 and 80 h for C3T Ag/Pd, and 5 and 80 h for C2T.

The thickness of the surface layers created on Ti64 during treatment at 660 °C for C2T and C3T Ag, Pd, and Ag/Pd for either 5 or 80 h are shown in figure 4.38. Please note, the axis has been split between 20 and 80 μm to allow easier reading of the thinner layers.

It can be seen when comparing the 5 h treatments with the 80 h, but keeping the other conditions equal, as expected, the 80 h treatments resulted in a much thicker layer than the respective 5 h.

At the same treatment duration, the C3T catalytic layers were able to significantly increase the layer thickness when compared with C2T, although this was not as significant an increase for C3T Pd as it was for C3T Ag or Ag/Pd.

For the shorter (5 h) treatment, the C3T Ag was 1110 % thicker than C2T, and C3T Ag/Pd 22 % thicker than C3T Ag. However, increasing treatment duration to 80 h it can be seen that this is not the case as the pre-deposition of Ag increased the thickness compared with Ag/Pd, where C3T Ag/Pd was 1933 % thicker than C2T and C3T Ag 37 % thicker than C3T Ag/Pd. This suggests that, compared with Ag, the bimetallic catalyst had a greater effect in the initial treatment stages, and this reduced with increasing treatment duration to be overtaken by the Ag catalytic layer.

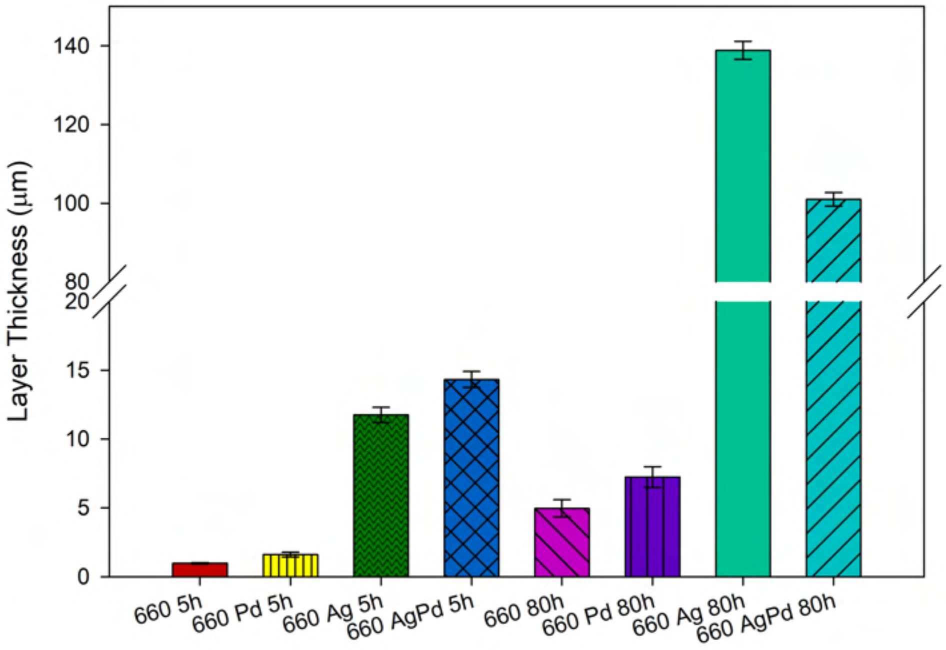

Figure 4.38: Surface layer thickness of Ti64 C2T and C3T Ag, Pd, and Ag/Pd. Treatment conditions are for 5 or 80 h at 660 °C. Please note axis split between 20 and 80 μm.

4.3 Mechanical and Tribological Performance

4.3.1 Micro-hardness

4.3.1.1 Surface Hardness

Figure 4.39 charts the average surface micro-hardness for Ti64 untreated, C2T, and C3T Au. The treatment conditions varied from 580 to 700 °C, for 80 h. It can be seen that the ceramic conversion treatment produced a surface layer which is significantly harder compared to untreated ($\approx$ 320 HV0.05).

For both C2T and C3T Au, increasing treatment temperature resulted in an increase in surface hardness, where C2T demonstrated a 1.8 times increase from $\approx$ 540 to $\approx$950, and C3T Au demonstrated a 1.2 times increase from $\approx$ 610 to $\approx$ 760 HV0.05. However, for C2T, other than the initial increase from 580 to 620, this was not a significant increase between temperature increases. This is attributed to the fact that although the layer thickness increased, the quality of the higher temperature treatments was not adequate enough to significantly increase the hardness of the layer.

When comparing C2T and C3T Au, it can be seen that the C3T Au produced a surface layer which, other than when treated at 580 °C, was not as hard as C2T. This is not as expected due to the previous findings of C3T Au's layer being thicker than that of C2T (figure 4.34). It may be attributed to a reduced ODZ, so therefore reduced oxide layer support. The increase at 580 is likely due to the much thicker layer produced for C3T Au compared with C2T with this treatment condition.

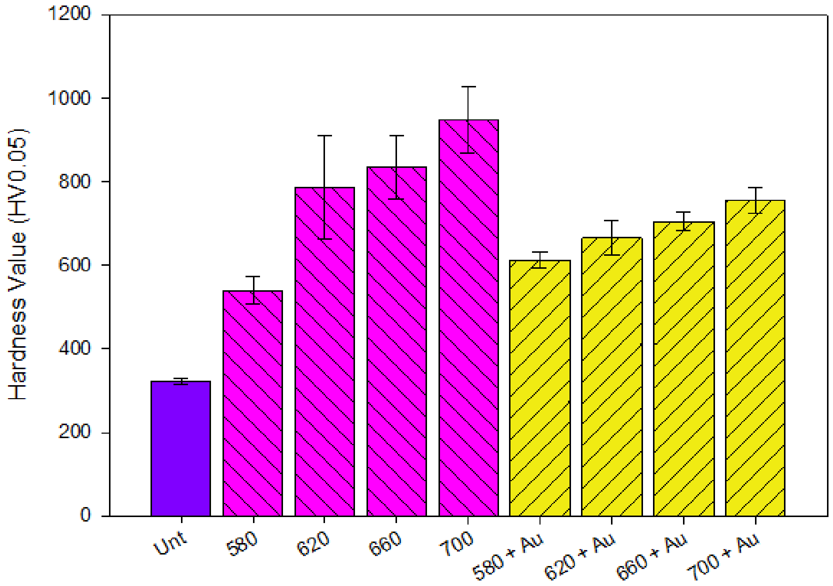

Figure 4.39: Surface micro-hardness of Ti64 untreated, C2T, and C3T Au. Treatment conditions are of 580, 620, 660, and 700 °C, for 80 h.

The average surface micro-hardness for Ti67 untreated, C2T, and C3T Au can be seen in figure 4.40. Ceramic conversion treatment was able to yield surface layers which are significantly harder than the untreated Ti67 (≈ 290 HV0.05).

For both C2T and C3T Au, increasing treatment temperature resulted in a slight increase in surface hardness. The increase was likely not significant due to the fact that the oxide thickness increase (figure 4.35) was only marginal between treatment temperatures.

When comparing C2T with C3T Au for the same treatment temperature, it can be seen that C3T Au is not as hard as C3T. This is potentially due to a reduction in support underneath the surface layer from having a reduced oxygen inward diffusion, and the relatively high load used of HV0.05 for such thin surface layers.

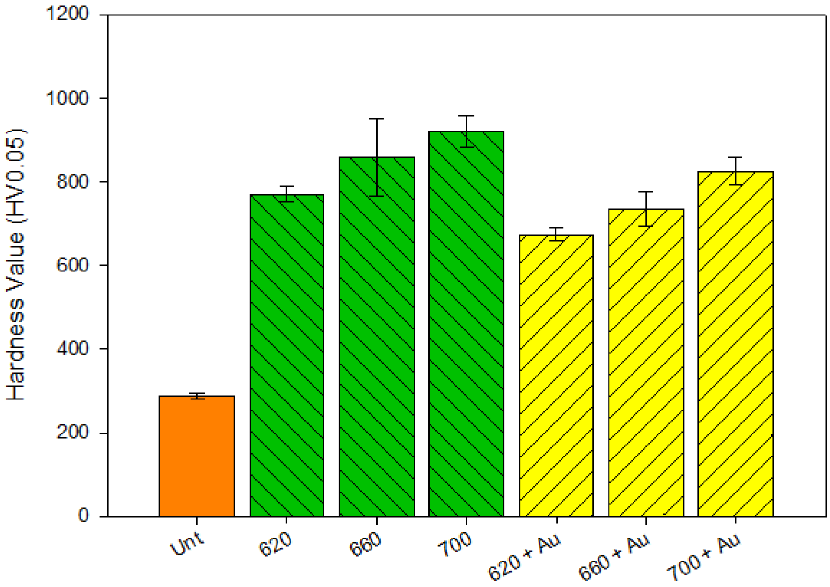

Figure 4.40: Surface micro-hardness of Ti67 untreated, C2T, and C3T Au. Treatment conditions are of 620, 660, or 700 °C, for 80 h.

The average surface micro-hardness values for the Ti64 Ag/Pd C3T 660 samples are shown in figure 4.41. *, **, and brackets denote $p > .05$, and therefore no statistically significant change taking place. Layer thickness has been plotted over the chart to allow quick comparison.

In general, increasing treatment duration results in an increased hardness value, where 1 h resulted in $\approx$ 710, and 80 h $\approx$ 1050 HV0.025 (a 1.5 times increase). However, for the 5 h treatment this was not the case. This condition resulted in a significantly ($p < .05$) higher hardness (1130 HV0.025) compared with the other treatments. In addition to the large increase in layer thickness between 1 and 5 h, this may have also been caused by the surface changes shown in figure 4.8, where it can be seen that for treatments 10-80 h the formed surface agglomerates begin to coalesce into larger ones, and the associated surrounding morphology changes.

Interestingly, the increase between 20, 40, and 60 h did not result in a significant ($p > .05$) change in hardness value, despite the thickness of the layer increasing over this range. This means that the change is likely due to micro-structural/compositional changes rather than due to the result being influenced by the underlying bulk material as may have occurred with the treatments between 1 and 10 h which produced a thinner layer.

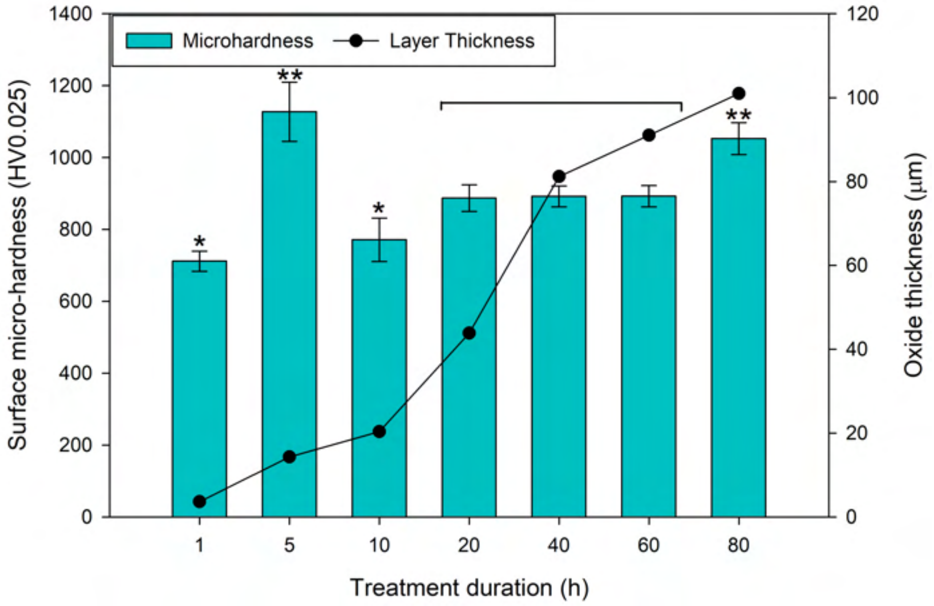

Figure 4.41: Surface Vickers micro-hardness (25 g) of the Ti64 C3T Ag/Pd 660 treated samples with varying treatment duration (1-80 h). *, **, and brackets denote $p > .05$. Oxide thickness is also plotted for each treatment for quick comparison.

Table 4.1: Surface micro-hardness at 25 and 50 g results of Ti64 660 5 h; C2T, C3T Ag, C3T Pd, and C3T Ag/Pd.

Treatment - 660 5h	HV0.025	HV0.05
C2T	931 +/- 20	612 +/- 34
C3T Ag	1067 +/- 72	720 +/- 52
C3T Pd	1099 +/- 68	686 +/- 96
C3T Ag/Pd	1128 +/- 82	853 +/- 51

Surface micro-hardness was measured at both 25 and 50 g for Ti64 C2T and C3T Ag, Pd, and Ag/Pd, treated at 660 °C for 5 h. The results from this can be seen in table 4.1.

It can be seen that the pre-deposition of catalytic elements yielded surface layers of higher surface micro-hardness than without, regardless of measurement load. This is especially true of Ag/Pd, which was ≈ 18 % harder than Ag and Pd at 50 g, and 4 % harder at 25 g. Ag and Pd demonstrated a similar surface micro-hardness, regardless of measurement load.

4.3.1.2 Load bearing capacity

The ability of the currently adopted C2T treatment of 620 °C for 80 h to maintain its hardness value with increasing load (load bearing capacity) has been compared with C3T Ag/Pd treated at 660 °C for 80 h in figure 4.42.

C3T Ag/Pd demonstrated a steady decline in hardness value with increasing load, with a drop over the load range of 27 %. Contrasting with this, C2T presented a very sudden drop in hardness value after only a slight increase in load. Increasing load further resulted in a drop in hardness to that of the bulk material underlying the surface layer, providing only 61 % of the initial hardness value. This signifies the superior ability of

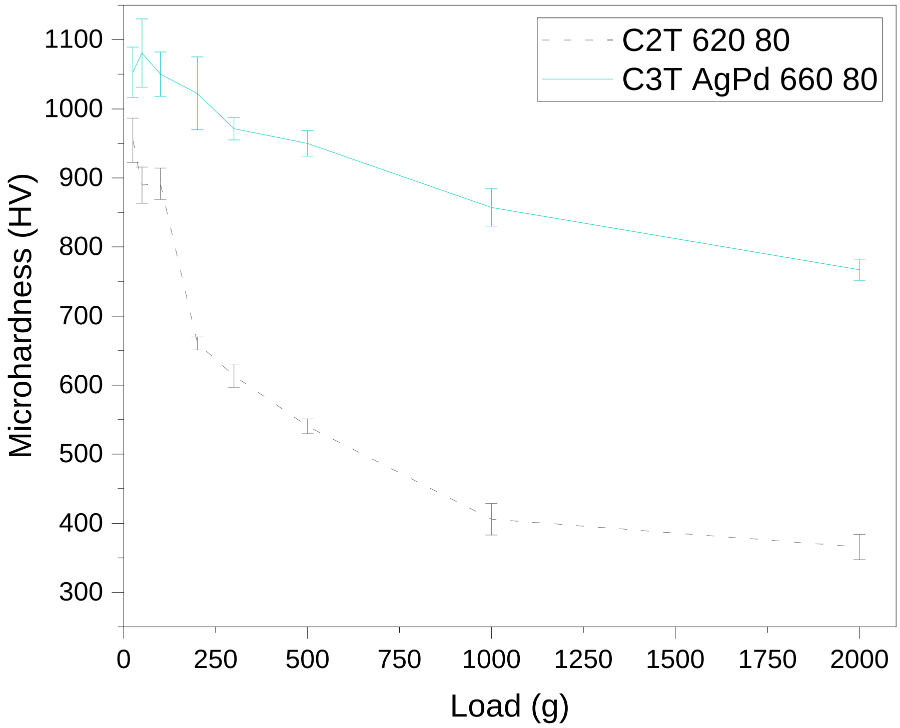

Figure 4.42: Load bearing capacity of Ti64 C2T 620 80 and C3T Ag/Pd 660 80 treated sample.

C3T Ag/Pd to support higher loads than the currently adopted C2T treatment.

4.3.1.3 Cross-sectional Hardness

The cross-sectional hardness values can be seen in figure 4.43. Please note, the measurements are from the area just beneath the surface layer, in the bulk material. Measurement was started as close to the surface layer as possible without causing the layer to break off due to it not being supported adequately by the bakelite mounting material. Optimal treatments were selected for the measurements.

As expected, untreated samples demonstrated a relatively constant hardness value with increasing depth. On the other hand, the treatments resulted in a significant increase in measured hardness close to the surface. This is due to oxygen diffusion into the bulk material beneath the surface layer forming the ODZ, and the associated interstitial hardening effect of this. Owing to the diffusion nature of this process, this value reduced with increasing depth.

It can be seen that C2T treated at both 620 and 660 resulted in a much higher initial hardness value compared with C3T, regardless of what catalytic element/s were used. This suggests that the nature in which the C3T surface layer was formed was more dominated by outward diffusion of titanium than inward diffusion of oxygen when compared with C2T.

Compared to C3T Au 620, both C3T Ag/Pd 620 and 660 treatments resulted in a much harder initial hardness. This suggests that a greater catalytic effect from the Ag/Pd resulting in more inward diffusion than Au.

In addition, both C3T Ag/Pd treatments allowed measurements to be taken much closer to the surface layer than both C2T and C3T Au treatments, owing to the much thicker layer present providing more support for the indent thus preventing spallation

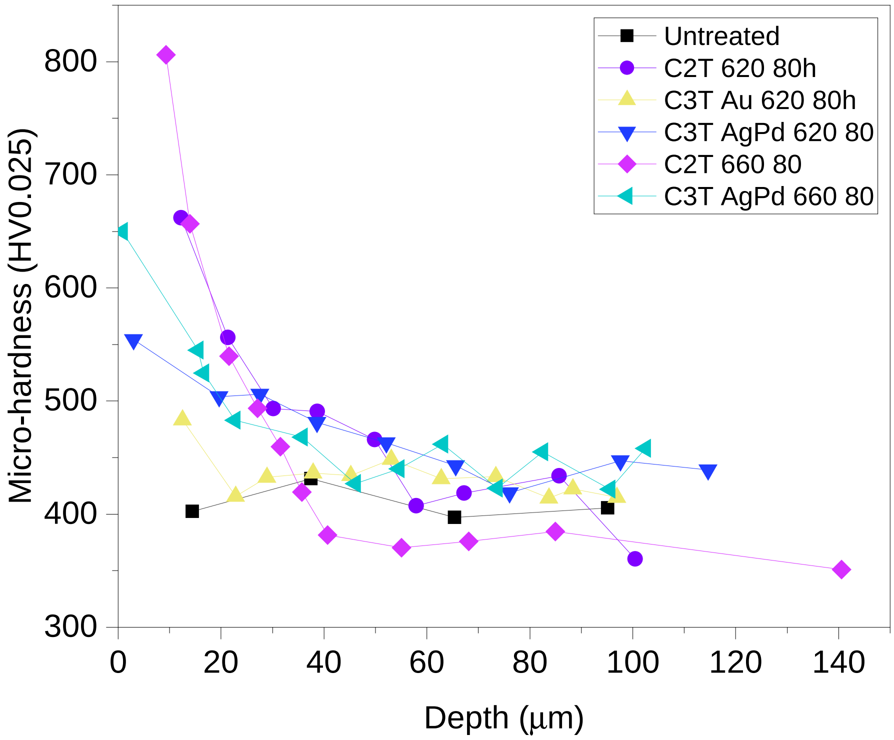

Figure 4.43: Cross-sectional Vickers micro-hardness (25 g) within the region beneath the surface layer of Ti64 untreated, C2T 620, C3T Au 620, C3T Ag/Pd 620, C2T 660, and C3T Ag/Pd 660, all treatments are for 80 hours.

during indentation.

Cross-sectional micro-hardness for Ti67 untreated, C2T, and C3T Au treated at either 620, 660, or 700 for 80 hours is plotted in figure 4.44. The measurements could not be taken too closely to the surface layer as this results in the layer spallating and therefore providing an incorrect hardness measurement. This means that all of the treated sample profiles were only considering the effect of CCT on the underlying substrate.

The untreated Ti67 presenting a relatively constant hardness value with increasing depth, as expected. In contrast, the treatments of Ti67 all resulted in a significantly increased initial hardness value due to nature of the treatment resulting in oxygen inward diffusion to form the ODZ, as with Ti64.

For both C2T and C3T, increasing treatment temperature resulted in a much higher initial hardness value, which is due to the higher diffusivity at the higher temperatures.

Comparing C2T with C3T Au, it can be seen that the C3T Au resulted in a much lower initial hardness value. This is potentially due to the mechanism in which the catalytic layer functions, resulting in relatively more outward diffusion to meet the oxygen rather than inward diffusion of oxygen compared with C2T.

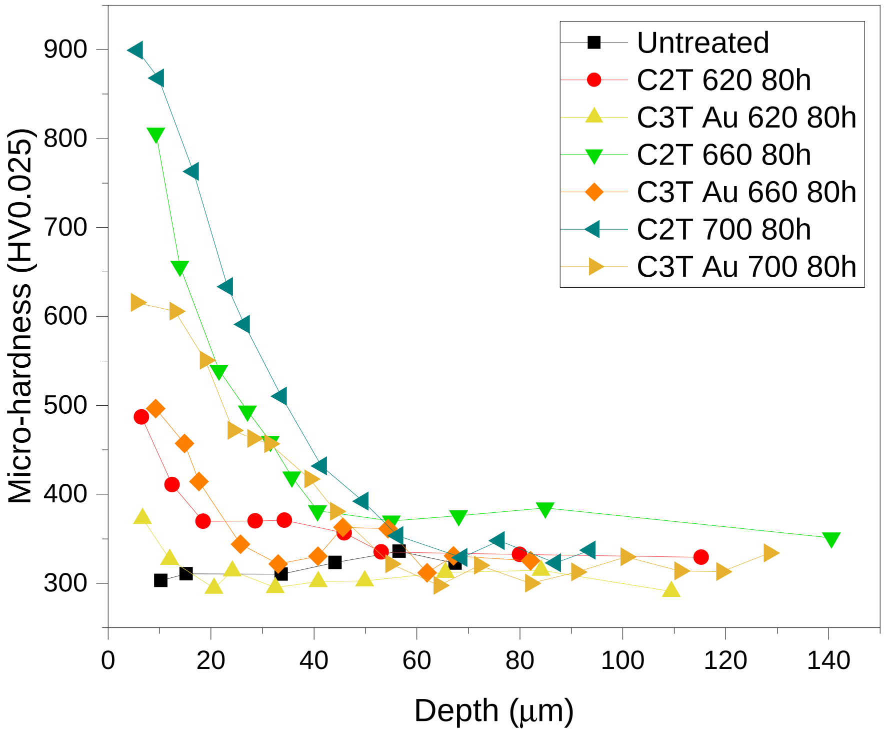

Figure 4.44: Cross-sectional Vickers micro-hardness (25 g) within the region beneath the surface layer of Ti67 untreated, C2T and C3T Au treated at either 620, 660, or 700 for 80 hours.

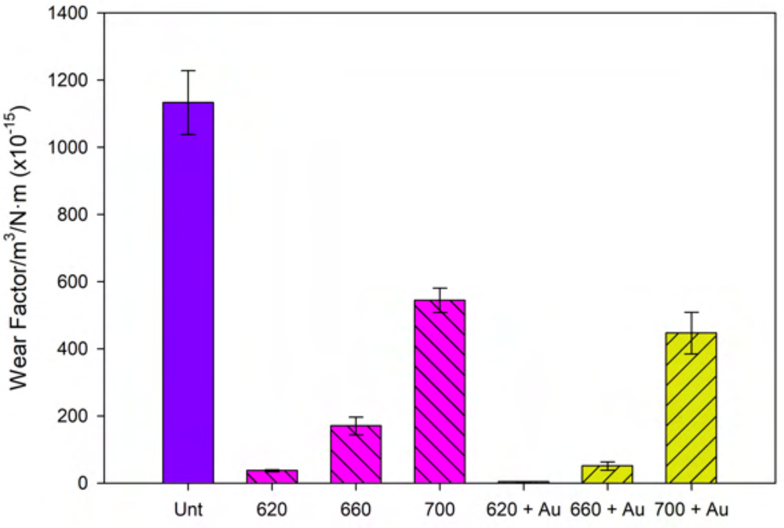

Figure 4.45: Wear factor after tribological testing at 15 N for Ti64 untreated, C2T, and C3T Au. Treatment conditions were 620, 660, 700 °C, all for 80 h.

4.3.2 Tribological Performance

The results shown in figure 4.45 display the wear factor of Ti64 untreated, C2T, and C3T Au samples. Untreated samples demonstrated the highest wear factor of $1133\times10^{-15} \pm 95\times10^{-15}$ mm^3/Nm.

CCT reduced the wear rate for all treatments. For the same CCT temperature, Au pre-deposition significantly reduced the wear factor of $37\times10^{-15} \pm 3\times10^{-15}$ versus $3\times10^{-15} \pm 0.7\times10^{-15}$; $170\times10^{-15} \pm 26\times10^{-15}$ versus $51\times10^{-15} \pm 12\times10^{-15}$; $544\times10^{-15} \pm 36\times10^{-15}$ versus $446\times10^{-15} \pm 62\times10^{-15}$, for 620; 660; 700, respectively. When increasing CCT temperature it can be seen that the wear factor increased for both C2T and C3T Au, which suggests that increasing treatment temperature results in a poorer surface layer quality (as evidenced in figure 4.6) which is not as durable.

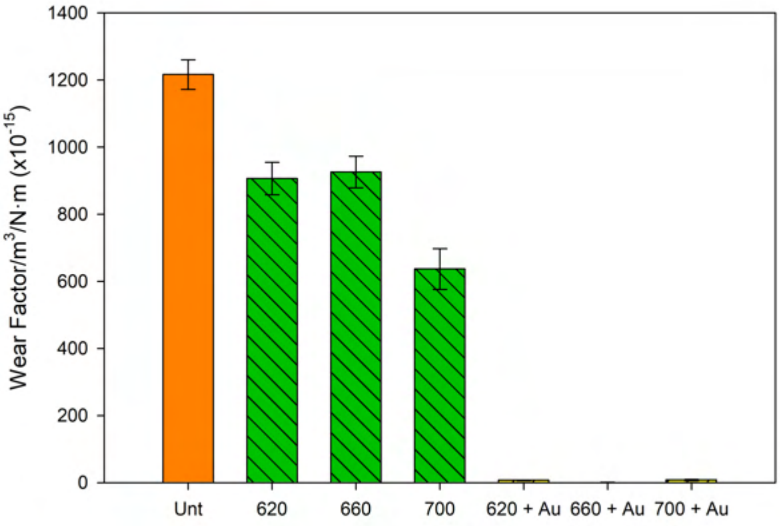

Figure 4.46: Wear factor after tribological testing at 15 N for Ti67 untreated, C2T, and C3T Au. Treatment conditions were 620, 660, 700 °C, all for 80 h.

The results shown in figure 4.46 display the wear factor of Ti67 untreated, C2T, and C3T Au samples. Untreated samples demonstrated the highest wear factor of $1263\times10^{-15} \pm 44\times10^{-15}$ mm^3/Nm.

Although CCT reduced the wear rate for all treatments, it can be seen that C2T only resulted in a marginal decrease in wear factor, suggesting either a poor or thin surface layer, as once the hard layer is worn through severe abrasive wear will occur. Increasing treatment temperature resulted in a slight improvement in wear factor, although not significantly so.

Au pre-deposition significantly reduced the wear factor irrespective of treatment temperature, where a maximum reduction of 99.9 % versus untreated and C2T occurred.

The wear factor results from tribological testing at 15 and 50 N for Ti64 untreated, C2T 620 80 h, and C3T Ag/Pd 660 1, 5, 20, 20 post surface grinding, and 80 h are shown in figure 4.47. Surface grinding (sample code 20G) was carried out to remove the top-most surface containing the agglomerated structures.

At 15 N, C2T 620 80 h resulted in a significant reduction in wear factor compared with untreated, of 1133x10^{-15} ± 95x10^{-15} versus 37x10^{-15} ± 2x10^{-15} m^3/N·m respectively. C3T Ag/Pd tribological testing at this load resulted in unmeasurable wear scars.

Increasing the load to 50 N resulted in C2T demonstrating a slight reduction in wear factor of 364x10^{-15} ± 32x10^{-15} versus the 394x10-15 ± 86x10-15 m^3/N·m of untreated. When comparing the wear factor values between 15 and 50 N, it can be seen that untreated is significantly lower at the higher load, and C2T 620 80 h is significantly higher. This may be attributed to the untreated sample conforming to the counterpart thus reducing the contact pressure, and the C2T sample presenting severe abrasive wear of the underlying bulk material once the surface layer was worn though, evidenced in figure 4.49.

The higher load resulted in marginally measurable wear scars for C3T Ag/Pd. The resulting wear factor was significantly reduced when compared to both untreated and C2T. No significant difference can be seen between 1 and 20 h treated samples, 5x10^{-15} ± 1x10^{-15} versus 6x10^{-15} ± 2x10^{-15}, respectively. Interestingly, the 5 h treated sample demonstrated a much higher wear factor (33x10^{-15} ± 8x10^{-15}). This may be attributed to a change in surface layer structure (figure 4.8) and this surface having a higher hardness (figure 4.41) resulting in harder wear particles being produced, and therefore relatively (compared with the other C3T Ag/Pd treatments) more abrasive wear occurring due to these harder third-bodies. Increasing treatment duration to 80 h resulted in a significant

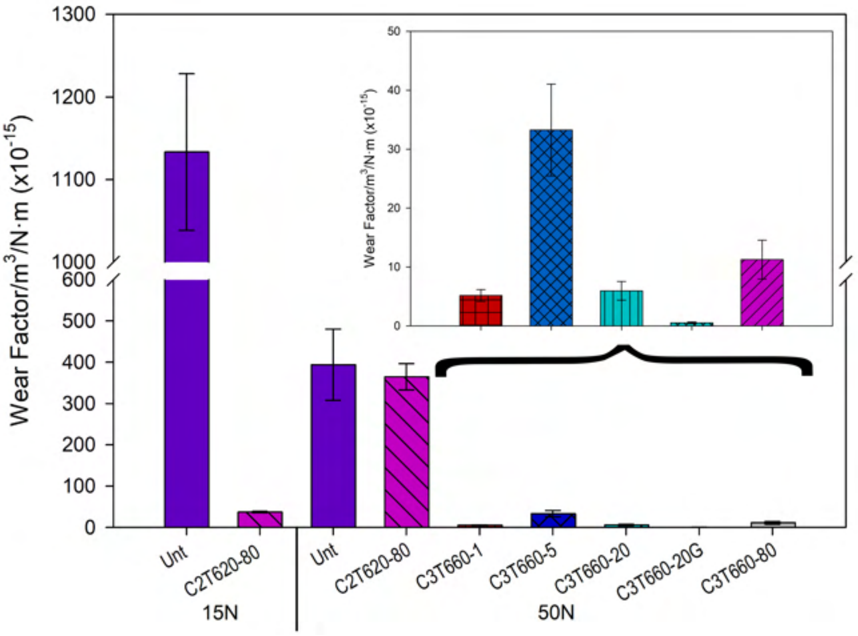

Figure 4.47: Wear factor after tribological testing at 15 and 50 N for Ti64 untreated, C2T 620 80, and C3T Ag/Pd 660 1, 5, 20, 20 post surface grinding, and 80 h. Please note label for testing load beneath the x-axis. An additional graph for C3T Ag/Pd plotting the same data has been overlaid to allow easier comparison.

increase in wear factor compared with the 1 and 20 h samples of 11x10^{-15} ± 3x10^{-15} versus ≈ 5.5x10^{-15}, respectively. Although this is much less significantly than the 5 h.

Additionally, it can be seen that the removal of the top-most layer (C3T Ag/Pd 660 20 G) resulted in a significant reduction in wear factor, where hardly any measurable wear was seen (0.52x10^{-15} ± 0.14x10^{-15}). Further investigation was carried out to try and ascertain why this occurred, which can be seen in figure 4.48 and table 4.2.

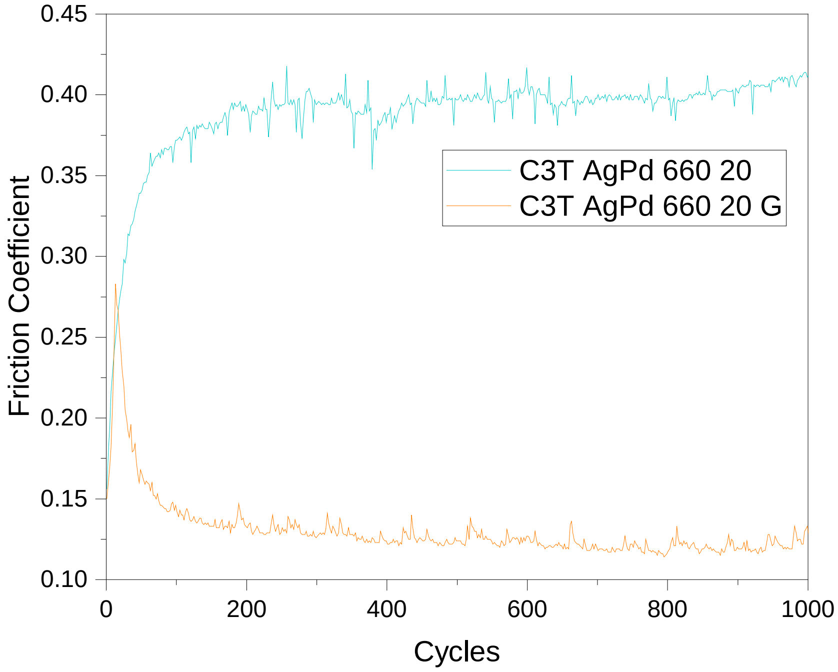

Figure 4.48: Measured friction coefficient during tribological testing 50 N for Ti64 C3T Ag/Pd 660 20 h and 20 h post surface grinding.

After a bedding in period, it can be seen that the recorded coefficient of friction (figure 4.48) was significantly lower for the ground sample with average values of 0.124 ± 0.006 versus 0.397 ± 0.008 respectively. This is likely caused by the significant reduction in the measured surface roughness (table 4.2) of 0.23 versus 0.85 μm. This is due to the grinding process removing the surface features present pre-grinding.

Table 4.2: Surface roughness of Ti64 C3T Ag/Pd treated at 660 C for 20 h, pre- and post- surface grinding at P1200.

Treatment Condition	Surface Roughness (Ra) (μm)
C3T Ag/Pd 660 20 h	0.852 ± 0.162
C3T Ag/Pd 660 20 h G	0.227 ± 0.078

Surface profiles of the wear tracks and surrounding area of Ti64 untreated, C2T 620 80 h, and C3T Ag/Pd 660 20 h post 50 N tribological testing can be seen in figure 4.49. Untreated and C2T had similar track depths of $\approx$ 30 μm. However, it can be seen that their wear mechanism was not the same. The untreated sample's wear track was much smoother than that of C2T 620 80 h, where deep gouges can be seen suggesting severe abrasive wear. This has likely occurred due to abrasive wear debris being generated from the hard oxide layer wearing through, and these acting as third-bodies to abrade deep into the bulk material underneath, thus causing rapid wear.

Compared to this, C3T Ag/Pd 20 h had a smooth and much shallower track, where the depth does not exceed that of the surface profile roughness surrounding the wear track, i.e. it has just polished the surface. This suggests that the counterpart was not able to wear through the subsurface under the tribo test conditions.

SEM images of some typical wear tracks post-tribological testing can be seen in figures 4.50 and 4.51 for Ti64 and figure 4.53 for Ti67. It can be seen that there are multiple mechanisms in which wear has occurred. These are: 1 adhesive wear, where large asperities can be seen due to plastic deformation and adhesion junctions forming between the counterpart and sample surface. In addition, gouging can be seen due to wear debris

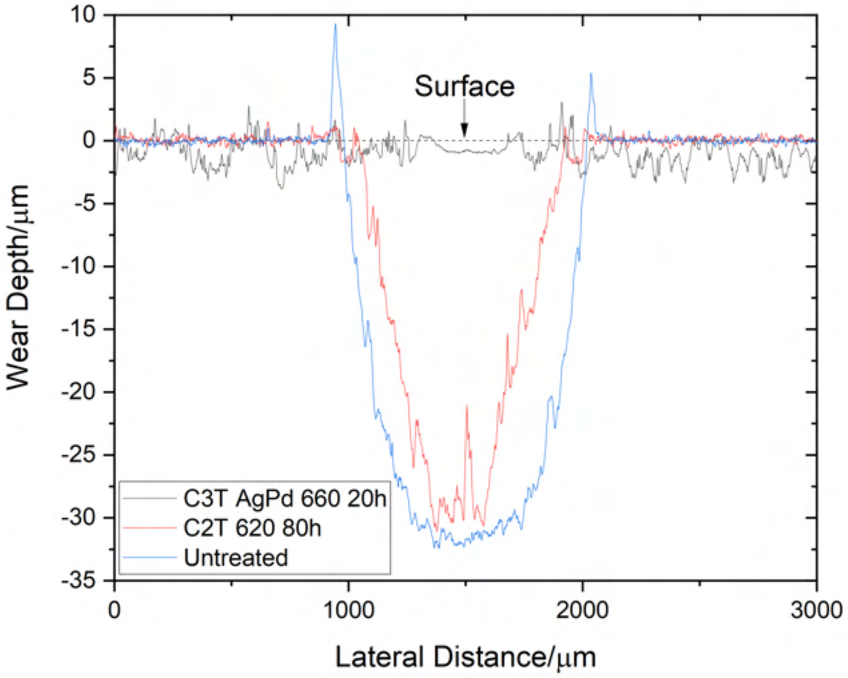

Figure 4.49: Surface profiles of Ti64 untreated, C2T 620 80h, and C3T Ag/Pd 660 20 wear tracks post wear testing at 50 N.

causing abrasive wear; 2 abrasive wear due to the hard wear debris acting as a third-body, which has worn through the oxide layer and into the underlying bulk material; 3 partial oxide layer spallation/chip-off; 4 further layer spallation/chip-off; 5 severe surface layer spallation/chip-off and wear of the underlying bulk material; 6 a polished smooth track rather than wear. Untreated for both alloys (figure 4.50(a) and 4.53(a)) demonstrated severe type 1 wear.

For Ti64, C2T 620 demonstrated type 3 wear, where surface layer peeling can be seen in figure 4.50(b). Increasing treatment temperature to 660 (figure 4.50(d)) proved detrimental to the tribological performance, where severe spallation (type 5) has occurred. Changing alloy to Ti67 showed that the wear mechanism changed to abrasive/adhesive wear (figures 4.53(b) and (d)) due to the hard wear debris wearing through the relatively thin oxide layer (figure 4.35). The higher temperature presented a narrower wear track, and hence a reduced wear factor (figure 4.46).

Regardless of alloy, the addition of catalytic films typically resulted in just type 6 (polished surface) wear, other than for Ti64 C3T Au 700 (figure 4.50(e)) which presented type 3 (surface chip-off) wear. The wear track produced on Ti64 C3T Ag/Pd 660 20 h G (figure 4.51) presented a polished surface which demonstrated peeling/spallation. This suggests the presence of a weakly bound tribo-film on this track. Deeper analysis of this track can be seen in figure 4.52 and table 4.3. Figure 4.52(b-c) present higher magnification regions from (a). When comparing spectrum data from SP1, SP2, and SP3 (table 4.3), it can be seen that the polished film on the surface with which SP2 contains presents relatively high wt% of W, and an increased wt% of O. This suggests the presence of a tungsten oxide due to the WC counterpart wearing and the resultant debris from this oxidising to produce a tribo-film. This tribo-film had weak bonding to the sample surface and therefore was prone to spallation, evidenced by the film peeling in figure 4.51. The film containing tungsten oxide is evidenced further by the wt% of the other elements being similar within SP1 and SP3, but reduced within SP2.

Following from this, the main wear mechanism which occurred during each tribological test have been summarised in table 4.4. It can be seen that for both Ti64 and Ti67 untreated samples adhesive wear took place due to substrate-counterpart galling.

Comparing C2T Ti64 and Ti67, it can be seen that Ti64 produced a layer prone to spallation, which results in severe wear, whereas Ti67 is more prone to just abrasive wear due to the hard debris from the layer producing third-body wear. It is likely that this occurred because the layer produced on Ti64 is much thicker than that on Ti67 (figure 4.34 vs 4.35), and them typically presenting poor layer bonding (figure 4.6 e and g).

Regardless of alloy, C3T produced layers which were typically only polished by the counterpart material, under the testing conditions. This shows that the layers produced by C3T were of much higher durability compared with the currently adopted treatment (C2T).

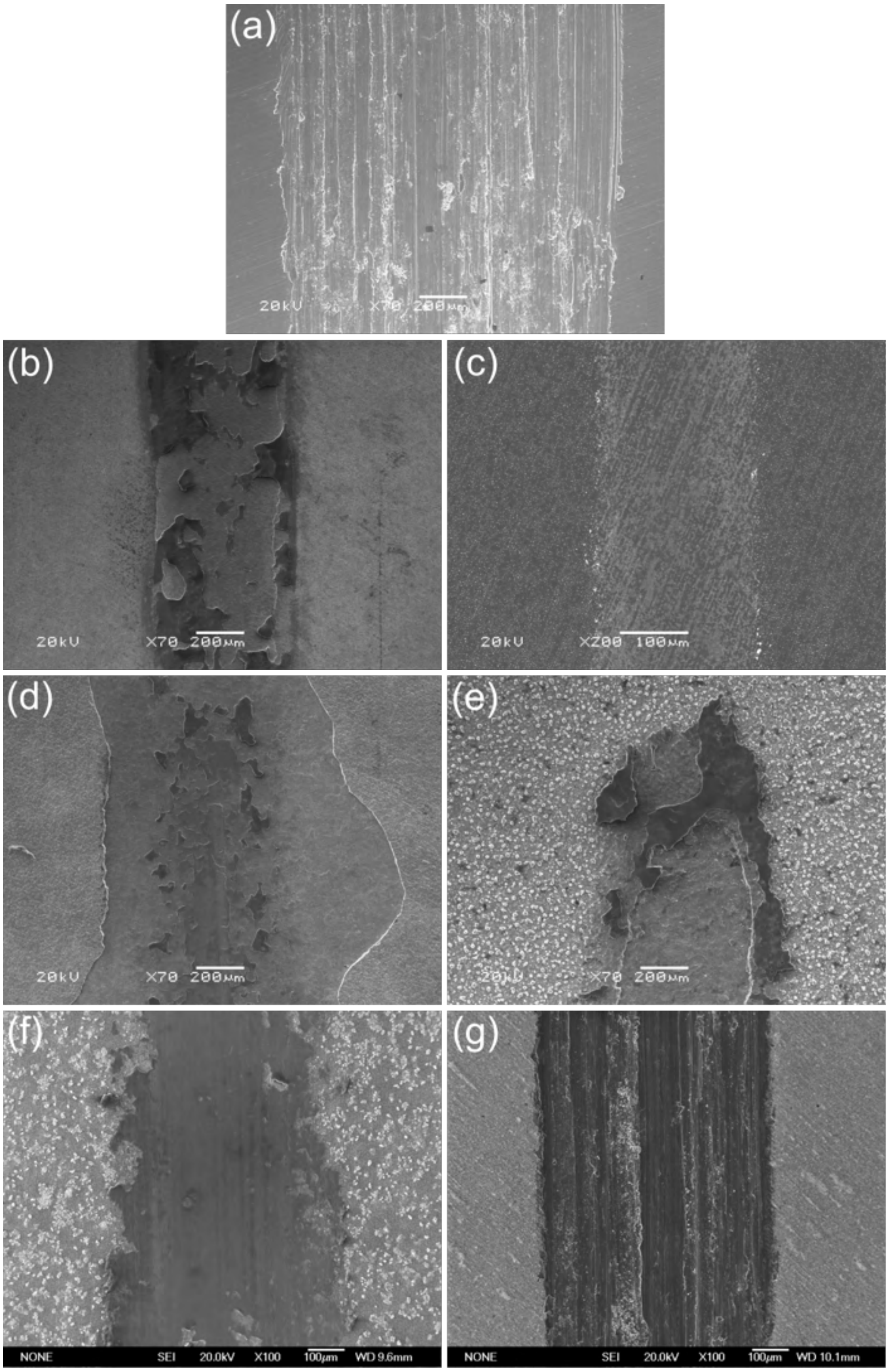

Figure 4.50: SEM images of the wear scars produced during tribological testing of Ti64 untreated, C2T, C3T Au, and C3T Ag/Pd. Where (a) untreated, (b) C2T 620 80 h, (c) C3T Au 620 80 h, (d) C2T 660 80 h, (e) C3T Au 660 80 h, (f) C3T Ag/Pd 660 1 h, and (g) C3T Ag/Pd 660 20 h. (a-e) are tested at 15 N, and (f,g) at 50 N.

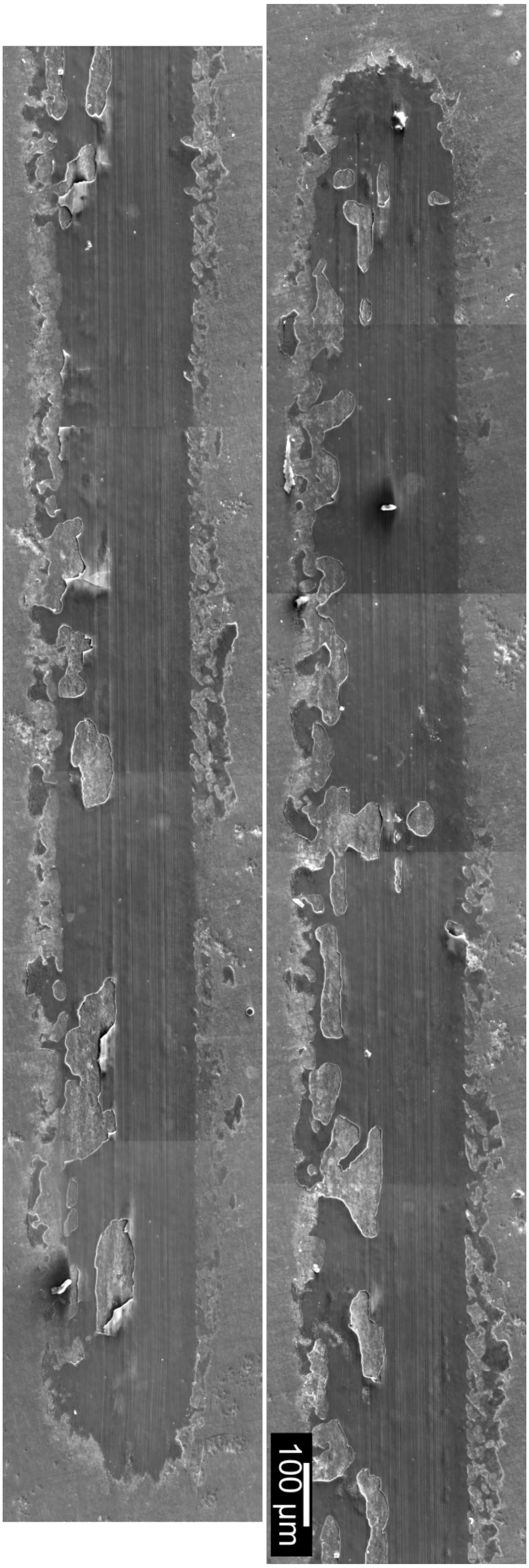

Figure 4.51: SEM image of a wear scars produced during tribological testing at 50 N of Ti64 C3T Ag/Pd 660 20 h G. Magnification is the same across all of the collective images to produce the full scar.

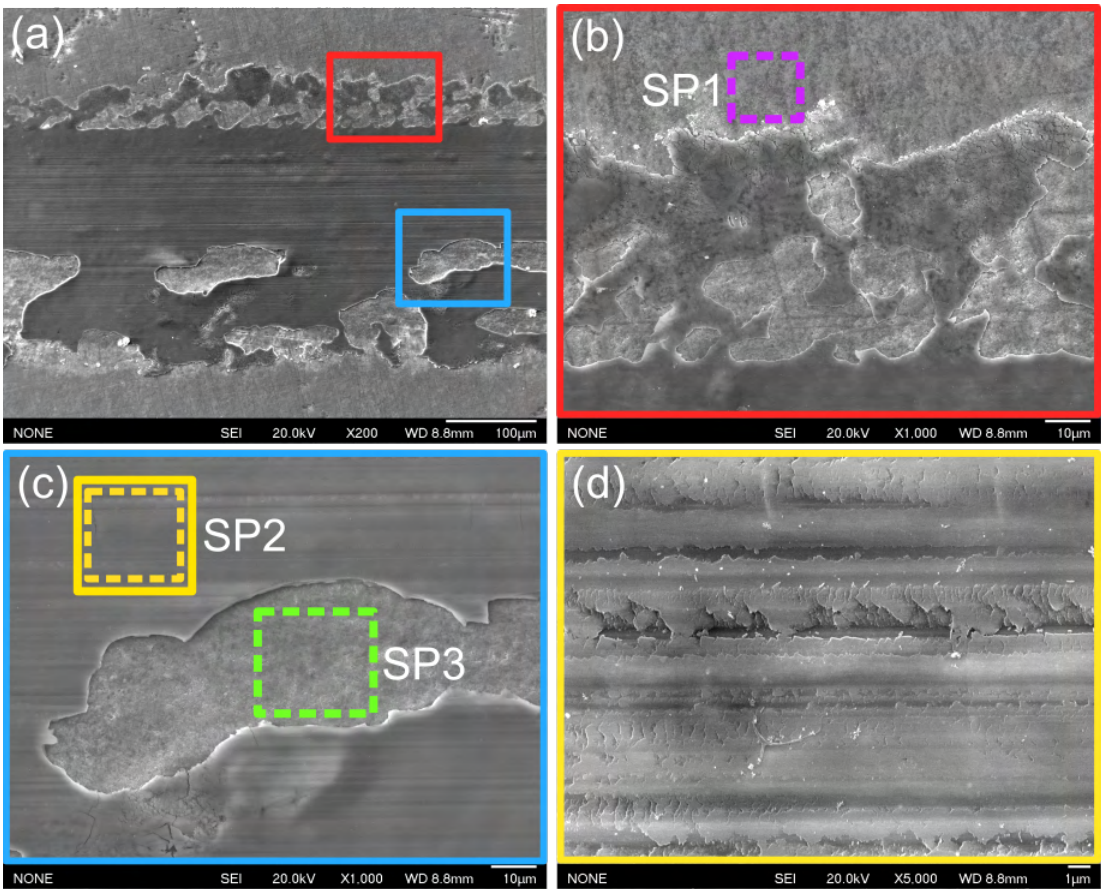

Figure 4.52: SEM images of different regions within a wear scar produced during tribological testing at 50 N of Ti64 C3T Ag/Pd 660 20 h G. Boxes with solid lines of the same colour indicate a magnification, where the red box in image (a) is magnified in (b), the blue box in (a) is magnified in (c), and the yellow box in (c) is magnified in (d). Dashed boxes in (b) and (c) indicate where EDX spectrums were measured (SP1, SP2, and SP3), the spectrum data from these regions are displayed in table 4.3.

Table 4.3: Table of the EDX spectrum data from the Ti64 C3T Ag/Pd 660 20 h G wear track worn at 50 N. SP1, 2, and 3 are from the regions shown in figure 4.52.

Element, wt%	SP1	SP2	SP3
Ti	51.58	43.45	49.72
Al	9.48	7.90	10.85
V	2.46	2.44	3.42
Ag	1.54	1.39	1.5
Pd	0.12	0.05	0
O	34.81	39.65	34.37
W	0	4.73	0.13

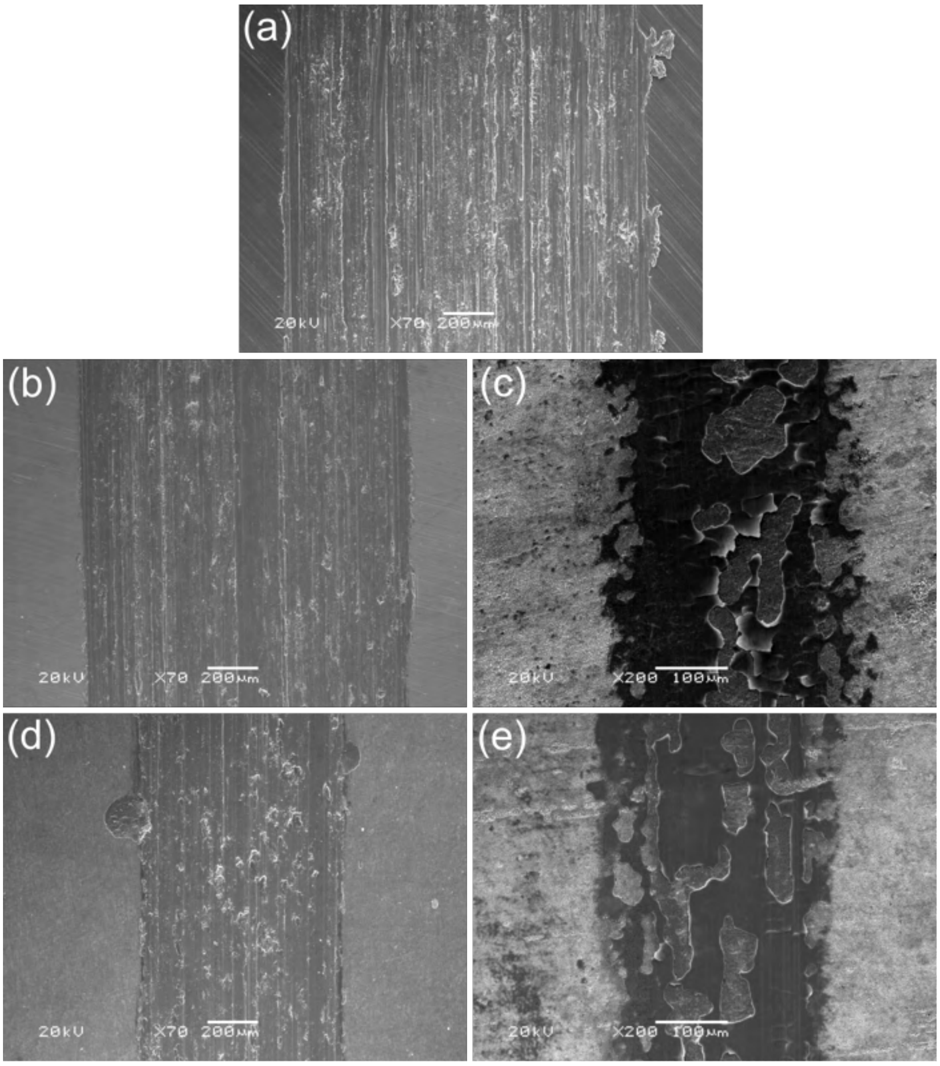

Figure 4.53: SEM images of the wear scars produced during tribological testing at 15 N of Ti67 untreated, C2T, and C3T Au. Treatments were either 620 or 700 C for 80 h. Where (a) untreated, (b) C2T 620, (c) C3T Au 620, (d) C2T 660, (e) C3T Au 660.

Table 4.4: Table of the dominant wear mechanism for each tribological test of untreated, C2T, and C3T Ti64 and Ti67 samples.

Sample Condition	Dominant Wear Mechanism
Ti64 Untreated	Adhesive (figure 50(a))
Ti64 C2T 620 80 h	Oxide Slight Spallation (figure 50(b))
Ti64 C2T 660 80 h	Oxide Spallation (figure 50(d))
Ti64 C2T 700 80 h	Oxide Severe Spallation
Ti64 C3T Au 620 80 h	Oxide Polish (figure 50(c))
Ti64 C3T Au 660 80 h	Oxide Slight Spallation (figure 50(e))
Ti64 C3T Au 700 80 h	Oxide Spallation
Ti64 C3T Ag/Pd 660 1 h	Oxide Polish (figure 50(f))
Ti64 C3T Ag/Pd 660 5 h	Oxide Polish
Ti64 C3T Ag/Pd 660 20 h	Oxide Polish (figure 50(g))
Ti64 C3T Ag/Pd 660 20 h G	Oxide Polish (figure 51)
Ti64 C3T Ag/Pd 660 80 h	Oxide Polish
Ti67 Untreated	Adhesive (figure 53(a))
Ti67 C2T 620 80 h	Oxide Abrasive (figure 53(b))
Ti67 C2T 660 80 h	Oxide Abrasive (figure 53(d))
Ti67 C2T 700 80 h	Oxide Abrasive
Ti67 C3T Au 620 80 h	Oxide Polish (figure 53(c))
Ti67 C3T Au 660 80 h	Oxide Polish (figure 53(e))
Ti67 C3T Au 700 80 h	Oxide Polish

4.4 Surface Treated Bone Fixation Pin Performance

4.4.1 Ceramic Conversion Process

Due to concerns regarding the line-of-sight nature of the PVD process, and the relatively complex geometry of a fixation pin compared with a coupon sample, a sacrificial pin was used to PVD coat and treat at 660 for 5 h (C3T Ag/Pd 660 5 h). This was then characterised via SEM analysis. An image of the fluted region at the pin tip can be seen in figure 4.54. It can be seen that a thick surface layer was able to successfully grow around the edge of the fluted region. Although the layer was slightly thinner bordering

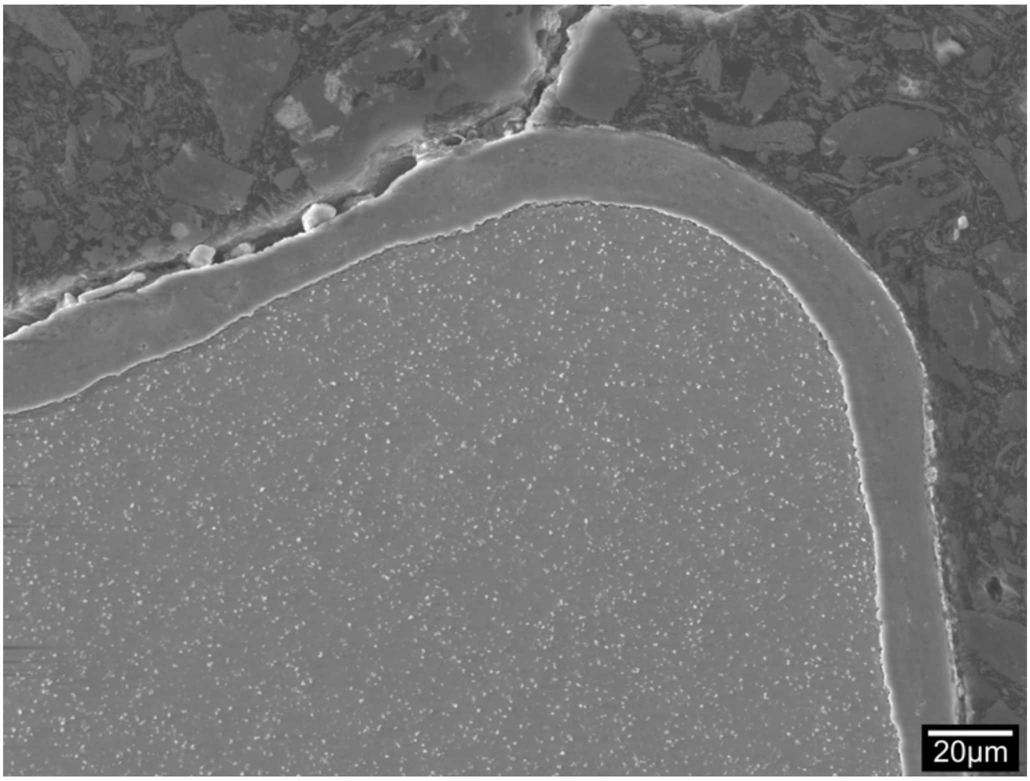

Figure 4.54: SEM cross-section image of a C3T Ag/Pd 660 5 h treated fixation pin at the edge of the fluted region.

the edge, potentially due to the PVD coating not being as thick in this region prior to treatment, it is still a thick and dense layer of approximately 12 μm versus the 16 μm in the other regions.

4.4.2 Fixation Pin Drilling

4.4.2.1 Force

The recorded axial forces, Fz, needed to achieve the insertion distance of 25 mm through the simulated bone plate against the insertion time are shown in figure 4.55 for as received (untreated) and C3T Ag/Pd 660 5 h pins. It can be seen that for the untreated pins the applied axial force increased linearly before it reached the maximum force value, then dropped to a nearly constant force, with some fluctuation as the pin went through the bone simulation block. Finally, it rapidly reduced before it flattened at a low value after the pin fully went through the simulated bone plates. Compared with the untreated pins, a significant reduction in the insertion force was observed for C3T treated pins. As can be seen from figure 4.56 that the average/maximum insertion forces are 20/33 N for the treated, and 78/86 N for the untreated, a nearly four times reduction in mean insertion force of the C3T pins versus the untreated pins.

These results demonstrate that the C3T Ag/Pd treatment has a great potential to reduce the wear of complex shaped components, meriting further systematic testing of fixation pins with different treatment parameters.

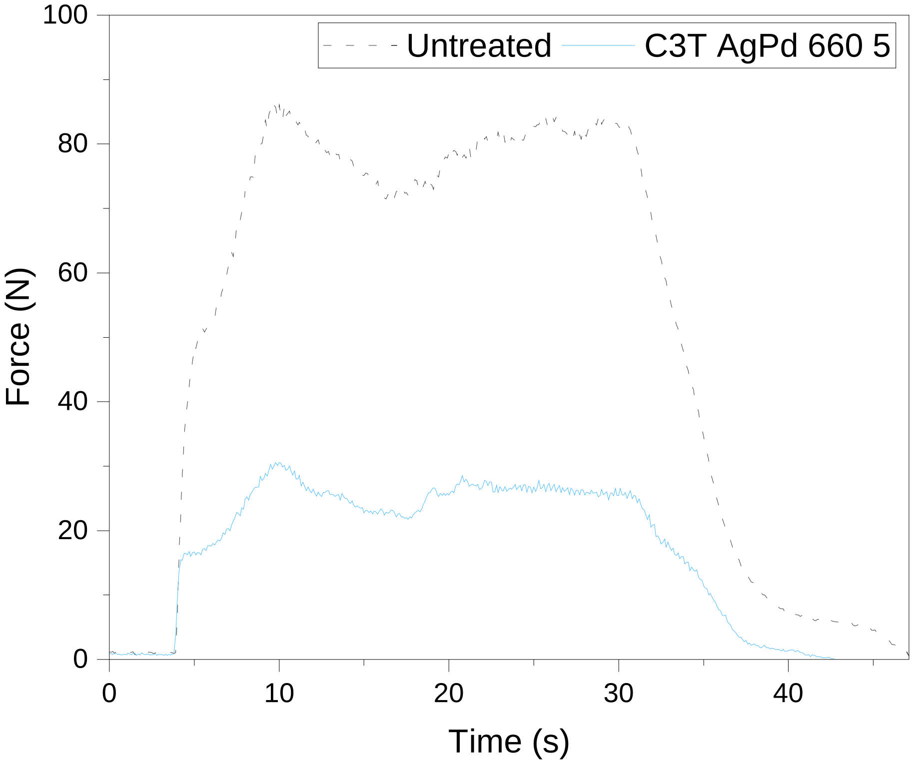

Figure 4.55: Axial force against time during the drilling of simulated bone with as-received (untreated) and C3T Ag/Pd treated at 660 °C for 5 h fixation pins.

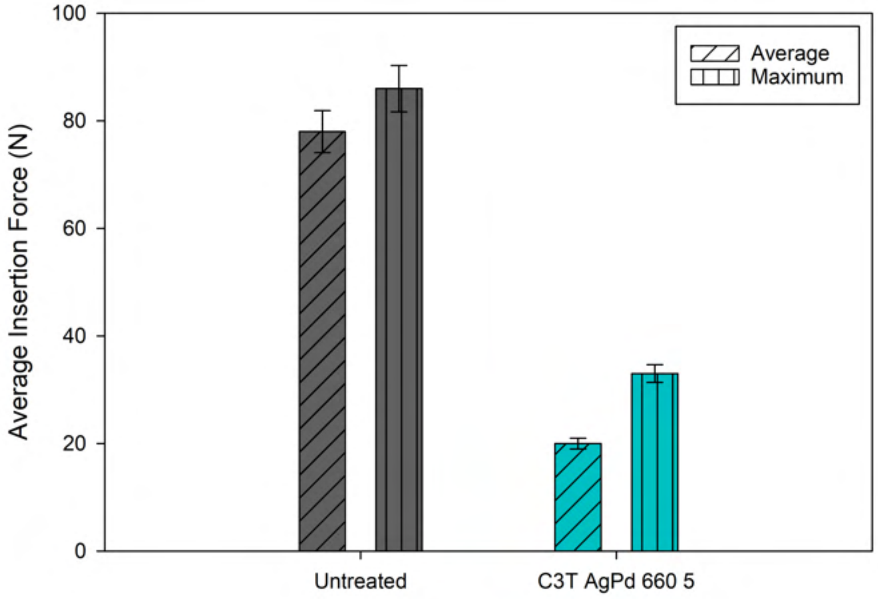

Figure 4.56: Chart of average and maximum insertion axial force during drilling of simulated bone with untreated and C3T Ag/Pd 660 5 h fixation pins.

Figure 4.57 shows the recorded axial force against time results of further systematic testing from figure 4.55 and 4.56. As-received (untreated), untreated but PVD coated with Ag/Pd, C2T 660 3 h, C2T 620 80 h, and C3T Ag/Pd 660 3 h were tested by drilling 25 mm into simulated bone blocks.

It can be seen that PVD coating resulted in a very marginal reduction in recorded axial force compared with untreated, likely induced by the solid-lubricating effect of the Ag/Pd coating.

Treatment at 660 for 3 h without the addition of the catalytic layer (C2T 660 3 h) resulted in a significant reduction in the required axial force to drill through the simulated bone compared with untreated and PVD coated pins. This reduction was not as significant as for C2T 620 80 h and C3T Ag/Pd 660 3 h, who demonstrated similar values.

It can also be seen that for untreated pins the last section of drilling tapered off before finally getting through the bone material, likely due to the cutting-edge blunting during the drilling process. This did not occur with the treated pins.

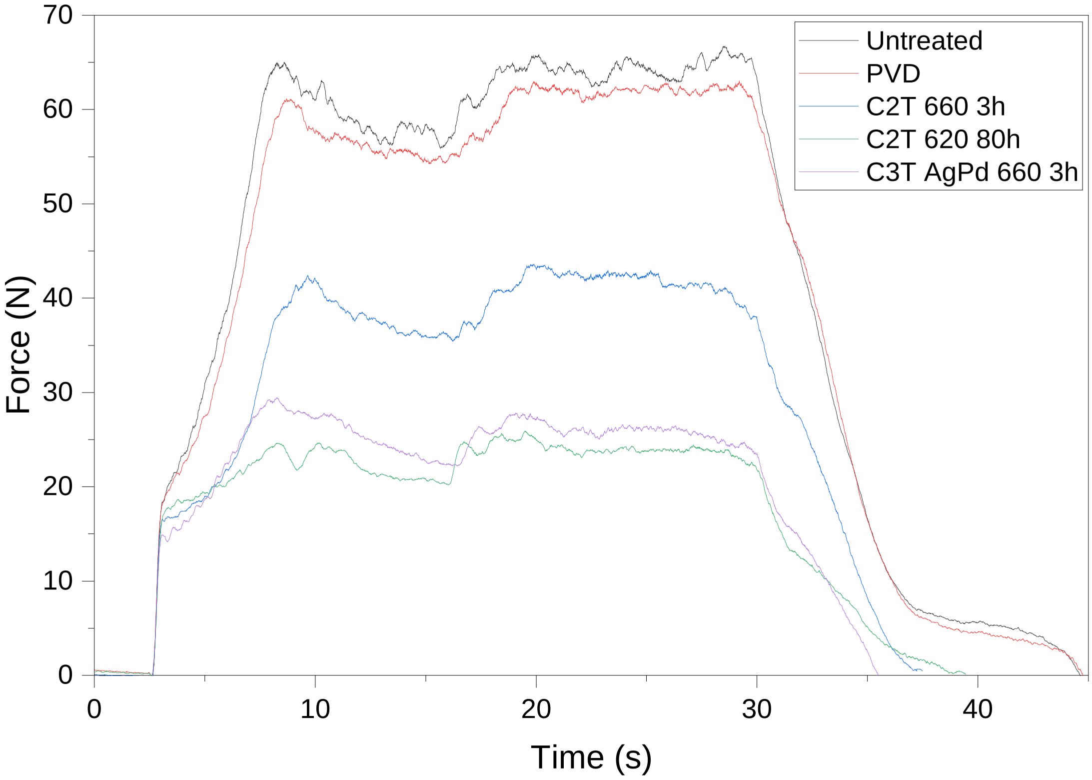

Figure 4.57: Axial force against time during the drilling of simulated bone with as-received (untreated), untreated but Ag/Pd coated (PVD), C2T treated at 660 for 3 h, C2T treated at 620 for 80 h, and C3T Ag/Pd treated at 660 for 3 h fixation pins.

Figure 4.58 charts the average and maximum insertion axial forces during the drilling process of the simulated bone material. Statistical analysis has been carried out on the data, and subsequently * and ** denote $p > .05$ for the average force values, and # and ## denote $p > .05$ for the maximum insertion force values.

It can be seen that the maximum insertion force value was higher than the respective average insertion force, suggesting that the drilling process is not a constant force as the fixation pin moves through the material.

As expected, the as-received but PVD coated fixation pin did not demonstrate a statistically ($p > .05$) significant change in average fixation pin insertion force, where the measured values were 58 ± 4 versus 58 ± 6 N, respectively.

The treatments for the fixation pins successfully significantly reduced the average insertion force required to drill through the simulated bone material. However, for C2T 660 3 h (38 ± 2 N) this was not as significantly reduced as compared with C2T 620 80 h and C3T Ag/Pd 660 3 h. But this was still a 34 % improvement compared with the untreated pins.

The C2T 620 80 h demonstrated a lower average insertion force of 24 ± 1 N compared with C3T 660 3 h's 28 ± 3 N. However, this was not a statistically significant ($p > .05$) reduction in force; indicating a potential for the observed change to be due to random sampling variability.

Although higher, the maximum insertion force required followed the same trend as the average.

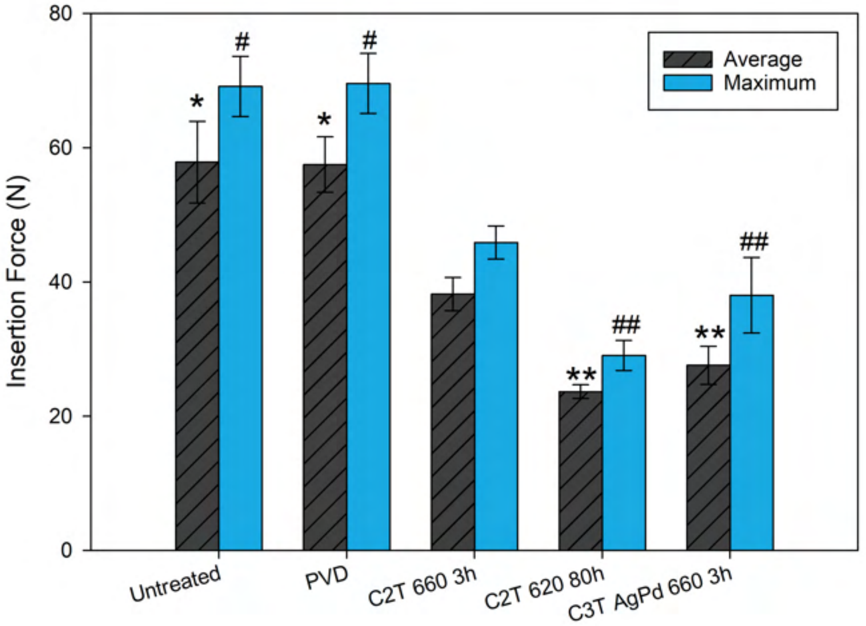

Figure 4.58: Chart of average and maximum insertion axial force during drilling of simulated bone for the different fixation pins. * and ** denote $p > .05$ for the average insertion force values. # and ## denote $p > .05$ for the maximum insertion force values.

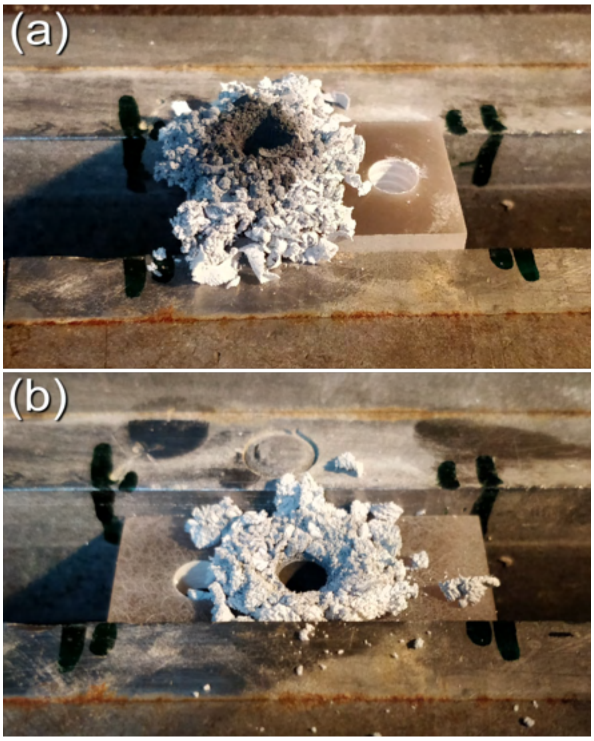

Figure 4.59: Images of the drilling debris, where (a) is for a untreated pin, and (b) is for a treated pin.

4.4.2.2 Temperature

Images of the extruded wear debris post-drilling can be seen in figure 4.59. The blackened debris seen from the untreated pins (figure 4.59(a)) is caused by the higher temperatures generated during drilling causing burning of the simulated bone material. It can be seen in 4.59(b) that the treated pins did not cause the debris to burn, suggesting the temperature generated was much lower than as untreated.

The recorded temperatures during drilling within the simulated bone and post drilling at the fixation pin tip can be seen in figure 4.60. Statistical analysis was carried out: * and ** denote $p > .05$ for the average bone temperature values; # and ## denote $p > .05$ for the average pin temperature values.

The pin temperatures were all significantly higher than for bone, due to both the thermal diffusivity of the bone and the fact that the thermocouple tip was not able to be placed directly next to the drilling hole.

It can be seen that for both bone and pin temperature all treatments were able to significantly ($p < .05$) reduce the recorded temperature. However, comparing between treatments no significant ($p > .05$) change in temperature was measured. The same is also true when comparing untreated and PVD coated pins.

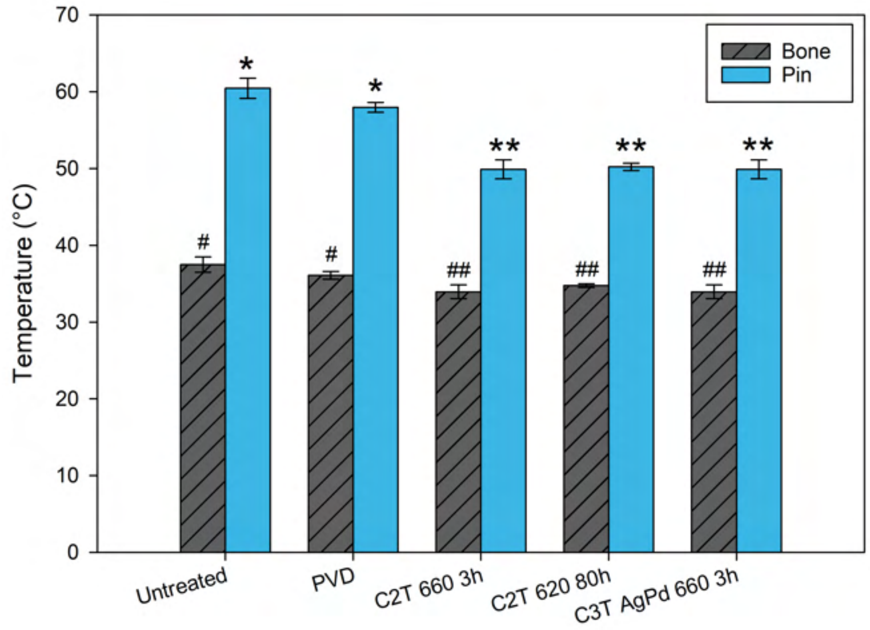

Figure 4.60: Chart of temperature during drilling of simulated bone recorded during drilling within the bone and at the tip of the pin post drilling for the different fixation pins. * and ** denote $p > .05$ for the average bone temperature values. # and ## denote $p > .05$ for the average pin temperature values.

4.4.2.3 Cutting surface wear

The cutting surface of the fixation pins post-drilling can be seen in figure 4.61. It can be seen that for both untreated (a) and untreated with PVD coating (b) severe wear of the cutting edge has occurred. This resulted in the sharp edge being completely rounded, and therefore will be much less able to drill through the bone block.

Although the treated pins demonstrated much less wear, the C2T 660 3 h treated pin (c) cutting edge experienced significant damage, where the treated layer has almost entirely been removed from the cutting edge, and the underlying bulk has had significant wear. Increasing the treatment time to 80 h (d) it can be seen that the amount of wear to the cutting edge has significantly reduced. However, it can also be seen that at the edge of the pin a large region of the surface layer has spallated off. This may have occurred due to poor surface layer bonding in this region coupled with significant shear forces during the drilling process.

C3T 660 3 h presented marginal wear at the cutting edge, demonstrating superior surface layer bonding and toughness, even with complex shapes such as a fixation pin.

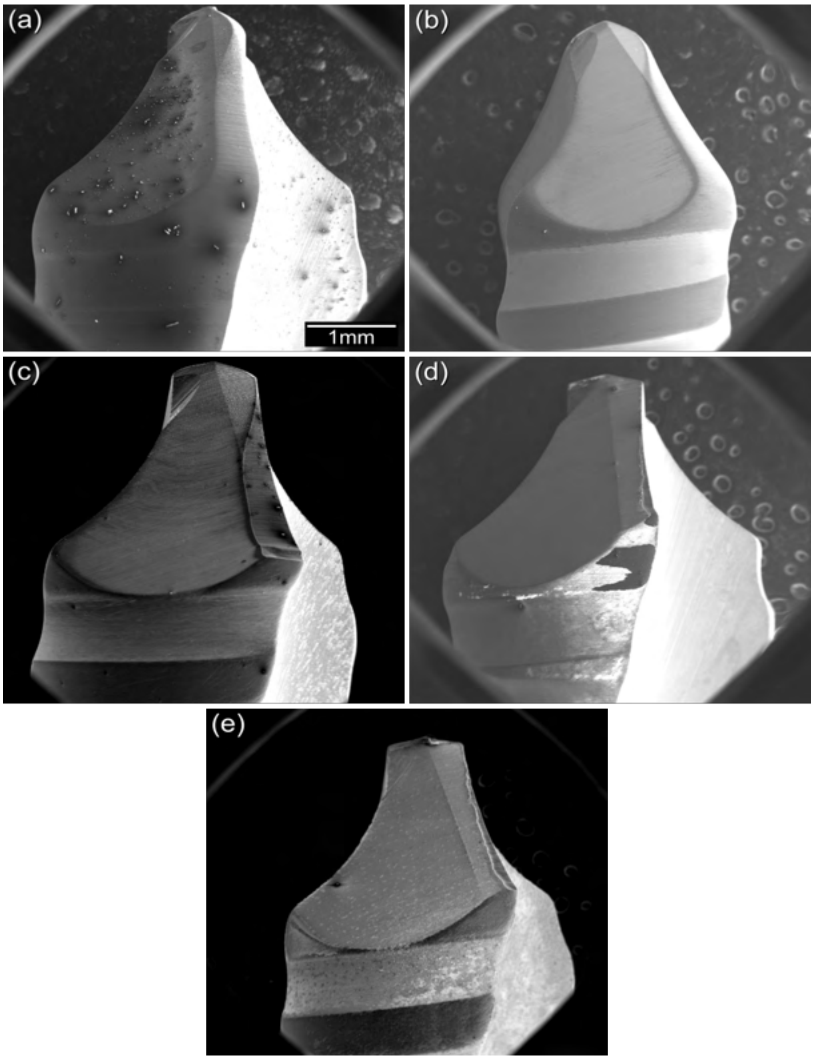

Figure 4.61: SEM images of the fixation pin cutting edges. (a) and (b) show as-received untreated pins, where (b) has also been PVD coated in Ag and Pd prior to drilling. (c) and (d) show C2T pins, where (c) is treated at 660 for 3 h, and (d) is treated at 620 for 80 h. (e) shows C3T Ag/Pd 660 3 h. Magnification is the same for all images.

Optical images of the cutting edge of the same pins as in figure 4.61, but also including as-received pre-drilling, are shown in figure 4.62. The cutting edge has been outlined of the pre-drilled pin (a), which has then been superimposed over the post-drilled pins cutting tips.

From this, approximate percentage area loss of the cutting edge has been calculated. The results of which are displayed in table 4.5. It can be seen that untreated and PVD coated fixation pins had a similar cutting surface percentage area loss (86 %). C2T 660 3 h marginally improved on this with an 83 % loss. Treatments with thicker layers significantly improved on the durability of the cutting edge, where C2T 620 80 h presented only 8 % loss, and C3T Ag/Pd treated for only 3 h presented a 9 % loss.

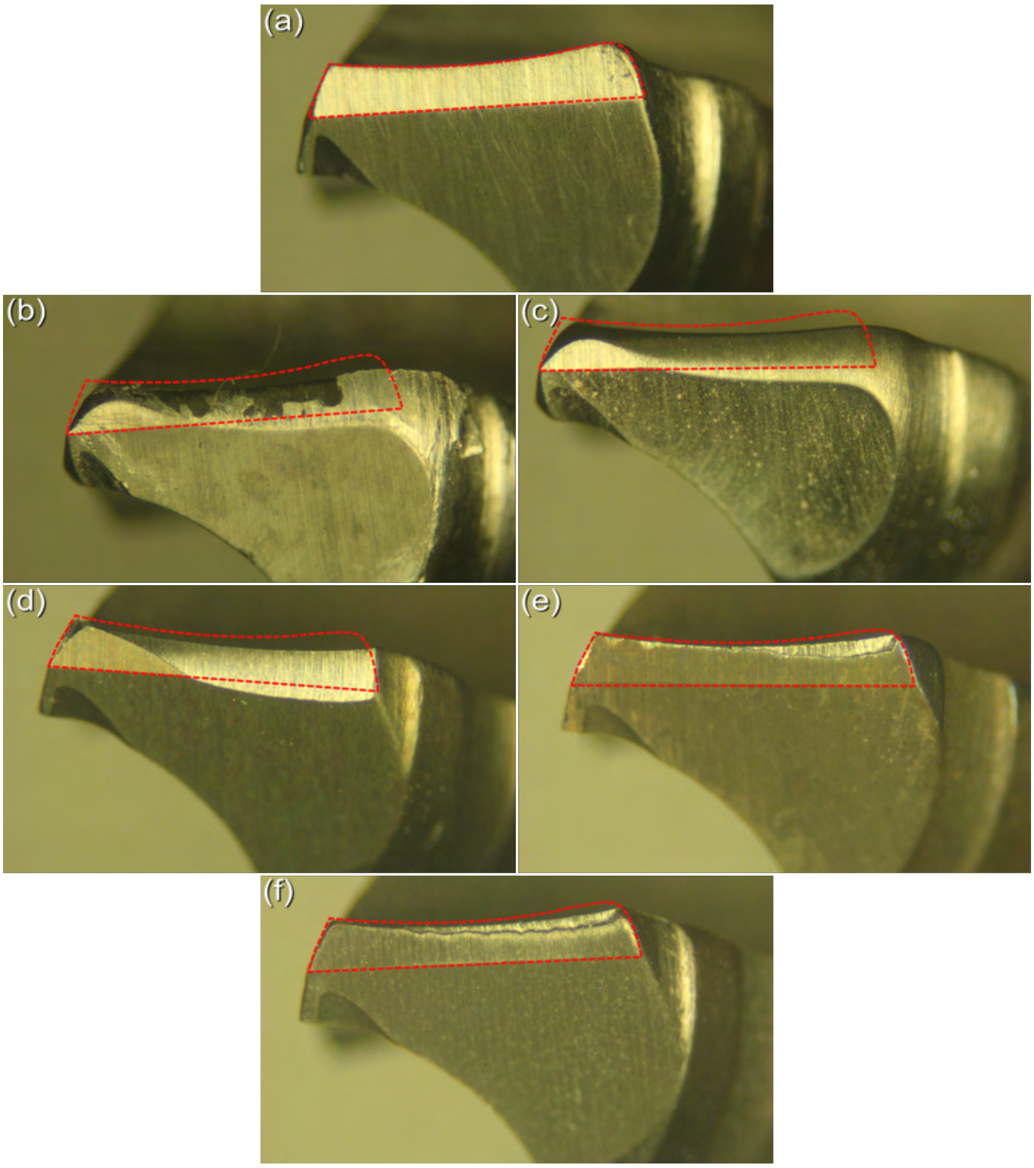

Figure 4.62: Optical images of the fixation pin cutting edges post-drilling. The red dashed region shows the area prior to drilling, and therefore shows the area removed during drilling due to wear of the cutting edge. (a) is of an as-received pin pre-drilling for comparison. (b) and (c) show untreated pins, where (c) has also been PVD coated in Ag and Pd prior to drilling. (d) and (e) show C2T pins, where (d) is treated at 660 for 3 h, and (e) is treated at 620 for 80 h. (f) shows C3T Ag/Pd 660 3 h.

Table 4.5: Percentage area loss of the cutting surface for untreated, PVD, C2T, and C3T fixation pins post simulated bone drilling.

Pin	Cutting surface area loss (%)
As-received (unt) pre-drilled	0
As-received (unt) post-drilled	86
Unt PVD Ag/Pd	86
C2T 660 3h	83
C2T 620 80h	8
C3T 660 3h	9

4.5 Anti-bacterial Performance

4.5.1 Coupons

The antibacterial performance of untreated and treated Ti64 coupons is shown in figure 4.63. Post 6 h incubation, the average number of viable CFU per ml of *S. aureus* inoculant reduced significantly ($p < .05$) for C2T, C3T Au, and C3T Ag/Pd compared with untreated ($40x10^4$).

The application of an Au catalytic layer prior to CCT resulted in a significant ($p < .05$) reduction in CFU per ml compared with C2T of $12x10^4$ vs $20x10^4$, respectively. As expected, due to the presence of silver at the surface, C3T demonstrated a further significant ($p < .05$) reduction vs C2T and C3T Au of $3x10^4$. These suggest that the addition of the catalytic layers, and resultant particles remaining at the surface, result in a significant ($p < .05$) reduction in the number of *S. aureus* able to grow and survive on the surfaces. This is also evidenced by the fact that the removal of the top-most layer (C3T Ag/Pd 660 20 G) results in an increase in CFU per ml to that of the C2T sample.

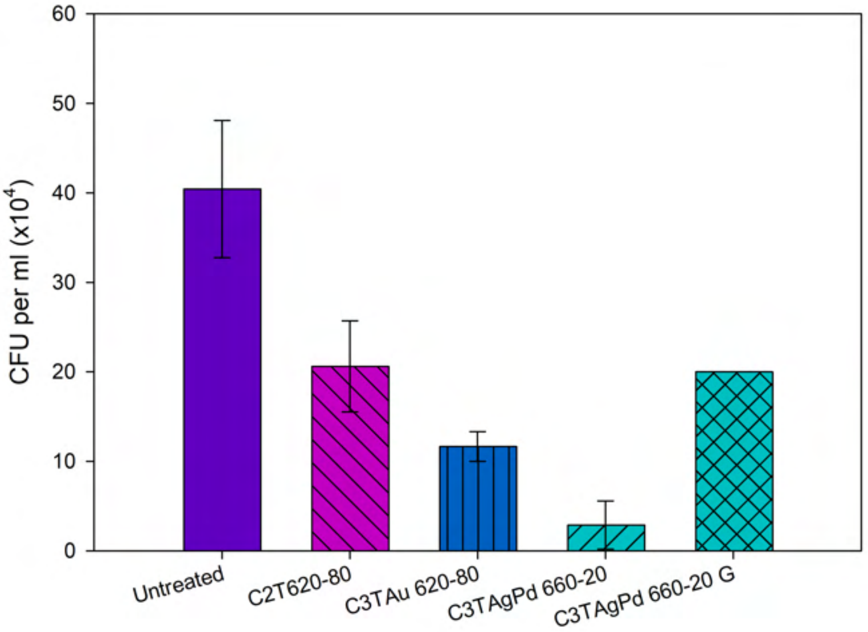

Figure 4.63: Antibacterial performance of Ti64 coupons with *S. aureus*. Untreated, C2T 620 80 h, C3T Au 620 80 h, and both C3T Ag/Pd 660 20 h normal and ground were assessed.

These findings clearly indicate that the ceramic conversion treatment can effectively improve the antibacterial efficacy of Ti64 compared with untreated, with approximately a 50 % reduction in the number of CFUs. Additionally, the catalytic elements introduce a further dramatic increase in antibacterial performance, with a reduction in CFUs of 93 % for Ag/Pd, and 70 % for Au compared with untreated.

The result of changing alloy to Ti67 can be seen in figure 4.64. Like with Ti64, treatment of the coupons resulted in a significant ($p < .05$) reduction in CFU per ml of *S. aureus*. However, unlike with Ti64, the application of Au prior to treatment did not result in a significant ($p > .05$) change in CFU per ml, although there was still a reduction for C3T Au of 20x10^4 versus 27x10^4 CFU per ml.

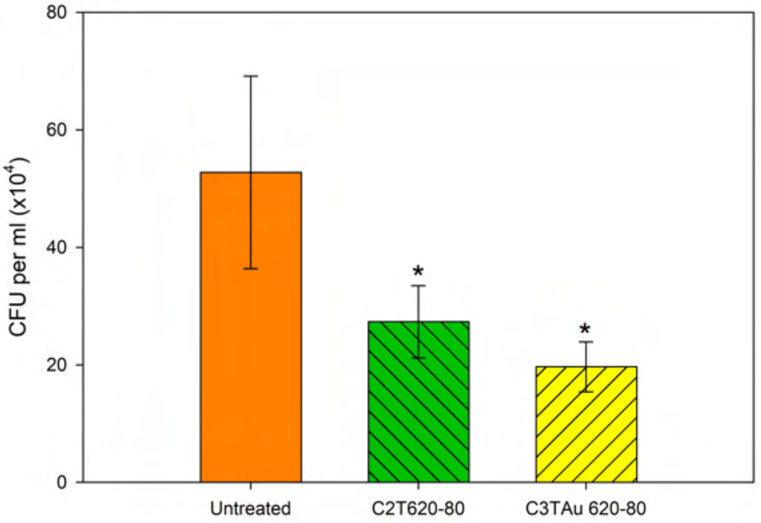

Figure 4.64: Antibacterial performance of Ti67 coupons with *S. aureus*. Untreated, C2T 620 80 h, and C3T Au 620 80 h were assessed. * denotes $p > .05$.

4.5.2 Fixation Pins

The durability of the antibacterial performance has been assessed post-drilling in figure 4.65. Tests were carried out with *S. aureus* grown on as-received (untreated), C2T 660 3 h, C2T 620 80 h, and C3T Ag/Pd 660 3 h. Results statistically non-significant ($p > .05$) are denoted by * in the figure. Please note that the scale is a multiplication.

It can be seen that compared with untreated (75x10^7 ± 5x10^7 CFU/ml), all treatments produced a lower number of colony forming units (CFU) per ml. Although for C2T 660 3 h (68x10^7 ± 3x10^7 CFU/ml), this reduction was not a statistically significant one ($p > .05$), meaning that the difference observed has a possibility to be due to random sampling variability.

Both C2T 620 80 h (47x10^7 ± 6x10^7 CFU/ml) and C3T 660 3 h (33x10^7 ± 3x10^7 CFU/ml) were significantly ($p < .05$) lower than these. And in addition to this, the C3T 660 3 h produced a significantly ($p < .05$) reduced number of CFU/ml compared with the C2T 620 80 h. However, this reduction is only marginally statistically lower ($p = .04$).

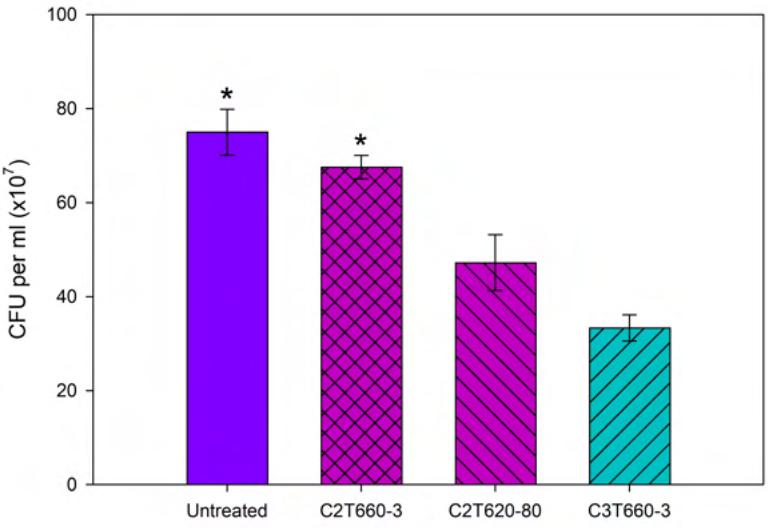

Figure 4.65: Antibacterial performance of post-drilling untreated, and C2T and C3T treated fixation pins with *S. aureus*. * denotes $p > .05$.

Chapter 5

Discussion

Titanium and its alloys are commonly used within the biomedical field, however, owing to their poor tribological properties, they have limited use within the orthopaedic field. In addition to this, concern has been made over the potential toxicity associated with the alloying components of the currently most adopted alloy Ti-6Al-4V. Because of this, another alloy (Ti-6Al-7Nb) has been developed to try and eradicate this concern. CCT (C2T) is a surface treatment which can be employed to improve upon these poor properties by the growth of a hard oxide layer onto the surface of the alloys, thus improving the wear resistance. However, traditional C2T treatments require long treatment durations to yield relatively thin oxide layers. This study employs catalytic films prior to C2T to produce "catalytic C2T" (C3T) as a means to both reduce treatment durations and/or layer thickness and to promote antimicrobial activity of the surfaces.

This chapter covers the analysis of the influence of these catalytic films on the C2T process of the Ti-6Al-4V and Ti-6Al-7Nb alloys, and any differences found with the new alloy. Changes in surface layer structures and properties will be discussed, along with potential explanations for the changes experienced. In addition to this, their influence on tribological and antibacterial properties will be discussed, along with an assessment of the treatment's suitability for relatively complex geometry fixation pins.

5.1 Influence of Substrate Compositions on CCT

The Ti-6Al-7Nb alloy was developed as a substitute for Ti-6Al-4V within the biomedical field due to the concerns over the potential toxicity of V. Because of this, the non-biomedical properties of the alloy were designed to be closely matched [101]. This was found true within this study, where the untreated alloys presented similar hardness (figures 4.39 and 4.40) and wear factor (figures 4.45 and 4.46) values.

The replacement of vanadium with niobium in the Ti-6Al-7Nb alloy resulted in a significantly reduced oxide layer thickness, evidenced by comparing figures 4.34 and 4.35. As previously mentioned in the literature review (see Section 2.2.3), this is due to niobium increasing the oxidation resistance of the alloy due to it promoting the growth of a continuous alumina (Al_2O_3) layer. This layer acts as a transport barrier for further oxygen diffusion, and therefore titania (TiO_2) growth; evidenced by the 110 peak in the XRD analysis of Ti67 C2T in figure 4.31, which is not present for the Ti64 C2T analysis in figure 4.30. Additionally, the Nb will become enriched at the interface, thus altering the interface chemistry as evidenced in the cross-section SEM images in figure 4.7, showing lighter regions along the interface, and the GDOES depth profile in figure 4.19 showing enriched Nb beneath this interface. Further to this, the vanadium in the Ti64 alloy acts to promote the Al_2O_3 to form in islands within the layer, which act as transport paths for rapid growth [106].

Interestingly, Ti64 did not present alumina for the XRD analysis of the C2T samples when an aluminium-rich layer can be seen in the EDX analysis in figure 4.15 (as can also be seen for Ti67 C2T in figure 4.16). This may be explained by the fact that the Al_2O_3

forming in islands surrounded by TiO_2 and a thicker TiO_2 layer would make it difficult to detect the relatively limited Al_2O_3 present. This is further supported in a study by Varma *et al.* [105], who found that the addition of Nb into the alloy creates a sharper interface between the Al_2O_3 and TiO_2 layers in the oxide, which could have made it easier to detect the Al_2O_3 by XRD analysis.

Although the layers are much thinner on Ti67 than Ti64, it can be seen (figures 4.6 and 4.7) that the quality of the surface oxide layer and the interface between the oxide layer and the substrate is better when the oxide layers are formed on the Ti67 alloy than when formed on the Ti64 alloy, especially at the higher treatment temperatures which were used within this study. This may have occurred due to the reduced oxidation rate reducing the residual stresses experienced within the oxide and at the bulk-oxide interface [4]. This could be attributed to the high Pilling-Bedworth ratio (PGR), the ratio of oxide-to-metal molar volumes (PGR=1.7 for rutile formation on Ti), the high coefficient of thermal expansion ratio of Ti to rutile (about 1.3), and the large lattice mismatch [194].

Despite these thinner oxide layer thicknesses, the surface micro-hardness values were similar between the two alloys (figures 4.39 and 4.40). This is likely attributed to the already mentioned continuous Al_2O_3 layer, which is harder than TiO_2 [195].

Owing to the similar hardness values and oxide type, it could be expected that the tribological performance of the C2T samples would be similar. However, when comparing Ti64 (figure 4.45) and Ti67 (figure 4.46) C2T wear factor results it can be seen the Ti67 had a significantly reduced performance. This can be attributed to the thin oxide layer and the low hardness in the diffusion zone. As evidenced in figures 4.43 and 4.44, when treated under the same conditions (660°C/80h), the total hardened cases for C2T 660 80 treated Ti64 and Ti67 is about 100 (figure 4.43) and 40 (figure 4.44) microns respectively. Thus, it can be deducted that when C2T is treated under the same conditions, the load bearing capacity, and hence the resistance to surface damage under a high load, should be much higher for Ti64 than for Ti67. Accordingly, the thin oxide layer on C2T treated Ti67 would be easily collapsed under the tribo-loading, thus forming hard abrasive particles and therefore severe abrasive wear quickly occurs to the underlying material, evidenced in figure 4.53.

5.2 Catalytic Effect on CCT

Both conventional ceramic conversion treatment (C2T) and novel catalytic ceramic conversion treatment (C3T) resulted in the production of an oxide layer, as seen in the SEM cross-sectional images in figures 4.6, 4.7, 4.10, 4.11, and 4.14. This oxide layer consisted of mainly rutile, evidenced by the XRD analysis in figures 4.30, 4.31, 4.32, and 4.33. The addition of catalytic films typically also resulted in the detection of alumina during this XRD analysis. Peaks of alumina were also found by Khanna *et al.* [196] when they carried out thermal oxidation of Ti64 at a higher temperature (800 °C) than used within this study.

C2T is an already established treatment [14] of Ti-6Al-4V (Ti64), whose parameters require treatments of long duration (80+ h), to yield high-quality oxide layers of $\approx 3\ \mu$m, which was also shown in this study (figure 4.34). However, this is a time and energy consuming process and it is also difficult, if not impossible, to generate a thick oxide layer without striation within the layer and with strong bonding to the substrate. This is because, at low temperatures (or the initial oxidation period) in an oxidizing atmosphere, oxide scale formation follows these steps [4]: oxygen adsorption at the surface, oxide nucleation, lateral growth of the nuclei and formation of a compact oxide scale, which will then separate the surface from the gaseous environment, thus retarding the oxidation process.

As reported in the preceding chapter, the pre-deposition of catalytic films (Au, Ag, Pd, and Ag/Pd) can promote the growth of high-quality oxide layers during ceramic conversion treatment of both Ti64 and Ti67 alloys. For instance, as shown in figure 4.37, the pre-deposition of Ag/Pd can reduce the C3T time to as low as 1 h and produce an oxide layer of $\approx 4\ \mu$m thick, which would take 80+ h to be produced by C2T. However, it should be pointed out that the catalysing effect depends on the types of the catalytic elements as well as the substrates.

According to diffusion theory, a continuous thin-film would retard the uptake and the inwards diffusion of oxygen. However, it can be seen in figure 4.1 that the pre-deposited film is not a continuous thin-film, but rather nano-particles, with an average particle size of ≈ 57 nm, which will not prevent titanium adsorption of oxygen. The non-continuity is also evidenced in figure 4.8, where agglomeration of the particles can be seen. These nano-particles were blocking the lateral growth of the TiO_2, which made the TiO_2 grains form in the nanoscale, and in turn, those grain boundaries provided multiple tunnels for fast inward oxygen diffusion. Similar observations were reported by Prodromides *et al.* [197] on TiZrV getter films, where the presence of grain boundaries in the nano-crystalline structure promoted in depth diffusion of oxygen.

As discussed within the literature review, different elements within this film will have different effects on C3T through different mechanisms [106, 174], which will be discussed in the following subsections.

5.2.1 Catalytic Effect of Au

It has been found that ultrafine dispersed particles of Au, especially ones supported on substrates such as TiO_2, are able to have high activity for catalytic combustion [198, 199]. It is clear to see by comparing the oxide layer thickness in figures 4.34 and 4.35 that the application of Au prior to CCT resulted in a significant increase in thickness compared with C2T, especially so for Ti67. This agrees with the literature [165, 181] where Au was also successfully used as a catalyst for Ti64 CCT.

This can potentially be explained by a study conducted by Tanaka *et al.* [179]. They carried out TEM and looked at Ti ion interaction in the presence of gold nanoparticles within TiO_2. They found that the presence of these gold nanoparticles resulted in O_2^- formation at the TiO_2/gold perimeter within rutile, which resulted in the diffusion of interstitial Ti to said perimeter. This, therefore, provides more active sites in addition to the normal lattice sites, thus increasing oxidation rate. This may have also occurred within this study. Additionally, the clustering of Au at the surface of the oxide layer rather than dispersion throughout seen in figures 4.4(c,e,g) and 4.5(c,e,g) further supports the outward diffusion of the Ti to the Au particles, and is supported by the TEM analysis carried out in [200] by Tanaka *et al.*, which is shown in figure 5.1. It can be seen in the figure that the Au particles move outwards on top of TiO_2 pillars.

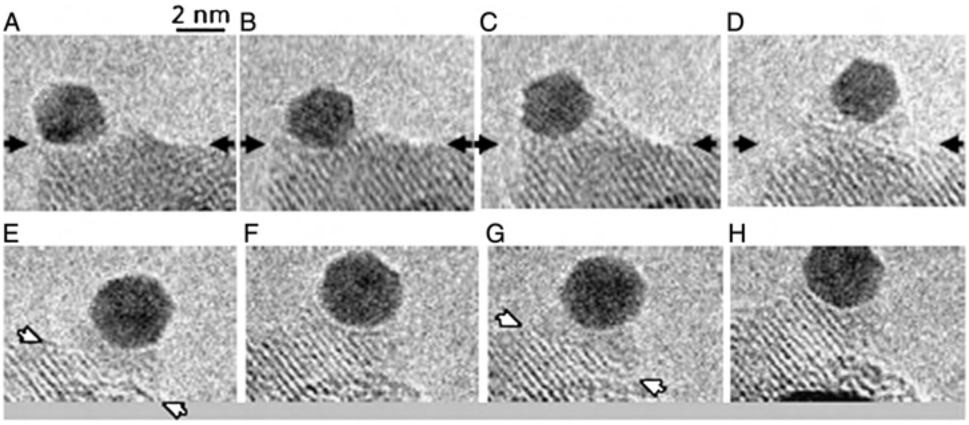

Figure 5.1: *in-situ* TEM of an Au particle supported on TiO_2. (A) is the starting point, prior to O_2 exposure, and (B-H) show increasing time from 198-1327 s post-exposure. Source: [200]

5.2.2 Catalytic Effect of Ag

Ag was shown to have a great effect on catalysing CCT, and evidenced in figure 4.38, where after 5 h of treatment at 660 °C the oxide layer produced by C3T Ag is 1110% thinker than that by C2T. This agrees with the literature [183, 184], where Ag was also successful at catalysing the CCT process, but the mechanisms involved are still under investigation.

It is known that at elevated temperatures (up to $\approx$ 300 °C), Ag forms AgO and Ag_2O. Increasing temperatures further causes the dissociation of the Ag and oxygen, thus significantly increasing the amount of available oxygen present at the surface [184]. In addition to this, Ag doping in TiO_2 is known to cause grain refinement by acting as a diffusion barrier, thus confining the TiO_2. This results in an increase in required energy to move the grain boundaries for TiO_2 particle coalescence [201]. This will result in fine columnar grain production, and as it is reported that the oxygen diffusion coefficient along grain boundaries is 108 times greater than that of bulk diffusion [202], this significantly increases diffusion throughout the layer. This will be discussed further in conjunction with C3T Ag/Pd later in this section.

5.2.3 Catalytic Effect of Pd

As well as Au and Ag, Pd has also been shown to promote oxidation of Ti [106]. This can be seen to be true in figure 4.38, where a significant increase in layer thickness is seen compared with C2T. However, the effect was not as significant as the other catalytic elements. As well as being thicker, like the other C3Ts, this layer is also significantly harder than C2T, evidenced in table 4.1. Pd has been shown to increase oxidation with a similar mechanism to Au of creating TiO_2 islands at the surface [200, 203]. This can be seen by the clustered/agglomerated surface structure shown in figure 4.13(c).

5.2.4 Synergetic Catalytic Effect of Ag/Pd

Ag is known to agglomerate at higher temperatures, which will decrease its catalytic ability. A method to overcome this is the utilisation of mixed films to increase thermal stability, and therefore reduce agglomeration [204]. As well as this, it will lead to electron interactions between the mixed metals, and result in modifications to the active sites/morphology of them. This will result in a different reactivity for the catalyst [185–187]. A mixed film consisting of Ag and Pd was used within this study, and it is clear to see (figure 4.37) that, as with Ag alone, the combination of Ag and Pd to produce C3T Ag/Pd has successfully led to a significantly increased thickness of this oxide, to $\approx 100\ \mu$m after 80 h. It can also be seen that reducing the C3T time to as low as 1 h can yield oxides with similar thickness to what would require the long 80+ h treatments with C2T, of ≈ 4 μm thick. The catalytic effectiveness of the Ag/Pd films were significantly greater in the first 40 h of treatment; these initial stages were 22 times faster than C2T. When the treatment duration increased over 40 h, the rate reduced to 0.5 μm/h, but this is still 5 times greater than C2T. This suggests that in the initial stages the Pd was successfully able to retard agglomeration, and therefore increase oxidation rate, but with increasing treatment duration this reduced. This is evidenced in figure 4.8, where large surface agglomerates have formed, which increase in size with increasing treatment duration. In addition to this, the combination of Ag and Pd showed to be significantly more effective at catalysing CCT than both Ag and Pd alone in these initial treatment stages, evidenced in figure 4.38.

However, it was also noticed that for the longer treatment durations (such as 80 h), Ag alone was more effective. This seemingly abnormal result could be related to the difference in the quality of the oxide layers formed by Ag and by Ag/Pd. As shown in figure 4.14, the addition of Pd into the Ag catalytic layer can not only more effectively increase the oxide thickness but also delay the striation of TiO_2 and Al_2O_3 which usually occurs with treatments at 650-800 °C [205–207] and delay the degradation of the oxide quality (figures 4.14(d vs b)). This effect is more pronounced for the long duration (80 h) treatments of C3T Ag (figure 4.14(f)) and C3T Ag/Pd (figure 4.14(h)). Whilst the oxide layer produced by C3T Ag/Pd is very dense, the C3T Ag treatment led to a thicker oxide layer with many distributed pores. It is believed that these pores could have facilitated the rapid diffusion of Ti and O thus leading to a very thick oxide layer; however, such thick oxide layers with many large pores would be expected to be easily removed via connection of the pores and eventual delamination under tangential forces during service.

It is clear that the co-deposition of Ag and Pd as a pre-deposited layer can produce a synergetic catalytic effect in terms of increasing the growth rate of the oxide layer at the initial oxidation stages and acts to avoid the degradation of oxide layer quality during the later stages.

For the C3T Ag/Pd treatments, this effect was continued until Pd particles were agglomerated to large particles and Ag was exhausted from the surface due to dispersion within the formed TiO_2, as evidenced by the fact that the oxidation rate was reduced only after 40 h and the reduction in Ag wt% with increasing treatment duration (figure 4.25) [114].

In addition to this, surrounding the agglomerates are needle-like structures (figure 4.8), which EDX analysis show to be rich in vanadium (evidenced in figure 4.26). TEM analysis of this region (figure 4.29B) confirmed this and found the presence of $AgVO_3$. This is in agreement with a study by Tousley *et al.* [208], where silver-coated vanadium powders resulted in an increased production of vanadium oxide with these same needle-like structures. This is supported by the finding after the examination of figure 4.8 in which the needle-like phases gradually disappeared after 40 h for the C3T Ag/Pd treatments.

It is clear to see that the catalytic films applied prior to CCT had a significant effect on the growth of oxide layers on the titanium surfaces. In order to further advance scientific understanding of the catalytic effect of Ag/Pd, Ti64 C3T Ag/Pd treated at 660 °C for 20 h has been selected for detailed TEM characterisation. This is due to the surface features shown in figure 4.26, which present both agglomerated and needle-like structures. An area with both of these structures was selected and subsequently FIB-milled.

EDX/STEM chemical composition mapping of this C3T Ag/Pd 660 20 h sample (figures 4.21, 4.24, 4.28, and 4.29) demonstrates movement of the pre-coated Ag/Pd catalytic elements for treatment durations longer than 10 h at 660 °C. It revealed that Pd agglomerated at the surface and formed PdO, while Ag particles were finely dispersed in the TiO_2 layer, and the quantitative analysis of the Ag content in both particles and the matrix (TiO_2) further confirmed this observation (figures 4.25 and 4.26). Based on the Ellingham-diagram [209], Ag_2O can be formed at low temperatures when oxidised in air. However, it is unstable above 462 K and the formed Ag_2O will reduce to stable Ag metal. Due to Ti's strong affinity to O, when Ti diffuses outwards to meet oxygen and form TiO_2, the stable Ag particles act as doping elements pinning TiO_2 grains, thus preventing them growing to a large size. This resulted in the formation of nano-crystalline columnar TiO_2. This formed near vertical (to the sample surface) columnar grain boundaries between the nano-crystalline grains, thus acting as oxygen diffusion channels. The dispersion of Ag particles in the TiO_2 matrix are in good agreement with Adochite *et al.* [210] who reported the same on a silver doped TiO_2 system obtained by magnetron sputtering after annealing between 400–600 °C, and such a phenomenon might have been induced by Ag diffusion along the TiO_2 grain boundaries, as suggested by Armelao *et al.* [211]. [114]

On the other hand, the nano-crystaline columnar TiO_2 grains prevented the formation of a lateral Al_2O_3 layer. According to Du *et al.* and Cimenoglu *et al.* [206, 212] multi-layered oxides will form on the surface of Ti–6Al–V alloy with long duration oxidation, which is due to alternating growth of Al_2O_3 and TiO_2 layers by outward diffusion of aluminium and inward diffusion of oxygen. At the early stages of oxidation, Al_2O_3 nucleates on the surface together with TiO_2. At extended oxidation times, Al_2O_3 grows laterally and covers TiO_2. In this case, the outer most section of the oxide layer (gas/oxide interface) is Al_2O_3, while the inner section of the oxide layer (oxide/substrate interface) is TiO_2. Once the critical thickness is exceeded, cracks develop at the interface, where the conditions might be similar to the bulk atmosphere of the early stage of oxidation. Aluminium from the substrate would again diffuse outward and form the second Al_2O_3 layer on the second TiO_2 layer in the crack. However, this lateral structure, and thus the cracks, were not observed within the C3T coupons even after 80 hours of treatment. The finely distributed Ag within columnar nano-crystalline TiO_2 grains firstly prevented the lateral TiO_2 oxide layer growth, and secondly, the fast columnar growth of the TiO_2 ejected the aluminium along the grain boundaries perpendicular to the surface, as evidenced in figure 4.28(Al). [114]

Surface enrichment of vanadium, and thus the formed AgVO acicular phase, during ceramic conversion treatment may also contribute to the fast growth of the surface oxide layer. And as previously mentioned, oxygen diffusion along grain boundaries is much faster. [114]

5.2.5 Effect on Diffusion Zone

Cross-sectional hardness is a means to determine the thickness of the ODZ into the substrate. The measurements in the substrate beneath the oxide layer, shown in figures 4.43 and 4.44, were reduced for all C3T samples. This was also reported by Zhang *et al.* [165, 181]. It was speculated to be due to an increased outwards diffusion of titanium cations to meet the oxygen and form TiO_2, reducing the amount of available oxygen for inwards diffusion.

5.3 Improved Performance of Catalytic CCT

5.3.1 Influence of C3T on Durability

As discussed in chapter 2, titanium and its alloys are known to be chemically active and coupled with their high ductility, this results in adhesion to the counterpart. This adhesion is typically stronger than the titanium and results in rupturing of the asperities formed [213], thus resulting in severe adhesive wear. This is evidenced in figure 4.50(a), 4.53(a), and table 4.4. If this severe wear were to occur within the body, not only would the wear debris cause damage due to an accumulation in the local area and other organs, but when coupled with the toxic nature of the alloying elements, it will lead to a cascade of issues for the patient [82, 91]. To this end, improving the durability of these alloys is vital for their long-term use within the biomedical field.

It can be seen in figure 4.47 that the wear factor of untreated Ti64 is very high under both 15 and 50 N. It is noted that increasing the load from 15 to 50 N for tribo testing resulted in a reduced wear factor. This phenomenon is believed to be due to the fact that although there was a 3.3 times increase in load (15 to 50 N), there was not a 3.3 times increase in contact pressure, evidenced in table 3.5. This is due to the untreated Ti64 undergoing more deformation at the higher load, thus increasing the contact area between the substrate and counterpart, therefore reducing the contact pressure. This is not taken into consideration in the wear factor calculation. Additionally, the higher load may have caused a sufficient temperature increase between the substrate and counterpart due to frictional heating during wear, which induced the generation of a tribofilm consisting of oxidised Ti64 wear particles, thus increasing wear resistance of the Ti64, which was also found by Ding *et al.* [214]. [114]

One of the main purposes of the ceramic conversion treatment (CCT) is to increase the durability of titanium and its alloys [14]. Owing to this, as expected, the treatments used within this study were able to successfully increase the wear resistance of the titanium alloys. This is because the treated samples should reduce/remove the amount of adhesive wear because of the tribopair change from Ti/WC to ceramic/WC, and this ceramic of rutile being a hard (figures 4.39, 4.40, 4.41, and table 4.1) and lubricous oxide [166].

However, although the C2T significantly reduced the wear factor compared with untreated when tested at a relatively low load of 15 N, no significant reduction in wear factor was observed when tested at 50 N, as seen in figure 4.47. This is not expected due to the large increase in surface micro-hardness as previously mentioned. This can be explained by comparing the profiles of the wear tracks (figure 4.49), where the C2T had a much rougher track compared with untreated, owing to it having suffered from severe abrasive wear. This is due to the relatively thin oxide being cracked and worn due to the large contact pressure and C2T having a lower load bearing capacity versus C3T Ag/Pd (figure 4.42), therefore producing hard abrasive particles; and because of this relatively thin oxide layer and the lower load bearing capacity being present, this led to the wear track penetrating beyond the oxide layer and into the underlying bulk material, leading to the severe wear demonstrated.

It can be seen that the application of catalytic layers, and therefore C3T treatments, were able to significantly reduce the wear factor compared with the conventional C2T treatment (figures 4.45, 4.46, and 4.47). For Ti64 C3T Ag/Pd, this could be attributed to the presence of the outer-most layer (figures 4.28 and 4.29), which consists of agglomerates of palladium (with trace silver) oxide, vanadium oxide and amorphous-like fine grains of alumina presenting within the grain boundaries. This superficial layer with the underneath supporting nano-columnar $TiO_2 + Al_2O_3$ layer provided high surface hardness of above 1000 HV 0.025 (figure 4.41) and high load bearing capacity (figure 4.42) [114]. This layer was also found to be more durable than the WC counterpart used, evidenced in figure 4.52 and table 4.3 where a surface tribo-film consisting of tungsten oxide was found. This is due to wear of the counterpart occurring and the resulting debris oxidising due to the high temperature produced from the sliding frictional forces. Although TEM was not carried out on the C3T Au samples, the presence of alumina in the XRD analysis (figures 4.30, 4.31, 4.32, and 4.33) suggests that the significant reduction in wear factor could be attributed to similar structures. In addition to this, the catalytic elements agglomerated at the surface of C3T samples could act as solid lubricants, thus reducing the wear experienced. A study by Li *et al.* [215] found this to be true when they applied silver spheres onto the surface of titanium and found it was able to reduce the wear by creating a plastic deformation body at the surface, thus providing a silver-rich lubrication layer which reduces both the friction and wear [114].

Interestingly, removal of the outermost surface containing the catalytic elements resulted in a further reduction in wear factor (figure 4.47). This is likely due to the reduction in surface roughness (table 4.2), and therefore reduced friction experienced (figure 4.48) during the tribo tests. This is because, typically, increasing surface roughness results in increased wear due to increased abrasion by hard asperities [110].

5.3.2 Influence of C3T on Anti-bacterial Performance

Within the biomedical field, implant-associated infections are a major concern. Therefore, the ability of a material to demonstrate antibacterial behaviour is important for reducing implant failure rates in order to reduce both patient and NHS stress. The results of antibacterial testing untreated and treated Ti64 and Ti67 with *S. aureus* on coupon samples have demonstrated the ability of the treatments to increase antibacterial efficacy (figures 4.63 and 4.64).

The antibacterial properties of the C2T compared with untreated Ti64 demonstrated a significant reduction, of approximately 50 %, in the amount of *S. aureus* CFU per ml. This is consistent with the literature [53, 216]. This is typically thought to be due to titanium oxide inherently being able to produce reactive oxygen species (ROS), capable of disrupting cell membranes and walls. However, the surface morphological changes present between untreated and treated titanium will also have a large influence on the bacterial attachment and growth. A paper by Bazaka *et al.* [134] showed that rougher surfaces (such as for the treated versus untreated samples) decrease the cell bonding. This has been evidenced in a paper by Liu *et al.* [54], who found TiO_2 to have a reduced number of bacteria anchor points due to the increase in nano-roughness. This, coupled with TiO_2 having a change in surface energy, and thus more protein adhesion/more bacteria repelling proteins, would result in a more antibacterial surface. In addition to this, *S. aureus* demonstrates preferential growth in trenches of long rows [134], which could result in more bacterial attachment/growth on the untreated samples due to the presence of the grinding grooves.

A further reduction in the number of CFU per ml was found with C3T. This was especially true for Ti64 Ag/Pd, where compared with untreated, there was a 93 % reduction, and when compared with C2T, an 85 % reduction. This is since it has silver present on the surface, which is well known for its antimicrobial activity. This is thought to be from hindering metabolism and DNA replication of the bacterial cells, ultimately resulting in cell death [20,21,49,216,217]. As well as this, palladium and palladium oxide have recently been reported to be antimicrobial [22,58], which would further improve the antibacterial performance experienced.

Although C3T Au did result in a reduction in CFU/ml, it was not as significant as for Ag/Pd, especially so for the Ti67 treated samples. Within the literature, although gold nanoparticles have been suggested to be bactericidal, the results are conflicting, and even if they are shown to be it is only at high concentrations [218]. Because of this, the changes found in this study are likely due to the morphological/chemical changes at the surface experienced between the C2T and C3T Au samples.

These findings provide evidence that the reported treatments can produce a durable surface, capable of reducing the number of CFU/mL of *S. aureus* without the need for additional antimicrobial coatings/material, such as biomimetic anchored polymer brushes [219] or antimicrobial Ag/polyacrylonitrile nanofibers [220], which although they offer antibacterial activity, would not offer a durable antimicrobial solution for orthopaedic implants. [114]

Although untreated Ti67 presented a poorer antibacterial performance compared with Ti64, it was not a significant ($p > .05$) increase in the number of CFUs/ml. A recent study by Prosolov *et al.* [221] found uncoated Ti67 to have marginally improved antibacterial performance compared with uncoated Ti64. The reported differences are likely due to variance during testing, although further testing to compare the two alloys is merited.

5.3.3 Enhanced Performance of Fixation Pins

When a bone fracture would not be able to anatomically repair, external fixation devices are employed [72]. This is where fixation pins are drilled into the bone, and externally bolted to a cage support. The drilling procedure produces friction, and therefore heat. If the temperature of the bone gets too high, it will damage the cells, and potentially lead to apoptosis/necrosis. A recent review by Kniha *et al.* [222] found that bone thermal necrosis occurs at 47-55 °C for 1 min; but this can only be used as a guideline as the study was found to be inconclusive.

CCT successfully significantly ($p < .05$) reduced the drilling temperature (figure 4.60), where the temperature of the bone remained below threshold for all drilling procedures. However, the pin temperature reached above temperature threshold for untreated and PVD (60 and 57 °C, respectively), and in the lower threshold region for C2T and C3T ($\approx$ 50 °C); although the drilling duration was only $\approx$ 30 s for C3T, $\approx$ 35 s for C2T, and $\approx$ 40 s for untreated and PVD, evidenced in figure 4.57, which is lower than the stated threshold time of 1 min. These temperatures are similar to what is experienced within the literature [222, 223]. A study by Bachus *et al.* [224] found that increasing drilling force results in a decrease in generated temperature, which contradicts the findings of this study (figures 4.57 and 4.58). Therefore, the increased heat generation associated with untreated and PVD is likely due to the wear of the cutting edge rounding the edge (figure 4.62 and table 4.5), and therefore generating more friction with continued drilling.

The thermal couple positioning in the simulated bone material is not able to be im-

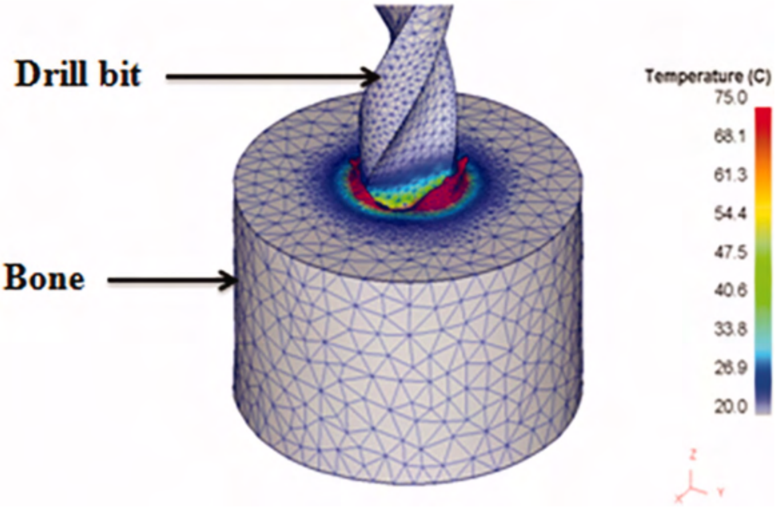

Figure 5.2: Finite element analysis of a fixation pin during drilling into bone, demonstrating the temperature gradient around the drilling area. Source: [59]

mediately next to the fixation pin as this could easily result in damage to the thermal couple. This results in the temperature measurement for the bone material is a lot lower than it would be at the immediate vicinity to the pin. This can be seen in papers by Mediouni *et al.* [59, 225], where they carried out finite element analysis of drilling an acetabular, and it can be seen that the temperature immediately surrounding the fixation pin has a dramatic change with increasing distance. In addition to this, the initial bone temperature during drilling would be at room temperature, but within the body it would be higher [226]. However, drilling *in vivo* will have faster heat dissipation due to the blood flow within the bone [227], which when coupled with cool irrigation fluid [228] will mean that the generated temperatures would be lower than demonstrated in this study. A paper by Sener *et al.* [229] found that irrigation reduced the temperature from 50.9 °C to 37.4 °C, which is well below threshold.

Pin-tract infections are a common and concerning complication of external fixation devices [230]. In order to determine whether the treated fixation pins antimicrobial properties were durable enough to withstand the drilling procedure, antimicrobial testing was carried out on the pin tips post-drilling. The results of this can be seen in figure 4.65. The treatment of the fixation pins successfully reduced the number of CFU/ml of *S. aureus*; but this was only significant for the C2T 80 and C3T Ag/Pd 3 pins. This is likely due to the relatively thin oxide layer present for the C2T 3 pin being worn away during the drilling procedure. The addition of catalytic films for the C3T Ag/Pd pin demonstrated a further significantly ($p < .05$) reduced CFU/ml compared with C2T. This reduction is not as significant as for the coupon samples, as seen in figure 4.63. This is likely attributed due to the drilling procedure removing some of the surface layer silver/palladium. However, these results are a worst-case scenario as the cutting edge of the pins are not the common site of infection; the typical site of pin-tract infections occurs at the pin-air-skin interface, as shown in figure 5.3. These results show promise for the use of C3T Ag/Pd for the treatment of fixation pins to help reduce pin-tract infection rates and the generated temperature/required force.

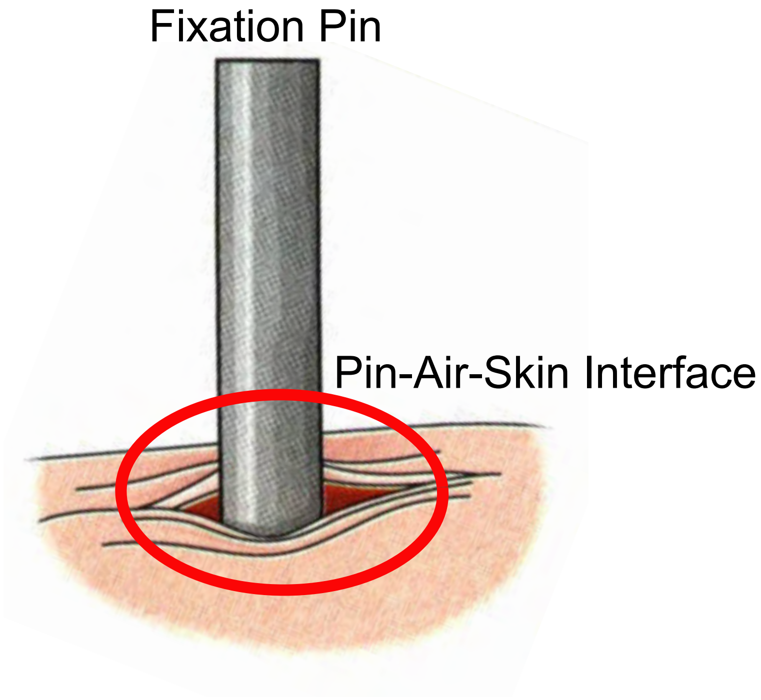

Figure 5.3: Schematic of a fixation pin tract. The area within the red denotes the pin-air-skin interface; the main site of infections. Adapted from: [231]

Chapter 6

Conclusions and Future Work

6.1 Summary and Conclusions

Within this study, the pre-deposition of catalytic films to Ti-6Al-4V and Ti-6Al-7Nb alloys prior to ceramic conversion treatment as a means to increase oxide layer thickness and/or reduce treatment duration has been explored. The key findings can be summarised as:

1. Untreated Ti67 presented similar hardness and wear factor, but increased oxidation resistance compared with Ti64, this is mainly due to the oxidation protecting effect of Nb in Ti67. Due to this increased oxidation resistance, and therefore reduced oxide layer thickness, C2T Ti67 demonstrated a significantly reduced durability compared with Ti64 C2T when treated under the same thermal oxidation conditions. Ti67 and Ti64 demonstrated similar antimicrobial properties with *S. aureus*. However, the application of Au prior to C2T resulted in a significant increase in oxide thickness, durability, and antimicrobial efficacy compared with the conventional C2T treatment carried out under the same conditions.

2. The application of catalytic films prior to ceramic conversion treatment (C3T) resulted in a significantly increased oxide layer thickness, which was also of high

quality. This was especially true for Ti64, where comparing to C2T of 80+ h to yield oxides of $\approx 4\ \mu$m, the same layer thickness can be achieved with the application of Ag/Pd in only 1 h. Increasing treatment duration to 80 h results in a layer thickness of 100 μm.

3. For long treatment durations (80 h) at 660 °C, the catalytic effectiveness in terms of oxide layer thickness were determined to be Ag $>$ Ag/Pd $>$ Au $>$ Pd. This difference in catalytic effectiveness is related to the behaviour of the catalysing elements in the catalytic conversion treatment (C3T).

4. The application of Au films prior to C2T can increase oxidation rate presumably through forming O_2^- at the TiO_2/gold perimeter. This results in the outwards diffusion of interstitial Ti to this perimeter. Pd is thought to have acted to increase oxidation rate in a similar way.

5. Ag was found to cause grain refinement by pinning the TiO_2 grains, this therefore increases the number of grain boundaries for diffusion. As well as this, Ag will form AgO and Ag_2O. As this is unstable at elevated temperatures, it reduces to Ag and O which subsequently results in increased Ti outwards diffusion. These lead to an increased diffusion/oxidation rate for both C3T Ag and Ag/Pd.

6. XRD, SEM, TEM and EDX analysis of Ti64 C3T Ag/Pd revealed a surface layer structure consisting of two sublayers: (1) a superficial layer with agglomerates of palladium (with trace silver) oxide, vanadium oxide, and amorphous-like fine grains of alumina presenting within the grain boundaries; (2) a dominant nano-columnar TiO_2/Al_2O_3 layer with traces of silver and palladium particles.

7. The addition of Pd to the Ag film was able to successfully retard Ag agglomeration in the initial treatment stages (up to 40 h), and therefore increase the catalytic effectiveness of the film, where C3T Ag was 11.8 μm and C3T Ag/Pd 14.3 μm after treatment for 5 h. After these initial stages (40-80 h), large agglomerates began to form which increased in size with increasing treatment duration.

8. C3T resulted in the production of an oxide layer with an increased surface hardness from $\approx$ 900 for C2T to $\approx$ 1100 HV0.025 for C3T. C3T also provided an increased load bearing capacity compared with C2T. In addition to this, C3T resulted in a much-improved durability with a reduction in wear factor from $\approx$ 390 to $\approx$ 5 $m^3/N \cdot m$. This is due to the formation of alumina within the oxide layer, which is a harder oxide than rutile, and the formation of an underlying nano-columnar grain layer which supports this alumina.

9. Due to the presence of Au, Ag, and Pd nanoparticles associated with the C3T samples, a significant reduction in the number of colony forming units of *S. aureus* was measured compared with both untreated and C2T. This was especially true with the presence of Ag due to its strong antimicrobial activity. C2T also demonstrated antimicrobial efficacy compared with untreated, but this was not as significant as for C3T.

10. Fixation pin drilling proved the durability of the treatments for complex geometries, where it reduced the required insertion forces and generated temperatures during the drilling procedure, which is highly beneficial for reducing the damage to bone and for allowing fast healing post-surgery.

11. Post-drilling antimicrobial testing demonstrated the durability of the antimicrobial properties, where a significant reduction in the number of colony forming units of *S. aureus* was found for the treated pins, and a further reduction for the C3T pins was seen.

6.2 Suggested Future Work

- The addition of catalytic films prior to CCT showed great improvement to the conventional CC treatment. This merits the exploration of other elements which may be able to have an effect on CCT, especially if cheaper elements can be utilised. In addition to this, as the application of a thin films promoted the generation of nano-grains, changing the size of the sputtered particles and the film thickness to determine their influence on the grain growth could be explored.

- Typically, thick oxide layers result in poor interfacial bonding between the layer and bulk material. However, this did not occur with C3T within this study. Investigation into this in the form of scratch testing and deeper analysis at the interface to increase the scientific understanding of why this has occurred should be carried out.

- The presence of metallic particles at the surface of/within the oxide layer could potentially influence the corrosion properties of the oxide. Because of this, corrosion testing in the form of electrochemical impedance spectroscopy, and the utilisation of simulated body solution (Ringer's solution) would be useful to determine their effects and suitability for biological environments.

- This study showed promising antimicrobial activity with *S. aureus*, which is gram positive. Further investigation of this with other strains of bacteria such as *Escherichia coli* (*E. coli*) which is gram negative is merited. In addition to this, attachment testing of these bacteria cells can be conducted. As well as additional bacterial cells, as the potential use of the C3T treatments is for orthopaedic implants, biocompatibility testing should be carried out to determine the effect of C3T on osteoblasts/fibroblasts.

- As mentioned in section 5.3.3, fluid flow through bone and surgical irrigation reduces the temperature generated during fixation pin drilling. It would be scientifically valuable to improve the drilling protocol to include these and therefore increase the accuracy of the data to better match that of the real application.

Bibliography

[1] B. D. Ratner, A. S. Hoffman, F. J. Schoen, and J. E. Lemons, *Biomaterials Science: an introduction to materials in medicine.* Elsevier, 3 ed., 2013.

[2] J. Park and R. S. Lakes, *Biomaterials: an introduction.* Springer Science & Business Media, 2007.

[3] W. R. Wagner, S. E. Sakiyama-Elbert, G. Zhang, and M. J. Yaszemski, *Biomaterials science: An introduction to materials in medicine.* Academic Press, 2020.

[4] C. Leyens and M. Peters, *Titanium and titanium alloys: fundamentals and applications.* John Wiley & Sons, 2003.

[5] M. Kaur and K. Singh, "Review on titanium and titanium based alloys as biomaterials for orthopaedic applications," *Materials Science and Engineering: C*, vol. 102, pp. 844–862, 2019.

[6] S. Prasad, M. Ehrensberger, M. P. Gibson, H. Kim, and E. A. Monaco Jr, "Biomaterial properties of titanium in dentistry," *Journal of Oral Biosciences*, vol. 57, no. 4, pp. 192–199, 2015.

[7] J. Pan, C. Leygraf, D. Thierry, and A. Ektessabi, "Corrosion resistance for biomaterial applications of tio2 films deposited on titanium and stainless steel by ion-beam-assisted sputtering," *Journal of Biomedical Materials Research: An Official Journal of The Society for Biomaterials and The Japanese Society for Biomaterials*, vol. 35, no. 3, pp. 309–318, 1997.

[8] J. J. Varrone, K. L. de Mesy Bentley, S. N. Bello-Irizarry, K. Nishitani, S. Mack, J. G. Hunter, S. L. Kates, J. L. Daiss, and E. M. Schwarz, "Passive immunization with anti-glucosaminidase monoclonal antibodies protects mice from implant-associated osteomyelitis by mediating opsonophagocytosis of staphylococcus aureus megaclusters," *Journal of orthopaedic research*, vol. 32, no. 10, pp. 1389–1396, 2014.

[9] M. E. Portillo, S. Corvec, O. Borens, and A. Trampuz, "Propionibacterium acnes: an underestimated pathogen in implant-associated infections," *BioMed research international*, vol. 2013, 2013.

[10] M. William Jiranek, P. Keogh, M. David Lewallen, M. Paul Manner, M. Wojciech Marczynski, J. B. Mason, M. Kevin Mulhall, W. Paprosky, M. Francisco Piccaluga, M. Gregory Polkowski, *et al.*, "One-stage versus two-stage exchange," *Journal of Orthopaedic Research*, vol. 32, p. S141, 2014.

[11] K. Azzam, K. McHale, M. Austin, J. J. Purtill, and J. Parvizi, "Outcome of a second two-stage reimplantation for periprosthetic knee infection," *Clinical Orthopaedics and Related Research®*, vol. 467, no. 7, pp. 1706–1714, 2009.

[12] P. J. Blau and J. Davis, "Metals handbook desk edition," *Wear Testing, Metals and Ceramics Division, Oak Ridge National Laboratory ASM Handbook*, pp. 1342–1347, 1998.

[13] J. R. Davis, *Surface engineering for corrosion and wear resistance.* ASM international, 2001.

[14] H. Dong, A. Bloyce, P. H. Morton, and T. Bell, "Surface oxidation of a titanium or titanium alloy article," Apr. 3 2001. US Patent 6210807.

[15] H. Dong, *Surface engineering of light alloys: Aluminium, magnesium and titanium alloys.* Elsevier, 2010.

[16] H. Dong, A. Bloyce, P. Morton, and T. Bell, “Surface engineering to improve tribological performance of ti–6al–4v,” *Surface engineering*, vol. 13, no. 5, pp. 402–406, 1997.

[17] S. D. Jackson and J. S. Hargreaves, *Metal oxide catalysis, 2 volume set*, vol. 1. John Wiley & Sons, 2008.

[18] U. Hanefeld and L. Lefferts, *Catalysis: An integrated textbook for students.* John Wiley & Sons, 2018.

[19] F. Kapteijn, A. D. Vanlangeveld, J. A. Moulijn, A. Andreini, M. A. Vuurman, A. M. Turek, J.-M. Jehng, and I. E. Wachs, “Alumina-supported manganese oxide catalysts: I. characterization: effect of precursor and loading,” *Journal of Catalysis*, vol. 150, no. 1, pp. 94–104, 1994.

[20] C. Romanò, H. Tsuchiya, I. Morelli, A. Battaglia, and L. Drago, “Antibacterial coating of implants: are we missing something?,” *Bone & Joint Research*, vol. 8, no. 5, pp. 199–206, 2019.

[21] A. B. Lansdown, “Silver in health care: antimicrobial effects and safety in use,” *Current Problems in Dermatology*, vol. 33, pp. 17–34, 2006.

[22] A. Dumas and P. Couvreur, “Palladium: a future key player in the nanomedical field?,” *Chemical Science*, vol. 6, no. 4, pp. 2153–2157, 2015.

[23] C. P. Adams, K. A. Walker, S. O. Obare, and K. M. Docherty, “Size-dependent antimicrobial effects of novel palladium nanoparticles,” *PloS one*, vol. 9, no. 1, p. e85981, 2014.

[24] D. F. Williams, *The Williams dictionary of biomaterials.* Liverpool University Press, 1999.

[25] Y. Chandorkar, R. K, , and B. Basu, “The foreign body response demystified,” *ACS Biomaterials Science & Engineering*, vol. 5, pp. 19–44, 2019.

[26] D. Zhang, Q. Chen, C. Shi, M. Chen, K. Ma, J. Wan, and R. Liu, “Dealing with the foreign-body response to implanted biomaterials: Strategies and applications of new materials,” *Advanced Functional Materials*, pp. 1–22, 2020.

[27] J. M. Morais, F. Papadimitrakopoulos, and D. J. Burgess, “Biomaterials/tissue interactions: possible solutions to overcome foreign body response,” *The AAPS journal*, vol. 12, no. 2, pp. 188–196, 2010.

[28] E. Gemelli, A. Scariot, and N. H. A. Camargo, “Thermal characterization of commercially pure titanium for dental applications,” *Materials research*, vol. 10, no. 3, pp. 241–246, 2007.

[29] J. A. Planell, S. Best, D. Lacroix, and A. Merolli, *Bone repair biomaterials.* Elsevier, 2009.

[30] J. Powers and J. Wataha, *Dental Materials: Foundations and Applications.* Elsevier, 11 ed., 2017.

[31] Y. Oshida, *Surface Engineering and Technology for Biomedical Implants.* Momentum Press, 2014.

[32] S. Gosavi, S. Gosavi, and R. Alla, "Titanium: A miracle metal in dentistry.," *Trends in Biomaterials & Artificial Organs*, vol. 27, no. 1, 2013.

[33] C. Oldani and A. Dominguez, "Titanium as a biomaterial for implants," in *Recent advances in arthroplasty*, InTech, 2012.

[34] S. D. Elek and P. Conen, "The virulence of staphylococcus pyogenes for man. a study of the problems of wound infection," *British journal of experimental pathology*, vol. 38, no. 6, p. 573, 1957.

[35] W. Zimmerli and P. Sendi, "Pathogenesis of implant-associated infection: the role of the host," in *Seminars in immunopathology*, vol. 33, pp. 295–306, Springer, 2011.

[36] A. G. Gristina, "Biomaterial-centered infection: microbial adhesion versus tissue integration," *Science*, vol. 237, no. 4822, pp. 1588–1595, 1987.

[37] M. Martinez-Perez, C. Perez-Jorge, D. Lozano, S. Portal-Nuñez, R. Perez-Tanoira, A. Conde, M. Arenas, J. Hernandez-Lopez, J. De Damborenea, E. Gomez-Barrena, *et al.*, "Evaluation of bacterial adherence of clinical isolates of staphylococcus sp. using a competitive model: An in vitro approach to the "race for the surface" theory," *Bone & joint research*, vol. 6, no. 5, pp. 315–322, 2017.

[38] H. J. Busscher, H. C. van der Mei, G. Subbiahdoss, P. C. Jutte, J. J. van den Dungen, S. A. Zaat, M. J. Schultz, and D. W. Grainger, "Biomaterial-associated

infection: locating the finish line in the race for the surface," *Science translational medicine*, vol. 4, no. 153, pp. 1–10, 2012.

[39] D. Kapsokalyvas, M. van Hoof, S. Wigren, T. Chimhanda, H. Kuijpers, F. Ramaekers, R. Stokroos, and M. van Zandvoort, "Investigating the race for the surface and skin integration in clinically retrieved abutments with two-photon microscopy," *Colloids and Surfaces B: Biointerfaces*, vol. 159, pp. 97–107, 2017.

[40] J. F. Guest, T. Keating, D. Gould, and N. Wigglesworth, "Modelling the costs and consequences of reducing healthcare-associated infections by improving hand hygiene in an average hospital in england," *BMJ open*, vol. 9, no. 10, p. e029971, 2019.

[41] M. Scholz, *Biofunctional surface engineering.* CRC Press, 2014.

[42] K. Page, M. Wilson, and I. P. Parkin, "Antimicrobial surfaces and their potential in reducing the role of the inanimate environment in the incidence of hospital-acquired infections," *Journal of materials chemistry*, vol. 19, no. 23, pp. 3819–3831, 2009.

[43] T. A. Taylor and C. G. Unakal, "Staphylococcus aureus," *StatPearls Publishing*, 2017.

[44] B. Li and T. J. Webster, "Bacteria antibiotic resistance: New challenges and opportunities for implant-associated orthopedic infections," *Journal of Orthopaedic Research®*, vol. 36, no. 1, pp. 22–32, 2018.

[45] J. O'Neill, "Tackling drug-resistant infections globally: final report and recommendations," 2016.

[46] I. Francolini, C. Vuotto, A. Piozzi, and G. Donelli, "Antifouling and antimicrobial biomaterials: an overview," *Apmis*, vol. 125, no. 4, pp. 392–417, 2017.

[47] P. Zou, W. Hartleb, and K. Lienkamp, "It takes walls and knights to defend a castle–synthesis of surface coatings from antimicrobial and antibiofouling polymers," *Journal of Materials Chemistry*, vol. 22, no. 37, pp. 19579–19589, 2012.

[48] S. Krishnan, C. J. Weinman, and C. K. Ober, "Advances in polymers for anti-biofouling surfaces," *Journal of Materials Chemistry*, vol. 18, no. 29, pp. 3405–3413, 2008.

[49] L. Harris, L. Mead, E. Müller-Oberländer, and R. Richards, "Bacteria and cell cytocompatibility studies on coated medical grade titanium surfaces," *Journal of Biomedical Materials Research Part A: An Official Journal of The Society for Biomaterials, The Japanese Society for Biomaterials, and The Australian Society for Biomaterials and the Korean Society for Biomaterials*, vol. 78, no. 1, pp. 50–58, 2006.

[50] W. Sim, R. T. Barnard, M. Blaskovich, and Z. M. Ziora, "Antimicrobial silver in medicinal and consumer applications: a patent review of the past decade (2007–2017)," *Antibiotics*, vol. 7, no. 4, p. 93, 2018.

[51] G. D. Avila-Quezada and G. P. Espino-Solis, "Silver nanoparticles offer effective control of pathogenic bacteria in a wide range of food products," *Pathogenic Bacteria*, 2019.

[52] S. Hashemikia and M. Montazer, “Sodium hypophosphite and nano tio2 inorganic catalysts along with citric acid on textile producing multi-functional properties,” *Applied Catalysis A: General*, vol. 417, pp. 200–208, 2012.

[53] H. Dong, T. Mukinay, M. Li, R. Hood, S. L. Soo, S. Cockshott, R. Sammons, and X. Li, “Improving tribological and anti-bacterial properties of titanium external fixation pins through surface ceramic conversion,” *Journal of Materials Science: Materials in Medicine*, vol. 28, no. 1, p. 5, 2017.

[54] L. Liu, R. Bhatia, and T. J. Webster, “Atomic layer deposition of nano-tio2 thin films with enhanced biocompatibility and antimicrobial activity for orthopedic implants,” *International journal of nanomedicine*, vol. 12, p. 8711, 2017.

[55] A. Aboelzahab, A.-M. Azad, S. Dolan, and V. Goel, “Mitigation of staphylococcus aureus-mediated surgical site infections with ir photoactivated tio2 coatings on ti implants,” *Advanced healthcare materials*, vol. 1, no. 3, pp. 285–291, 2012.

[56] Y. Guven, N. Ustun, E. B. Tuna, and O. Aktoren, “Antimicrobial effect of newly formulated toothpastes and a mouthrinse on specific microorganisms: An in vitro study,” *European journal of dentistry*, vol. 13, no. 02, pp. 172–177, 2019.

[57] L. Visai, L. De Nardo, C. Punta, L. Melone, A. Cigada, M. Imbriani, and C. R. Arciola, “Titanium oxide antibacterial surfaces in biomedical devices,” *The International journal of artificial organs*, vol. 34, no. 9, pp. 929–946, 2011.

[58] P. Muranyi, C. Schraml, and J. Wunderlich, “Antimicrobial efficiency of titanium dioxide-coated surfaces,” *Journal of applied microbiology*, vol. 108, no. 6, pp. 1966–1973, 2010.

[59] M. Mediouni, T. Kucklick, S. Poncet, R. Madiouni, A. Abouaomar, H. Madry, M. Cucchiarini, B. Chopko, N. Vaughan, M. Arora, *et al.*, "An overview of thermal necrosis: present and future," *Current Medical Research and Opinion*, vol. 35, no. 9, pp. 1555–1562, 2019.

[60] Y.-C. Chen, Y.-K. Tu, Y.-J. Tsai, Y.-S. Tsai, C.-Y. Yen, S.-C. Yang, and C.-K. Hsiao, "Assessment of thermal necrosis risk regions for different bone qualities as a function of drilling parameters," *Computer Methods and Programs in Biomedicine*, vol. 162, pp. 253–261, 2018.

[61] E. Creagh, D. Sheehan, and T. Cotter, "Heat shock proteins–modulators of apoptosis in tumour cells," *Leukemia*, vol. 14, no. 7, pp. 1161–1173, 2000.

[62] C. Timon and C. Keady, "Thermal osteonecrosis caused by bone drilling in orthopedic surgery: A literature review," *Cureus*, vol. 11, no. 7, 2019.

[63] G. F. Tawy, P. J. Rowe, and P. E. Riches, "Thermal damage done to bone by burring and sawing with and without irrigation in knee arthroplasty," *The Journal of arthroplasty*, vol. 31, no. 5, pp. 1102–1108, 2016.

[64] W. Allan, E. Williams, and C. Kerawala, "Effects of repeated drill use on temperature of bone during preparation for osteosynthesis self-tapping screws," *British Journal of Oral and Maxillofacial Surgery*, vol. 43, no. 4, pp. 314–319, 2005.

[65] M. Plecko, C. Sievert, D. Andermatt, R. Frigg, P. Kronen, K. Klein, S. Stübinger, K. Nuss, A. Bürki, S. Ferguson, *et al.*, "Osseointegration and biocompatibility of different metal implants-a comparative experimental investigation in sheep," *BMC musculoskeletal disorders*, vol. 13, no. 1, p. 32, 2012.

[66] M. Ridzwan, S. Shuib, A. Hassan, A. Shokri, and M. M. Ibrahim, "Problem of stress shielding and improvement to the hip implant designs: a review," *J. Med. Sci*, vol. 7, no. 3, pp. 460–467, 2007.

[67] J. R. Martin, C. D. Watts, D. L. Levy, and R. H. Kim, "Medial tibial stress shielding: a limitation of cobalt chromium tibial baseplates," *The Journal of arthroplasty*, vol. 32, no. 2, pp. 558–562, 2017.

[68] G. J. Tortora and B. H. Derrickson, *Principles of anatomy and physiology.* John Wiley & Sons, 2018.

[69] J. Li, L. Qin, K. Yang, Z. Ma, Y. Wang, L. Cheng, and D. Zhao, "Materials evolution of bone plates for internal fixation of bone fractures: A review," *Journal of Materials Science & Technology*, vol. 36, pp. 190–208, 2020.

[70] T. Duckworth and C. M. Blundell, *Orthopaedics and fractures*, vol. 12. John Wiley & Sons, 2010.

[71] R. Slone, M. Heare, R. Vander Griend, and W. Montgomery, "Orthopedic fixation devices.," *Radiographics*, vol. 11, no. 5, pp. 823–847, 1991.

[72] R. H. Palmer, D. A. Hulse, W. A. Hyman, and D. R. Palmer, "Principles of bone healing and biomechanics of external skeletal fixation," *Veterinary Clinics of North America: Small Animal Practice*, vol. 22, no. 1, pp. 45–68, 1992.

[73] D. Seligson, C. Mauffrey, and C. S. Roberts, *External fixation in orthopedic traumatology.* Springer Science & Business Media, 2011.

[74] G. A. Hosny, "Limb lengthening history, evolution, complications and current concepts," *Journal of Orthopaedics and Traumatology*, vol. 21, no. 1, pp. 1–8, 2020.

[75] Q. Guo, T. Zhang, Y. Zheng, S. Feng, X. Ma, and F. Zhao, "Tibial lengthening over an intramedullary nail in patients with short stature or leg-length discrepancy: a comparative study," *International orthopaedics*, vol. 36, no. 1, pp. 179–184, 2012.

[76] P. Li, F. Tao, W. Song, J. Dong, D. Qiu, and D. Zhou, "External fixation-assisted reduction for the treatment of neglected hip dislocations with limb length discrepancy: a retrospective study of 13 cases," *BMC Musculoskeletal Disorders*, vol. 20, no. 1, pp. 1–5, 2019.

[77] G. A. Ilizarov, "The principles of the ilizarov method.," *Bulletin of the Hospital for Joint Diseases Orthopaedic Institute*, vol. 48, no. 1, pp. 1–11, 1988.

[78] Y. Liu, M. Yushan, Z. Liu, J. Liu, C. Ma, and A. Yusufu, "Complications of bone transport technique using the ilizarov method in the lower extremity: a retrospective analysis of 282 consecutive cases over 10 years," *BMC Musculoskeletal Disorders*, vol. 21, pp. 1–9, 2020.

[79] N. M. Kliushin, A. S. Sudnitsyn, K. N. Subramanyam, and J. George, "Management of neurologic deformity of the ankle and foot with concurrent osteomyelitis with the ilizarov method," *Foot & ankle international*, vol. 39, no. 2, pp. 226–235, 2018.

[80] R. Davies, N. Holt, and S. Nayagam, "The care of pin sites with external fixation," *The Journal of bone and joint surgery. British volume*, vol. 87, no. 5, pp. 716–719, 2005.

[81] E. Guerado, J. R. Cano, and F. Fernandez-Sanchez, “Pin tract infection prophylaxis and treatment,” *Injury*, vol. 50, pp. S45–S49, 2019.

[82] M. Wen, C. Wen, P. Hodgson, and Y. Li, “Improvement of the biomedical properties of titanium using smat and thermal oxidation,” *Colloids and surfaces B: biointerfaces*, vol. 116, pp. 658–665, 2014.

[83] G. Lütjering and J. C. Williams, *Titanium.* Springer Science & Business Media, 2007.

[84] D. Apostu, O. Lucaciu, C. Berce, D. Lucaciu, and D. Cosma, “Current methods of preventing aseptic loosening and improving osseointegration of titanium implants in cementless total hip arthroplasty: a review,” *Journal of International Medical Research*, vol. 46, no. 6, pp. 2104–2119, 2018.

[85] G. Welsch, R. Boyer, and E. Collings, *Materials properties handbook: titanium alloys.* ASM international, 1993.

[86] F. Froes, *Titanium: physical metallurgy, processing, and applications.* ASM international, 2015.

[87] H. A. Kishawy and A. Hosseini, “Machining difficult-to-cut materials,” *Mater. Form. Mach. Tribol*, vol. 10, pp. 978–3, 2019.

[88] A. Festas, A. Ramos, and J. P. Davim, “Machining of titanium alloys for medical application-a review,” *Proceedings of the Institution of Mechanical Engineers, Part B: Journal of Engineering Manufacture*, vol. 236, no. 4, pp. 309–318, 2022.

[89] P. Oliveira, *The elements.* PediaPress, 2011.

[90] L. Bolzoni, I. M. Meléndez, E. M. Ruiz-Navas, and E. Gordo, "Microstructural evolution and mechanical properties of the ti–6al–4v alloy produced by vacuum hot-pressing," *Materials Science and Engineering: A*, vol. 546, pp. 189–197, 2012.

[91] M. Khan, R. Williams, and D. Williams, "In-vitro corrosion and wear of titanium alloys in the biological environment," *Biomaterials*, vol. 17, no. 22, pp. 2117–2126, 1996.

[92] J. R. Davis, *Alloying: understanding the basics.* ASM international, 2001.

[93] G. Lütjering and J. Williams, *Titanium.* Engineering Materials and Processes, Springer Berlin Heidelberg, 2013.

[94] R. Pederson, *Microstructure and Phase transformation of Ti-6Al-4V.* PhD thesis, Luleå tekniska universitet, 2002.

[95] R. E. Smallman and A. Ngan, *Physical metallurgy and advanced materials.* Elsevier, 2011.

[96] C. Lee, C.-P. Ju, and J. Chern Lin, "Structure–property relationship of cast ti–nb alloys," *Journal of Oral Rehabilitation*, vol. 29, no. 4, pp. 314–322, 2002.

[97] I.-V. Branzoi, M. Iordoc, and F. Branzoi, "Surface characterization and corrosion behaviour of ti based alloys in fetal bovine serum," *UPB Sci. Bull. Ser. B*, vol. 71, pp. 31–40, 2009.

[98] K. Aniołek, M. Kupka, M. Łuczuk, and A. Barylski, "Isothermal oxidation of ti–6al–7nb alloy," *Vacuum*, vol. 114, pp. 114–118, 2015.

[99] S. Kumar, T. S. Narayanan, S. G. S. Raman, and S. K. Seshadri, “Thermal oxidation of ti6al4v alloy: Microstructural and electrochemical characterization,” *Materials Chemistry and Physics*, vol. 119, no. 1-2, pp. 337–346, 2010.

[100] H. Cimenoglu, O. Meydanoglu, M. Baydogan, H. Bermek, P. Huner, and E. S. Kayali, “Characterization of thermally oxidized ti6al7nb alloy for biological applications,” *Metals and Materials International*, vol. 17, no. 5, pp. 765–770, 2011.

[101] M. F. Semlitsch, H. Weber, R. M. Streicher, and R. Schön, “Joint replacement components made of hot-forged and surface-treated ti-6al-7nb alloy,” *Biomaterials*, vol. 13, no. 11, pp. 781–788, 1992.

[102] K. Aniołek, B. Łosiewicz, J. Kubisztal, P. Osak, A. Stróż, A. Barylski, and S. Kaptacz, “Mechanical properties, corrosion resistance and bioactivity of oxide layers formed by isothermal oxidation of ti-6al-7nb alloy,” *Coatings*, vol. 11, no. 5, p. 505, 2021.

[103] S. Becker, A. Rahmel, M. Schorr, and M. Schütze, “Mechanism of isothermal oxidation of the intel-metallic tial and of tial alloys,” *Oxidation of Metals*, vol. 38, no. 5, pp. 425–464, 1992.

[104] H. Jiang, M. Hirohasi, Y. Lu, and H. Imanari, “Effect of nb on the high temperature oxidation of ti–(0–50 at.%) al,” *Scripta Materialia*, vol. 46, no. 9, pp. 639–643, 2002.

[105] S. Varma, A. Chan, and B. Mahapatra, “Static and cyclic oxidation of ti–44al and ti–44al–xnb alloys,” *Oxidation of Metals*, vol. 55, no. 5, pp. 423–435, 2001.

[106] Y. Shida and H. Anada, “The effect of various ternary additives on the oxidation behavior of tial in high-temperature air,” *Oxidation of Metals*, vol. 45, no. 1, pp. 197–219, 1996.

[107] I. Minami, “Ionic liquids in tribology,” *Molecules*, vol. 14, no. 6, pp. 2286–2305, 2009.

[108] T. Mang, K. Bobzin, and T. Bartels, *Industrial tribology: Tribosystems, friction, wear and surface engineering, lubrication.* John Wiley & Sons, 2011.

[109] J. A. Tichy and D. M. Meyer, “Review of solid mechanics in tribology,” *International Journal of Solids and Structures*, vol. 37, no. 1-2, pp. 391–400, 2000.

[110] D. Dwivedi, *Surface Engineering: Enhancing Life of Tribological Components.* Springer, 1 ed., 2018.

[111] I. Hutchings and P. Shipway, *Tribology: Friction and Wear of Engineering Materials.* Elsevier, 2 ed., 2017.

[112] T. Mang and W. Dresel, *Lubricants and lubrication.* John Wiley & Sons, 2007.

[113] M. M. Khonsari and E. R. Booser, *Applied tribology: bearing design and lubrication.* John Wiley & Sons, 2017.

[114] J. Alexander, H. Dong, D. Bose, A. A. Hassan, S. L. Soo, Z. Zhang, X. Tao, S. Kuehne, X. Li, and H. Dong, “Novel catalytic ceramic conversion treatment of ti6al4v for improved tribological and antibacterial properties for biomedical applications,” *Materials*, vol. 14, no. 21, p. 6554, 2021.

[115] K. Topolovec-Miklozic, F. Lockwood, and H. Spikes, "Behaviour of boundary lubricating additives on dlc coatings," *Wear*, vol. 265, no. 11-12, pp. 1893–1901, 2008.

[116] R. J. Bayer, *Mechanical Wear Fundamentals and Testing, revised and expanded.* CRC Press, 2004.

[117] K.-H. Zum Gahr, *Microstructure and wear of materials*, vol. 10. Elsevier, 1987.

[118] M. Wolski, T. Woloszynski, P. Podsiadlo, and G. W. Stachowiak, "En route to the automated wear surface classification system: differentiating between adhesive, abrasive, and corrosive wear under different load conditions," *Tribology Letters*, vol. 68, no. 3, pp. 1–12, 2020.

[119] J. Takadoum, *Materials and surface engineering in tribology.* John Wiley & Sons, 2013.

[120] R. Chattopadhyay, *Surface wear: analysis, treatment, and prevention.* ASM international, 2001.

[121] P. D BIANCO, P. Ducheyne, and J. Cuckler, "Systemic titanium levels in rabbits with a titanium implant in the absence of wear," *Journal of Materials Science: Materials in Medicine*, vol. 8, no. 9, pp. 525–529, 1997.

[122] R. M. Urban, J. J. Jacobs, M. J. Tomlinson, J. Gavrilovic, J. Black, and M. Peoc'h, "Dissemination of wear particles to the liver, spleen, and abdominal lymph nodes of patients with hip or knee replacement," *JBJS*, vol. 82, no. 4, p. 457, 2000.

[123] T. Rae, “The biological response to titanium and titanium-aluminium-vanadium alloy particles: I. tissue culture studies,” *Biomaterials*, vol. 7, no. 1, pp. 30–36, 1986.

[124] Š. Tarasevičius, R. Tarasevičius, V. Žegunis, A. Smailys, and R. J. Kalesinskas, “Metal type of the femoral stem in total hip arthroplasty,” *Medicina*, vol. 41, no. 11, pp. 932–935, 2005.

[125] N. Eliaz, *Degradation of implant materials.* Springer Science & Business Media, 2012.

[126] Z. A. Uwais, M. A. Hussein, M. A. Samad, and N. Al-Aqeeli, “Surface modification of metallic biomaterials for better tribological properties: A review,” *Arabian Journal for Science and Engineering*, vol. 42, no. 11, pp. 4493–4512, 2017.

[127] W. Jin and P. K. Chu, “Orthopedic implants,” *Encyclopedia of biomedical engineering*, vol. 1, p. 3, 2019.

[128] C. van Der Straeten and K. A. De Smet, “Current expert views on metal-on-metal hip resurfacing arthroplasty. consensus of the 6th advanced hip resurfacing course, ghent, belgium, may 2014,” *Hip International*, vol. 26, no. 1, pp. 1–7, 2016.

[129] B. Bhushan, “Surface roughness analysis and measurement techniques,” in *Modern tribology handbook, two volume set*, pp. 79–150, CRC press, 2000.

[130] D. J. Whitehouse, “Surface metrology,” *Measurement science and technology*, vol. 8, no. 9, p. 955, 1997.

[131] E. Mainsah, J. A. Greenwood, and D. G. Chetwynd, *Metrology and properties of engineering surfaces*. Springer Science & Business Media, 2001.

[132] M. Quinten, *A Practical Guide to Surface Metrology*. Springer, 2019.

[133] R. J. Crawford, H. K. Webb, V. K. Truong, J. Hasan, and E. P. Ivanova, "Surface topographical factors influencing bacterial attachment," *Advances in colloid and interface science*, vol. 179, pp. 142–149, 2012.

[134] K. Bazaka, R. J. Crawford, and E. P. Ivanova, "Do bacteria differentiate between degrees of nanoscale surface roughness?," *Biotechnology Journal*, vol. 6, no. 9, pp. 1103–1114, 2011.

[135] R. Bos, H. C. Van der Mei, and H. J. Busscher, "Physico-chemistry of initial microbial adhesive interactions–its mechanisms and methods for study," *FEMS microbiology reviews*, vol. 23, no. 2, pp. 179–230, 1999.

[136] R. P. van Hove, I. N. Sierevelt, B. J. van Royen, and P. A. Nolte, "Titanium-nitride coating of orthopaedic implants: a review of the literature," *BioMed research international*, vol. 2015, pp. 1–9, 2015.

[137] P. Molitor, V. Barron, and T. Young, "Surface treatment of titanium for adhesive bonding to polymer composites: a review," *International Journal of Adhesion and Adhesives*, vol. 21, no. 2, pp. 129–136, 2001.

[138] E. M. Liston, "Plasma treatment for improved bonding: a review," *The journal of adhesion*, vol. 30, no. 1-4, pp. 199–218, 1989.

[139] P. Sidky and M. Hocking, “Review of inorganic coatings and coating processes for reducing wear and corrosion,” *British Corrosion Journal*, vol. 34, no. 3, pp. 171–183, 1999.

[140] P. Sundriyal, M. Pandey, and S. Bhattacharya, “Plasma-assisted surface alteration of industrial polymers for improved adhesive bonding,” *International Journal of Adhesion and Adhesives*, vol. 101, p. 102626, 2020.

[141] X. Zheng, M. Huang, and C. Ding, “Bond strength of plasma-sprayed hydroxyapatite/ti composite coatings,” *Biomaterials*, vol. 21, no. 8, pp. 841–849, 2000.

[142] X. Suo, M. Yu, W. Li, M. Planche, and H. Liao, “Effect of substrate preheating on bonding strength of cold-sprayed mg coatings,” *Journal of thermal spray technology*, vol. 21, no. 5, pp. 1091–1098, 2012.

[143] Y. Wang, B. Jiang, T. Lei, and L. Guo, “Dependence of growth features of microarc oxidation coatings of titanium alloy on control modes of alternate pulse,” *Materials Letters*, vol. 58, no. 12-13, pp. 1907–1911, 2004.

[144] C. Fei, Z. Hai, C. Chen, and X. Yangjian, “Study on the tribological performance of ceramic coatings on titanium alloy surfaces obtained through microarc oxidation,” *Progress in Organic Coatings*, vol. 64, no. 2-3, pp. 264–267, 2009.

[145] F. Muhaffel, M. Kaba, G. Cempura, B. Derin, A. Kruk, E. Atar, and H. Cimenoglu, “Influence of alumina and zirconia incorporations on the structure and wear resistance of titania-based mao coatings,” *Surface and Coatings Technology*, vol. 377, p. 124900, 2019.

[146] K. Wasa, M. Kitabatake, and H. Adachi, *Thin film materials technology: sputtering of control compound materials*. Springer Science & Business Media, 2004.

[147] K. Reichelt and X. Jiang, “The preparation of thin films by physical vapour deposition methods,” *Thin Solid Films*, vol. 191, no. 1, pp. 91–126, 1990.

[148] A. Baptista, F. Silva, J. Porteiro, J. Míguez, and G. Pinto, “Sputtering physical vapour deposition (pvd) coatings: A critical review on process improvement and market trend demands,” *Coatings*, vol. 8, no. 11, p. 402, 2018.

[149] P. Martin, *Introduction to surface engineering and functionally engineered materials*, vol. 74. John Wiley & Sons, 2011.

[150] M. Faraday, “X. the bakerian lecture.—experimental relations of gold (and other metals) to light,” *Philosophical Transactions of the Royal Society of London*, no. 147, pp. 145–181, 1857.

[151] A. Anders, “Plasma and ion assistance in physical vapor deposition: Ahistorical perspective,” tech. rep., Ernest Orlando Lawrence Berkeley NationalLaboratory, Berkeley, CA (US), 2007.

[152] B. Berghaus, “Improvements in and relating to the coating of articles by means of thermally vaporized material,” 1938. UK Patent 510933.

[153] D. M. Mattox, “Fundamentals of ion plating,” *Journal of Vacuum Science and Technology*, vol. 10, no. 1, pp. 47–52, 1973.

[154] D. Boone, “Physical vapour deposition processes,” *Materials science and technology*, vol. 2, no. 3, pp. 220–224, 1986.

[155] R. Eason, *Pulsed laser deposition of thin films: applications-led growth of functional materials*. John Wiley & Sons, 2007.

[156] E. D. McClanahan and N. Laegreid, "Production of thin films by controlled deposition of sputtered material," *Sputtering by Particle Bombardment III*, pp. 339–377, 1991.

[157] J. M. Schneider, S. Rohde, W. D. Sproul, and A. Matthews, "Recent developments in plasma assisted physical vapour deposition," *Journal of Physics D: Applied Physics*, vol. 33, no. 18, p. R173, 2000.

[158] R. Behrisch and K. Wittmaack, *Sputtering by particle bombardment*, vol. 1. Springer-Verlag Berlin, 1981.

[159] D. Depla, S. Mahieu, *et al.*, *Reactive sputter deposition*, vol. 109. Springer, 2008.

[160] R. Power and S. Rossnagel, "Pvd for microelectronics: Sputter deposition applied to semiconductor manufacturing vol. 26," 1999.

[161] F. Borgioli, E. Galvanetto, F. Iozzelli, and G. Pradelli, "Improvement of wear resistance of ti–6al–4v alloy by means of thermal oxidation," *Materials Letters*, vol. 59, no. 17, pp. 2159–2162, 2005.

[162] R. Hanzel, "Surface hardening processes for titanium and its alloys," *Metal Progr.*, vol. 65, 1954.

[163] T. Bacci, F. Borgioli, E. Galvanetto, F. Galliano, and B. Tesi, "Wear resistance of ti–6al–4v alloy treated by means of glow-discharge and furnace treatments," *Wear*, vol. 240, no. 1-2, pp. 199–206, 2000.

[164] J. Lanagan, *Plasma surface engineering of titanium alloys.* PhD thesis, University of Birmingham, 1988.

[165] Z. Zhang, H. Dong, and T. Bell, "Role of gold in high temperature oxidation of titanium alloy," *Surface engineering*, vol. 21, no. 1, pp. 76–79, 2005.

[166] A. Bloyce, P.-Y. Qi, H. Dong, and T. Bell, "Surface modification of titanium alloys for combined improvements in corrosion and wear resistance," *Surface and Coatings Technology*, vol. 107, no. 2-3, pp. 125–132, 1998.

[167] S. Wendt, P. T. Sprunger, E. Lira, G. K. Madsen, Z. Li, J. Ø. Hansen, J. Matthiesen, A. Blekinge-Rasmussen, E. Lægsgaard, B. Hammer, *et al.*, "The role of interstitial sites in the ti3d defect state in the band gap of titania," *Science*, vol. 320, no. 5884, pp. 1755–1759, 2008.

[168] D. A. Hanaor and C. C. Sorrell, "Review of the anatase to rutile phase transformation," *Journal of Materials science*, vol. 46, no. 4, pp. 855–874, 2011.

[169] G. Wang, J. Li, K. Lv, W. Zhang, X. Ding, G. Yang, X. Liu, and X. Jiang, "Surface thermal oxidation on titanium implants to enhance osteogenic activity and in vivo osseointegration," *Scientific reports*, vol. 6, p. 31769, 2016.

[170] D. S. R. Krishna, Y. Brama, and Y. Sun, "Thick rutile layer on titanium for tribological applications," *Tribology International*, vol. 40, no. 2, pp. 329–334, 2007.

[171] F. A. Shah, M. Trobos, P. Thomsen, and A. Palmquist, "Commercially pure titanium (cp-ti) versus titanium alloy (ti6al4v) materials as bone anchored implants:

Is one truly better than the other?," *Materials Science and Engineering: C*, vol. 62, pp. 960–966, 2016.

[172] K. W. Kolasinski, *Surface science: foundations of catalysis and nanoscience.* John Wiley & Sons, 2012.

[173] O. J. Nguon, *Polymer-stabilized Transition Metal Nanocatalysts: Synthesis, Characterization, and Applications.* PhD thesis, University of Waterloo, 2014.

[174] G. A. Somorjai and Y. Li, *Introduction to surface chemistry and catalysis.* John Wiley & Sons, 2010.

[175] D. Y. Murzin and T. Salmi, *Catalytic kinetics.* Elsevier, 2005.

[176] G. C. Bond, C. Louis, and D. Thompson, *Catalysis by gold*, vol. 6. World Scientific, 2006.

[177] Z. Ma and S. Dai, "Development of novel supported gold catalysts: A materials perspective," *Nano Research*, vol. 4, no. 1, pp. 3–32, 2011.

[178] M. Haruta, T. Kobayashi, H. Sano, and N. Yamada, "Novel gold catalysts for the oxidation of carbon monoxide at a temperature far below 0 c," *Chemistry Letters*, vol. 16, no. 2, pp. 405–408, 1987.

[179] T. Tanaka, A. Sumiya, H. Sawada, Y. Kondo, and K. Takayanagi, "Direct observation of interstitial titanium ions in tio2 substrate with gold nanoparticle," *Surface Science*, vol. 619, pp. 39–43, 2014.

[180] C.-J. Li and X. Bi, *Silver catalysis in organic synthesis.* John Wiley & Sons, 2019.

[181] Z. Zhang, H. Dong, T. Bell, and B. Xu, “The effect of gold pre-deposition on the oxidation behavior of cpti and ti6al4v alloy,” *Oxidation of metals*, vol. 66, no. 1-2, pp. 91–106, 2006.

[182] Z. Zhang, Y. Zhang, X. Li, J. Alexander, and H. Dong, “An enhanced ceramic conversion treatment of ti6al4v alloy surface by a pre-deposited thin gold layer,” *Journal of Alloys and Compounds*, vol. 844, p. 155867, 2020.

[183] T. Mukinay, *The development of antibacterial and wear resistant Ti6Al4V surfaces by silver doping, selective laser melting and thermal oxidation.* PhD thesis, University of Birmingham, 2020.

[184] Z. Zhang, Y. Zhang, X. Tao, K. Liu, A. Burns, P. Li, T. Mukinay, X. Li, and H. Dong, “The exceptional oxidation of ti6al4v alloy with a pre-deposited silver layer,” *Journal of Alloys and Compounds*, p. 163574, 2022.

[185] J. A. Rodriguez, “Bimetallic model catalysts,” *Handbook of Heterogeneous Catalysis: Online*, pp. 1298–1309, 2008.

[186] M. Sankar, N. Dimitratos, P. J. Miedziak, P. P. Wells, C. J. Kiely, and G. J. Hutchings, “Designing bimetallic catalysts for a green and sustainable future,” *Chemical Society Reviews*, vol. 41, no. 24, pp. 8099–8139, 2012.

[187] I. Karakaya and W. Thompson, “The ag- pd (silver-palladium) system,” *Bulletin of alloy phase diagrams*, vol. 9, no. 3, pp. 237–243, 1988.

[188] X. Liu, D. Wang, and Y. Li, “Synthesis and catalytic properties of bimetallic nanomaterials with various architectures,” *Nano Today*, vol. 7, no. 5, pp. 448–466, 2012.

[189] B. C. Gates and F. C. Jentoft, *Advances in catalysis.* Academic Press, 2013.

[190] B. Viswanathan, S. Sivasanker, and A. Ramaswamy, *Catalysis: principles and applications.* Alpha Science Int'l Ltd., 2002.

[191] R. Boddula, A. M. Asiri, *et al.*, *Sustainable ammonia production.* Springer, 2020.

[192] A. Miles, S. Misra, and J. Irwin, "The estimation of the bactericidal power of the blood," *Epidemiology & Infection*, vol. 38, no. 6, pp. 732–749, 1938.

[193] F. H. Furkert, J. H. Sörensen, J. Arnoldi, B. Robioneck, and H. Steckel, "Antimicrobial efficacy of surface-coated external fixation pins," *Current microbiology*, vol. 62, no. 6, pp. 1743–1751, 2011.

[194] M. N. Gardos, "The tribooxidative behavior of rutile-forming substrates," *MRS Online Proceedings Library (OPL)*, vol. 140, 1988.

[195] R. J. Hussey and J. Wilson, *Advanced technical ceramics directory and databook.* Springer Science & Business Media, 2012.

[196] R. Khanna, T. Kokubo, T. Matsushita, Y. Nomura, N. Nose, Y. Oomori, T. Yoshida, K. Wakita, and H. Takadama, "Novel artificial hip joint: A layer of alumina on ti–6al–4v alloy formed by micro-arc oxidation," *Materials Science and Engineering: C*, vol. 55, pp. 393–400, 2015.

[197] A. Prodromides, C. Scheuerlein, and M. Taborelli, "Lowering the activation temperature of tizrv non-evaporable getter films," *Vacuum*, vol. 60, no. 1-2, pp. 35–41, 2001.

[198] M. Valden, X. Lai, and D. W. Goodman, “Onset of catalytic activity of gold clusters on titania with the appearance of nonmetallic properties,” *science*, vol. 281, no. 5383, pp. 1647–1650, 1998.

[199] M. Haruta, “Size-and support-dependency in the catalysis of gold,” *Catalysis today*, vol. 36, no. 1, pp. 153–166, 1997.

[200] T. Tanaka, K. Sano, M. Ando, A. Sumiya, H. Sawada, F. Hosokawa, E. Okunishi, Y. Kondo, and K. Takayanagi, “Oxygen-rich ti1- xo2 pillar growth at a gold nanoparticle–tio2 contact by o2 exposure,” *Surface science*, vol. 604, no. 23-24, pp. L75–L78, 2010.

[201] Y. Yuan, J. Ding, J. Xu, J. Deng, and J. Guo, “Tio2 nanoparticles co-doped with silver and nitrogen for antibacterial application,” *Journal of nanoscience and nanotechnology*, vol. 10, no. 8, pp. 4868–4874, 2010.

[202] J. Godlewski, J. Gros, M. Lambertin, J. Wadier, and H. Weidinger, “Raman spectroscopy study of the tetragonal-to-monoclinic transition in zirconium oxide scales and determination of overall oxygen diffusion by nuclear microanalysis of o 18,” in *Zirconium in the Nuclear Industry: Ninth International Symposium*, ASTM International, 1991.

[203] R. Bennett, P. Stone, and M. Bowker, “Scanning tunnelling microscopy studies of the reactivity of the tio 2 (110) surface: Re-oxidation and the thermal treatment of metal nanoparticles,” *Faraday Discussions*, vol. 114, pp. 267–277, 1999.

[204] D. Adams, T. L. Alford, and J. W. Mayer, *Silver metallization: stability and reliability*. Springer, 2008.

[205] B. Sefer, *Oxidation and alpha–case phenomena in titanium alloys used in aerospace industry: Ti–6Al–2Sn–4Zr–2Mo and Ti–6Al–4V*. PhD thesis, Luleå tekniska universitet, 2014.

[206] H. Du, P. Datta, D. Lewis, and J. Burnell-Gray, "Air oxidation behaviour of ti6al4v alloy between 650 and 850," *Corrosion Science*, vol. 36, no. 4, pp. 631–642, 1994.

[207] G. Fargas, J. J. Roa, B. Sefer, R. Pederson, M. L. Antti, and A. Mateo, "Oxidation behavior of ti–6al–4v alloy exposed to isothermal and cyclic thermal treatments," in *Conference Paper*, 2017.

[208] M. Tousley, A. Wren, M. Towler, and N. Mellott, "Processing, characterization, and bactericidal activity of undoped and silver-doped vanadium oxides," *Materials Chemistry and Physics*, vol. 137, no. 2, pp. 596–603, 2012.

[209] M. Shamsuddin, *Physical chemistry of metallurgical processes*. Springer Nature, 2020.

[210] R. Adochite, D. Munteanu, M. Torrell, L. Cunha, E. Alves, N. Barradas, A. Cavaleiro, J. Riviere, E. Le Bourhis, D. Eyidi, *et al.*, "The influence of annealing treatments on the properties of ag: Tio2 nanocomposite films prepared by magnetron sputtering," *Applied Surface Science*, vol. 258, no. 8, pp. 4028–4034, 2012.

[211] L. Armelao, D. Barreca, G. Bottaro, A. Gasparotto, C. Maccato, E. Tondello, O. I. Lebedev, S. Turner, G. Van Tendeloo, C. Sada, *et al.*, "Rational design of ag/tio2 nanosystems by a combined rf-sputtering/sol-gel approach," *ChemPhysChem*, vol. 10, no. 18, pp. 3249–3259, 2009.

[212] H. Guleryuz and H. Cimenoglu, “Oxidation of ti–6al–4v alloy,” *Journal of Alloys and Compounds*, vol. 472, no. 1-2, pp. 241–246, 2009.

[213] H. Dong and T. Bell, “Enhanced wear resistance of titanium surfaces by a new thermal oxidation treatment,” *Wear*, vol. 238, no. 2, pp. 131–137, 2000.

[214] H. Ding, V. Fridrici, G. Guillonneau, S. Sao-Joao, J. Geringer, J. Fontaine, and P. Kapsa, “Investigation on mechanical properties of tribofilm formed on ti–6al–4v surface sliding against a dlc coating by nano-indentation and micro-pillar compression techniques,” *Wear*, vol. 432, p. 202954, 2019.

[215] X. Li, K. Yang, H. Lin, H. Ma, Y. Han, and Q. He, “Laser additive manufacturing of (ti-6al-4v)/10 wt.% ag composite using spherical powders to reduce wear and friction,” *Journal of Materials Engineering and Performance*, vol. 28, no. 1, pp. 12–19, 2019.

[216] X. Jiang, B. Lv, Y. Wang, Q. Shen, and X. Wang, “Bactericidal mechanisms and effector targets of tio2 and ag-tio2 against staphylococcus aureus,” *Journal of medical microbiology*, vol. 66, no. 4, p. 440, 2017.

[217] U. F. Gunputh, H. Le, K. Lawton, A. Besinis, C. Tredwin, and R. D. Handy, “Antibacterial properties of silver nanoparticles grown in situ and anchored to titanium dioxide nanotubes on titanium implant against staphylococcus aureus,” *Nanotoxicology*, vol. 14, no. 1, pp. 97–110, 2020.

[218] K. Zheng, M. I. Setyawati, D. T. Leong, and J. Xie, “Antimicrobial gold nanoclusters,” *ACS nano*, vol. 11, no. 7, pp. 6904–6910, 2017.

[219] W. J. Yang, T. Cai, K.-G. Neoh, E.-T. Kang, G. H. Dickinson, S. L.-M. Teo, and D. Rittschof, “Biomimetic anchors for antifouling and antibacterial polymer brushes on stainless steel,” *Langmuir*, vol. 27, no. 11, pp. 7065–7076, 2011.

[220] Q. Shi, N. Vitchuli, J. Nowak, J. M. Caldwell, F. Breidt, M. Bourham, X. Zhang, and M. McCord, “Durable antibacterial ag/polyacrylonitrile (ag/pan) hybrid nanofibers prepared by atmospheric plasma treatment and electrospinning,” *European polymer journal*, vol. 47, no. 7, pp. 1402–1409, 2011.

[221] K. A. Prosolov, D. V. Mitrichenko, A. B. Prosolov, O. O. Nikolaeva, V. V. Lastovka, O. A. Belyavskaya, V. A. Chebodaeva, I. A. Glukhov, L. S. Litvinova, V. V. Shupletsova, *et al.*, “Zn-doped cap-based coatings on ti–6al–4v and ti–6al–7nb alloys prepared by magnetron sputtering: Controllable biodegradation, bacteriostatic, and osteogenic activities,” *Coatings*, vol. 11, no. 7, p. 809, 2021.

[222] K. Kniha, N. Heussen, E. Weber, S. C. Möhlhenrich, F. Hölzle, and A. Modabber, “Temperature threshold values of bone necrosis for thermo-explantation of dental implants—a systematic review on preclinical in vivo research,” *Materials*, vol. 13, no. 16, p. 3461, 2020.

[223] G. Augustin, S. Davila, K. Mihoci, T. Udiljak, D. S. Vedrina, and A. Antabak, “Thermal osteonecrosis and bone drilling parameters revisited,” *Archives of orthopaedic and trauma surgery*, vol. 128, no. 1, pp. 71–77, 2008.

[224] K. N. Bachus, M. T. Rondina, and D. T. Hutchinson, “The effects of drilling force on cortical temperatures and their duration: an in vitro study,” *Medical engineering & physics*, vol. 22, no. 10, pp. 685–691, 2000.

[225] M. Mediouni, D. R. Schlatterer, A. Khoury, T. Von Bergen, S. H. Shetty, M. Arora, A. Dhond, N. Vaughan, and A. Volosnikov, "Optimal parameters to avoid thermal necrosis during bone drilling: a finite element analysis," *Journal of Orthopaedic Research*, vol. 35, no. 11, pp. 2386–2391, 2017.

[226] A. Feldmann, J. Anso, B. Bell, T. Williamson, K. Gavaghan, N. Gerber, H. Rohrbach, S. Weber, and P. Zysset, "Temperature prediction model for bone drilling based on density distribution and in vivo experiments for minimally invasive robotic cochlear implantation," *Annals of biomedical engineering*, vol. 44, no. 5, pp. 1576–1586, 2016.

[227] R. Calttenburg, J. Cohen, S. Conner, and N. Cook, "Thermal properties of cancellous bone," *Journal of biomedical materials research*, vol. 9, no. 2, pp. 169–182, 1975.

[228] R. P. Singh, P. M. Pandey, M. A. Mir, and A. R. Mridha, "Thermal changes during drilling in human femur by rotary ultrasonic bone drilling machine: A histologic and ultrastructural study," *Journal of Biomedical Materials Research Part B: Applied Biomaterials*, 2021.

[229] B. C. Sener, G. Dergin, B. Gursoy, E. Kelesoglu, and I. Slih, "Effects of irrigation temperature on heat control in vitro at different drilling depths," *Clinical oral implants research*, vol. 20, no. 3, pp. 294–298, 2009.

[230] C. Stoffel, B. Eltz, and M. J. Salles, "Role of coatings and materials of external fixation pins on the rates of pin tract infection: A systematic review and meta-analysis," *World Journal of Orthopedics*, vol. 12, no. 11, p. 920, 2021.

[231] J. Santy, M. Vincent, and B. Duffield, “The principles of caring for patients with ilizarov external fixation,” *Nursing Standard (through 2013)*, vol. 23, no. 26, p. 50, 2009.